# SHELL STRUCTURE AND CLASSICAL ORBITS IN MESOSCOPIC SYSTEMS

by

KAORI TANAKA

B.Sc. (Science University of Tokyo, 1990)
M.Sc. (McMaster University, 1992)

A Thesis
Submitted to the School of Graduate Studies
in Partial Fulfilment of the Requirements
for the Degree
Doctor of Philosophy

McMaster University

# SHELL STRUCTURE AND CLASSICAL ORBITS IN MESOSCOPIC SYSTEMS

DOCTOR OF PHILOSOPHY (January, 1997)
(Physics)

McMaster University
Hamilton, Ontario

TITLE: Shell Structure and Classical Orbits in Mesoscopic Systems

AUTHOR: Kaori Tanaka

SUPERVISOR: Dr. Rajat K. Bhaduri

NUMBER OF PAGES: x, 132

# Abstract

The theme of this thesis is to understand global shell structure of a finite many-fermion system in connection with short periodic orbits of the corresponding classical system. It is the overall shell structure, or partly resolved quantum fluctuations in the density of states, that is often enough for describing various properties of a system of interacting particles. Through semiclassical periodic orbit theory, one can visualize quantum-mechanical phenomena in terms of simple classical orbits. It is particularly interesting to study this quantum-classical connection in the mesoscopic systems of simple metal clusters and quantum dots, as their size as well as the number of particles can be much larger than in such systems as atoms and nuclei.

We first illustrate a direct connection between quantum shells and classical periodic orbits by means of a mathematical model of a cranked two-dimensional harmonic oscillator. The quantum spectrum exhibits intriguing features, forming the Farey fan pattern. Furthermore, there is an analogy between this cranked model and the system of charged particles in a uniform magnetic field. We then go on to examine the electronic shell structure of simple metal clusters and quantum dots under a homogeneous magnetic field, taking simple mean-field models for these systems.

The so-called supershell structure, a long-range, beating modulation of the electronic shell structure of simple metal clusters, is a fascinating example which can be explained semiclassically in terms of short periodic orbits of high degeneracy. We study the effect of an external magnetic field on this supershell structure, assuming a spherical infinite well as a simple yet realistic mean-field potential for the valence electrons. It is found that there is little perceptible change in the supershells for experimentally feasible field strengths, and if yet stronger fields are assumed, the supershells get destroyed and new beat patterns appear. For semiclassical understanding of these phenomena, we apply a recently developed trace formula for broken symmetry to this system.

The system of quantum dots is more interesting than metal clusters in that its size can be much larger and the effect of magnetic fields on the electronic shell structure is observable for readily available field strengths. We examine the magnetization and magnetic susceptibility of a circular quantum dot with the two limiting cases of mean-field potential for a small and large number of confined electrons. The shell structure reflected in these magnetic properties are compared in the two cases and are interpreted through short classical orbits. In particular, the Aharonov-Bohm oscillations that appear in the strong-field limit, superimposed on the de Haas-van Alphen oscillations in the magnetization, are explained in terms of the shortest orbits that go along the edge of the system.

# Acknowledgements

First of all, I would like to thank my supervisor, Rajat K. Bhaduri, for his guidance. I appreciate his patience, enthusiasm and encouragement along the way to the completion of this work. I would also like to thank Matthias Brack for discussions on the work presented in Chapters 3 and 4, and for letting me visit Universität Regensburg in the summer of 1995. I am grateful to M. V. N. Murthy, with whom I collaborated on the work of Chapter 4, for his help and discussions.

I wish to thank Stephen Creagh for helpful discussions during the collaboration on the semiclassical analysis of Chapter 3. Thanks are also due to Steffi Reimann, Thomas Hirschmann, and Joachim Blaschke for stimulating discussions and along with Stephen, for making my stay in Regensburg a memorable one.

I would like to thank Yuki Nogami for his interest in this work and discussions. Diptiman Sen, Donald Sprung, Hua Wu and Randy Dumont are thanked for helpful comments and discussions.

I must send a special word of thanks to Akira Suzuki for his help and many discussions. His constant encouragement has been instrumental, ever since my freshman year at Science University of Tokyo, when I told him about my desire of doing graduate work on this continent.

The Department of Physics and Astronomy of McMaster University is greatly appreciated for their support during my graduate studies ; special thanks to Marg Wilby for her kind assistance and encouragement. I am indebted to Institut für Theoretische Physik of Universität Regensburg for their hospitality during my stay.

I wish to express my appreciation to Sumi Nogami, Manju Bhaduri, Liz Brack, and Kazuki Miura for their kind help and cheerful encouragement. I thank my parents for support and finally understanding what I have always wanted to do.

Finally, the Natural Sciences and Engineering Research Council of Canada, and last but not least, the Canadian taxpayers are gratefully acknowledged for the financial support.

# Preface

There is a paper included in Chapter 3 in this thesis. This paper was published in *Physical Review B* and has been reprinted here with permission of The American Physical Society.

The original idea of the work developed through my discussions with R. K. Bhaduri. After I completed the quantum-mechanical calculations, the new trace formula for broken symmetry was developed by S. C. Creagh and its application to the current problem as the semiclassical analysis was done in collaboration with S. C. Creagh and M. Brack. The paper was mostly written by me, while some parts were elaborated by M. Brack.

# Contents

# List of Figures

# Chapter 1

# Introduction

The subject of this thesis is the close relation between quantum shell structure and classical periodic orbits in a finite system of many fermions. In the following, we first describe this relation and then give an overview of this thesis.

## 1.1 Quantum Shell Structure and Classical Periodic Orbits

In a quantum-mechanical system in which particle(s) are confined to a finite spatial domain, the particle(s) can take only discrete values of energy. The quantized energy eigenvalues are usually (in systems of two- and three-dimensions) clustered into degenerate or close-lying levels, which are called "shells". The degree of degeneracy or the number of close-lying levels depends strongly on the symmetry as well as the

integrability of the system. The information about quantum energy levels is fully contained in the density of states, $g(E)$, as a function of energy $E$. It is defined including both bound and continuum states as [Beth 37, Huang 65]

$$g(E) = \sum_i \delta(E - E_i) + \frac{1}{i\pi} \mathrm{Tr} S^\dagger \frac{dS}{dE}, \tag{1.1}$$

where $S = e^{i\eta(E)}$ is the S-matrix, with $\eta(E)$ the scattering phase shift. Here we have assumed that the system has a potential of finite depth, so that there are bound states as well as scattering states. The first term sums up bound states with discrete eigenvalues $\{E_i\}$, including their degeneracies. The second sum, $\frac{1}{\pi}\mathrm{Tr}\frac{d\eta}{dE}$, runs over continuum states. If there is a resonant state, $\eta_l(E)$ increases by $\pi$ around the resonance energy, and this is reflected in $g(E)$ as a narrow peak. In this thesis, we consider only potentials of infinite depth (harmonic-oscillator wells, infinite-wall potentials), in which case only bound states exist, and the density of states is given as the first term in Eq.(1.1).

In a finite system which consists of many fermions interacting with each other, to a good approximation, the particles can be described as moving independently in a self-consistent single-particle potential. Such systems are nuclei [Bohr 69, Preston 75], atoms, and simple metal clusters [de Heer 93, Brack 93], in which the particles (nucleons or electrons) are bound in a self-consistent potential-well. Another example is a quantum dot, in which electrons are confined into a finite region at the interface of semiconductor heterostructure by a device potential – it is also called an artificial

atom, as its effective nuclear charge, as well as the number of electrons in it, can be controlled externally [Kastner 93]. The single-particle density of states $g(E)$ is a very important quantity, which describes properties of an interacting many-body system. At low temperatures, the particles occupy single-particle states according to the Pauli exclusion principle, $N$ particles filling up the $N$ lowest-energy states. This results in observable shell effects [Mayer 48, Mayer 49, Haxel 49], as seen in the periodic table of elements [Gasiorowicz 74], and in the mass spectra of nuclei [Myers 66] and of simple metal clusters. Shell effects determine the stability of self-bound systems, and also how the system responds to an external stimulus (e.g., application of a field). The system is most stable when the shells up to the Fermi energy are completely filled by the particles. In such cases, it requires more energy to put another particle in the system or to excite a particle to a higher level, than the cases when the shells are not completely closed.

The density of states as defined in Eq.(1.1) can always be decomposed into a smooth part that varies monotonously as a function of energy and a part that oscillates around it :

$$g(E) = \tilde{g}(E) + \delta g(E)\,. \tag{1.2}$$

The smooth part $\tilde{g}(E)$ describes the average distribution of energy levels. One can also define a smooth part as a function of other parameters such as deformation or external fields that yields the average behaviour of the density of states. The

$\tilde{g}(E)$ may be given by the so-called Thomas-Fermi density of states, $g_{TF}(E)$, or may have extra terms that give small (higher order in $\hbar$) corrections to it [Wigner 32, Kirkwood 33, Balian 70, Balian 71]. The $g_{TF}(E)$ is given by the number of points in the allowed phase space for a given energy $E$ that satisfy the uncertainty relation. For a $D$-dimensional system,

$$g_{TF}(E) = \frac{1}{h^D} \int d\mathbf{r}\, d\mathbf{p}\; \delta(E - H(\mathbf{r}, \mathbf{p}))\,, \tag{1.3}$$

where $H(\mathbf{r}, \mathbf{p})$ is the classical Hamiltonian. The uncertainty relation says that it is not possible to specify a quantum-mechanical state within a cell of size $h^D$ in the phase space. The $g_{TF}(E)$ contains the quantum-mechanical nature in this regard, but not the discreteness of energy spectrum. It is the oscillating part $\delta g(E)$ that reflects the shell structure of quantized and degenerate levels. The $\delta g$ is sometimes called the quantum fluctuations against $\tilde{g}$ [Brack 97].

We are interested in the fluctuating part $\delta g$ that contains shell effects. The $\delta g$ in Eq.(1.2) is basically a sum of delta functions. However, we would like to emphasize that only somewhat smoothed or "partly resolved" $\delta g$ is often important in understanding properties of a many-fermion system. It is the major shells, which may consist of many close-lying and degenerate levels, that determine various properties of the system such as stability or response to an external field. In view of this, one can consider somewhat smoothed $\delta g(E)$ which smoothly oscillates around $\tilde{g}(E)$. The above point can be seen in the total energy of a many-fermion system as described

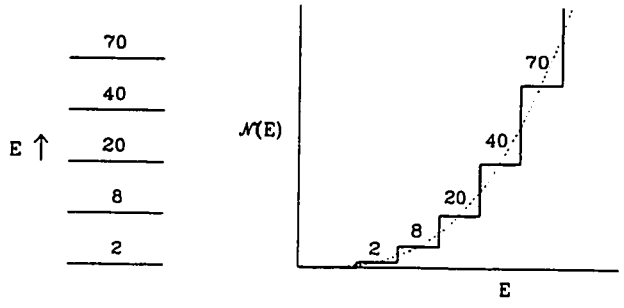


Figure 1.1: Discrete energy levels in the three-dimensional harmonic-oscillator well (left), and the number of available states $\mathcal{N}(E)$ as a function of $E$ (right). Magic numbers including spin degeneracy are shown.

below.

In Fig.1.1, we illustrate the quantum shells in the spherical harmonic-oscillator potential. In this case, shells are the equally-spaced levels, each of which is highly degenerate. We plot the number of states available for energy $\leq E$, denoted by $\mathcal{N}(E)$, which increases stepwise as a function of $E$. The dotted line is the smooth part $\widetilde{\mathcal{N}}(E)$ that arises from $\tilde{g}(E)$ and yields the average behaviour of $\mathcal{N}(E)$, alternately over- and underestimating it. The $\tilde{g}(E)$ is given as $\frac{1}{\hbar\Omega}(\frac{E^2}{(\hbar\Omega)^2} - \frac{1}{4})$, where $\Omega$ is the oscillator frequency [Bhaduri 71]. In Fig.1.1 the numbers of particles for filling up to each shell, including spin degeneracy, are indicated. These are the "magic numbers" for which the system is particularly stable. It is the degeneracy in each shell, rather than the discreteness itself, that results in strong shell effects. The spherical harmonic well can be regarded as a mean-field potential for nuclei, or for simple metal clusters, with a

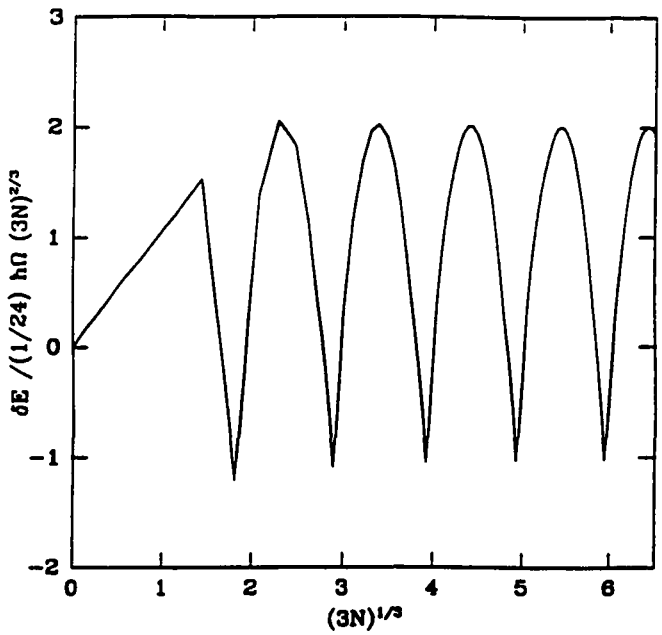


Figure 1.2: Shell correction for the spherical oscillator potential as a function of the particle number $N^{1/3}$.

small number of particles ($\lesssim 40$). For nuclei one needs to assume a strong spin-orbit coupling in order to explain all the magic numbers. Shell effects are reflected in the total energy of the system,

$$E_{tot} = \sum_{i=1}^{N} E_i = \int_0^{E_F} dE\, g(E)\, E, \quad \text{where} \quad N = \int_0^{E_F} dE\, g(E)\,. \tag{1.4}$$

The $E_{tot}$ as a function of the particle number $N$ is a step function as $\mathcal{N}(E)$ in Fig.1.1. According to Eq.(1.2), however, we can decompose it into a smoothly varying, average part $\tilde{E}_{tot}$ and an oscillating part $\delta E_{tot}$. The latter is called "shell correction", as it is the quantum correction to the "classical" (liquid drop) energy $\tilde{E}_{tot}$. The $\delta E_{tot}$ can be

obtained numerically for a given $N$ as [Strutinsky 67, Strutinsky 68]

$$\delta E_{tot} = E_{tot} - \tilde{E}_{tot}\,, \tag{1.5}$$

where the smooth part is given by $\tilde{E}_{tot} = \int_0^{\tilde{E}_F} dE\, \tilde{g}(E)E$, with $\tilde{E}_F$ determined from $N = \int_0^{\tilde{E}_F} dE\, \tilde{g}(E)$. This is shown in Fig.1.2 for the spherical harmonic oscillator. Here $\hbar\Omega$ is taken to vary as $N^{-1/3}$ so that the average Fermi energy $\tilde{E}_F$ is independent of $N$ [Bohr 75], as observed for nuclei and also for simple metal clusters. In Fig.1.2 we see pronounced cusps at the magic numbers, $N = 2, 8, 20, \ldots$, which reflect the stability of the system for these particle numbers. It can also be seen that $\delta E_{tot}$ reflects the shell structure in a somewhat smoothed way. This is because shell correction is an energy integration of $\delta g$. Although the actual magnitude of $\delta E_{tot}$ for nuclei is much smaller than the bulk energy $\tilde{E}_{tot}$, it plays a decisive role in nuclear properties such as the shape deformation and fission barriers.

In the so-called periodic orbit theory [Balian 72, Berry 76, Berry 77, Gutzwiller 71, Gutzwiller 90], the oscillating part $\delta g$ of the quantum-mechanical density of states of a finite system is related to periodic orbits in the corresponding classical system. This can be understood in terms of the semiclassical approximation ($\hbar \to 0$) in which the quantum-mechanical propagator, in the path-integral formalism of wave functions [Feynman 64], is approximated by contributions only from classical trajectories connecting two given points, rather than all the possible paths [Van Vleck 28, Gutzwiller 67]. The quantum density of states $g(E)$ can be expressed in terms of the

propagator $G(\mathbf{r}, \mathbf{r}'; E)$ as

$$g(E) = -\frac{1}{\pi}\mathrm{Im}\,\mathrm{Tr}\,G(\mathbf{r}, \mathbf{r}'; E + i\epsilon) \quad (\epsilon > 0)\,. \tag{1.6}$$

The leading contributions in the trace come from the classical orbits that close upon themselves. The $g(E)$ can then be written in the form of a semiclassical "trace formula", in which $\delta g(E)$ is given by a sum over contributions from all the classical periodic orbits in the system :

$$g(E) = \tilde{g} + \delta g = \tilde{g}(E) + \sum_i A_i(E) \cos\left[\frac{S_i(E)}{\hbar} - \sigma_i \frac{\pi}{2}\right]. \tag{1.7}$$

Here $i$ stands for each periodic orbit as well as its repetitions, and $S_i(E)$ is the classical action along orbit $i$. The amplitude $A_i$ and the phase $\sigma_i$ are also related to characteristics of each periodic orbit.

Quantum mechanically, if the system is integrable and has a high degree of symmetry, energy levels have strong degeneracy and the system exhibits pronounced shell structure. This can be understood in the semiclassical picture that if the system is integrable, for a given $i$ above characterising one type of periodic orbit, there are many such orbits that form a family of "degenerate" periodic orbits. There may be several such families of short periodic orbits with high degeneracy, which determines the overall shell structure. The higher the degree of symmetry of the system is, the higher the degree of degeneracy in each periodic orbit family is, which amplifies shell oscillations. Periodic orbits are important in describing quantum shell structure even in classically chaotic systems. In such systems, there exist unstable periodic orbits

isolated in the phase space which is dominated by ergodic motion, and these periodic orbits play a dominant role in the quantum-classical connection.

An essential point in applying periodic orbit theory to quantum shell structure is the following. As discussed above, the global characteristics of a many-body system are often determined by only partly resolved quantum fluctuations $\delta g$ [Brack 97]. It is the overall shell structure that dictates properties of a self-bound system such as stability, deformation, or fission. Also in systems such as a quantum dot in which particles are confined by a device potential, only partly resolved $\delta g$ is important in its properties, due to finite resolution in measurements, or smearing effect by finite temperature or surface roughness. Through a trace formula, the partly resolved $\delta g$ is related to shortest periodic orbits of the classical system. This can be understood through the uncertainty relation $\Delta E \Delta t \sim \hbar$, as rough resolution in energy corresponds to a short time scale. Thus it is often a few short periodic orbits of high degeneracy that govern global shell structure and therefore are sufficient in describing various properties of a many-body system. It is the strength of periodic orbit theory that it gives intuitive understanding of a quantum-mechanical system of interacting particles. It allows us to visualize quantum phenomena in terms of simple classical orbits, while quantum calculations can be troublesome or fully microscopic calculations for a many-body system may be impossible. This is the theme of this thesis.

To elaborate on the subject of this thesis, we study quantum shell structure and

its semiclassical interpretation in the "mesoscopic" systems of simple metal clusters and quantum dots. A metal cluster, made of metallic atoms, forms anywhere from a diatomic molecule to a particle composed of tens of thousand atoms [de Heer 93]. Shell structure of valence electrons in various kinds of simple metal clusters has been observed, with particle numbers up to several thousands [Pedersen 91, Bréchignac 92, Lerme 96]. A quantum dot is also a finite system of electrons, whose number can vary from one to a few thousands [Lindelof 96]. The electronic shell structure has been observed recently in the conductance of a quantum dot containing 1000-2000 electrons [Persson 95a, Persson 95b, Reimann 96b]. The size of a quantum dot can range from the order of 100 Angstroms to microns. These mesoscopic systems therefore lie in an intermediate region between the microscopic world of atoms and the macroscopic world of bulk metals. It is fascinating that shell effects are observable in these systems with up to so many particles and hence in a much longer energy range than in atoms and nuclei. A striking example is so-called "supershell" structure of alkali metal clusters, a long-range beating pattern in the electronic shell structure. This can be explained semiclassically as an interference effect between two shortest orbits of high degeneracy with slightly different periods. Thus in these systems of mesoscopic sizes, the connection between quantum shells and classical orbits becomes even more interesting.

## 1.2 Overview

In the work presented in this thesis, we take simple physical systems to demonstrate quantum shell effects and their link to short classical orbits in a finite system. Our focus will be on integrable systems and families of degenerate periodic orbits.

Chapter 2 gives preliminaries for the studies in subsequent two chapters in a twofold way. First, we emphasize the importance of periodic orbits in the fluctuating part of the semiclassical density of states of an integrable system. We graphically show a direct connection between the formation of quantum shell gaps and classical periodic orbits, in the system of a particle in a cranked two-dimensional harmonic oscillator. When the system is rotated, an isotropic oscillator potential becomes anisotropic with two different frequencies. As the rotating speed is changed, various ratios of the two frequencies are generated and an array of shell gaps are formed at rational frequency ratios, coinciding with the formation of classical periodic orbits. Secondly, an analogy between the effects of the cranking and of a homogeneous magnetic field in the system of charged particles is described. The latter effect on shell structure in a finite electron system is the subject of the following two chapters.

In Chapter 3, a published paper is included, in which the effect of an external uniform magnetic field on the electronic supershells of simple metal clusters is examined. In this article, a simplest mean-field model is taken for the valence electrons in large metal clusters, which is a free electron gas confined in a spherical cavity with perfectly

reflecting walls. This model is well known for the study made by Balian and Bloch [Balian 72], in which they found these supershell structure and its semiclassical origin as due to periodic orbits of the triangular and square shape, almost two decades prior to the first observation with sodium clusters [Pedersen 91]. How this supershells are affected by a magnetic field is an interesting question, as the classical dynamics will be quite different under the field. In particular, the classical actions that come into the phase of $\delta g$ (see Eq.(1.7)) will be changed by the magnetic flux enclosed by each orbit, and it is expected that the beating pattern is sensitive to such phase changes.

We go on to study the electronic shell structure of a quantum dot in a uniform magnetic field, in Chapter 4. Regarding the influence of a magnetic field, this system is more interesting than the metal clusters in that its size can be much larger. This is because the effective strength of a uniform magnetic field in a finite system is defined by the size of the system measured by the length scale set by the field, the quantum magnetic length or the classical cyclotron radius. In a quantum dot of the size in microns, dramatic changes in the structure of quantum shells, up to the formation of the Landau levels, can be realized with readily available field strengths. Classically this corresponds to changes in the orbit structure of the finite system, from slight bending of the sides of original orbits to the formation of closed cyclotron orbits. We look into the magnetization and the magnetic susceptibility of a circular quantum dot, modelling the system as a two-dimensional electron gas confined in a mean-field potential. Two kinds of mean-field potentials are examined, a harmonic oscillator and

a circular infinite well, which are suitable for a small and a large number of confined electrons, respectively. The shell structure reflected in the magnetization is studied in connection with short classical orbits.

The results of the thesis are summarized and discussed in Chapter 5. In Appendix, numerical procedures for obtaining quantum eigenvalues by a diagonalization method and for evaluating shell correction by Strutinsky's method are described.

# Chapter 2

# Quantum Gaps and Classical Orbits in A Cranked Harmonic Oscillator

## 2.1 Introduction

In this chapter, we study the energy spectrum of a particle in a two-dimensional cranked harmonic oscillator as a function of the cranking frequency [Bhaduri 94]. Although this mathematical model is very elementary and is fully solvable both quantum mechanically and classically, our aim is to emphasize the intimate connection between quantum shells and classical periodic orbits. The occurrence of energy gaps is linked to periodic orbits in the corresponding classical system. In addition, there

are other interesting points that emerge from the study. It is graphically shown that the Landau levels [Landau 58] are generated when the cranking frequency is equal to the oscillator frequency. This demonstrates the analogy between the cranking and the application of a uniform magnetic field in the system of charged particles ; the latter will be examined in later chapters. Furthermore, we look into intriguing aspects of the spectrum beyond the Landau-level limit, which forms the Farey fan pattern [McIlroy 92, Lagarias 92].

In the following, we describe the close connection between quantum energy spectrum and classical periodic orbits in integrable systems. In semiclassical approximation to the quantum density of states $g(E)$, the periodic orbits of the classical system are related to its oscillating part $\delta g(E)$. Berry and Tabor have shown that for integrable systems, it is always possible to give such a semiclassical trace formula [Berry 76, Berry 77]. This comes out naturally from the torus structure of the phase-space manifold in a multi-dimensional integrable system [Tabor 89, Brack 97]. We discuss their derivation in the case of two-dimensional systems. We then present a well-known example of an axially-symmetric deformed harmonic oscillator, which exhibits the direct connection between quantum shells and periodic orbits. This example also illustrates that shorter periodic orbits (of high degeneracy) govern shell structure in longer energy range. This is also seen in the cranked oscillator and will be an important point for studies in the subsequent chapters.

### 2.1.1 Link between quantum spectrum and classical periodic orbits in integrable systems

In an integrable Hamiltonian system of $N$ degrees of freedom, there are $N$ constants of motion $A_i$ $(i = 1, 2, \ldots, N)$ in involution. This means that the trajectories in the $2N$-dimensional phase space are confined to an $N$-dimensional manifold, i.e., an $N$-dimensional continuous surface defined by $N$ equations $A_i$ = constant. One may define $N$ "velocity vectors" on this manifold with components $(\nabla_p A_i, -\nabla_q A_i)$. It can be shown, by the Poisson bracket relations which $A_i$'s satisfy, that they are orthogonal to the normals $(\nabla_q A_i, \nabla_p A_i)$ and thus tangent to the manifold, and that they are all linearly independent. According to the Poincaré-Hopf theorem in topology, an $N$-dimensional manifold for which one can construct $N$ independent commuting vector fields tangent to it has the topology of an $N$-dimensional torus. That is, the phase-space trajectories lie on an $N$-torus. For two-dimensional motion, the manifold is a 2-torus with the topology of a doughnut, as illustrated in Fig.2.1 The $N$-torus is a periodic object, in which one can define $N$ topologically independent closed curves $C_i$. This makes it convenient to introduce the action-angle variables $(\phi_i, I_i)$ and to define $N$ independent actions $I_i$ about the $N$ closed curves $C_i$. The conjugate angles $\phi_i$ do not come into the Hamiltonian, and the energy of the system is expressed as a function of the constant actions $I_i$.

In deriving a semiclassical trace formula for an integrable system, one starts from

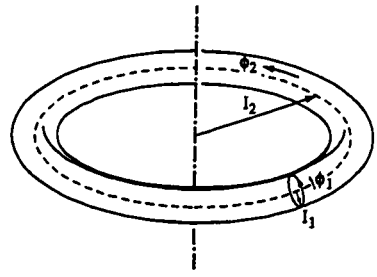


Figure 2.1: The 2-torus manifold for two-dimensional integrable motion, embedded in the four-dimensional phase space. The action-angle variables are indicated. After [Brack 97].

the fact that the quantization of actions yields (approximate) eigenvalue spectrum [Berry 76]. This is borne out by the WKB approximation for one-dimensional systems and the EBK method for multi-dimensional cases.

$$I_i = \frac{1}{2\pi} \oint_{C_i} \mathbf{p} \cdot d\mathbf{q} = (n_i + \frac{\mu_i}{4})\,\hbar\,, \quad n_i = 0, 1, 2, \ldots \quad (i = 1, 2, \ldots, N)\,, \tag{2.1}$$

where $\mu_i$ is the number of turning or "conjugate" points. Let us now consider the quantum density of states for a two-dimensional system [Brack 97] :

$$g(E) = \sum_{n_1=0}^{\infty} \sum_{n_2=0}^{\infty} \delta(E - E_{n_1,n_2})\,, \tag{2.2}$$

where the quantum numbers $(n_1, n_2)$ are assumed to be positive. As a first step to decompose the density of states into a smooth part and an oscillating part, $g(E) =$

$\tilde{g} + \delta g$, one uses the Poisson summation formula

$$\sum_{n=0}^{\infty} f(n) = \sum_{M=-\infty}^{\infty} \int_0^{\infty} dn\, f(n)\, e^{2\pi i M n} + \frac{1}{2} f(0)\,. \tag{2.3}$$

Applying this formula twice to the double sum in Eq.(2.2), $g(E)$ is divided into a double sum and two single sums over the integer $M$. The single sums turn out to be higher order in $\hbar$ and the terms with $M = 0$ yields the smooth part $\tilde{g}$. Thus the leading terms in the semiclassical $\delta g$ are given by the double sum

$$\delta g(E) = \sum_{M_1=-\infty}^{\infty} \sum_{M_2=-\infty}^{\infty} \int_0^{\infty} dn_1 \int_0^{\infty} dn_2\, \delta(E - E_{n_1,n_2})\, e^{2\pi i (M_1 n_1 + M_2 n_2)}\,, \tag{2.4}$$

where the $M_1 = M_2 = 0$ term in the sum are omitted. By virtue of the quantization condition Eq.(2.1), we may change the integration variables from $(n_1, n_2)$ to $(I_1, I_2)$ and write $E_{n_1,n_2} = H(I_1, I_2)$. Using the Fourier representation of the delta function, $\delta(x) = \frac{1}{2\pi} \int_{-\infty}^{\infty} d\tau e^{ix\tau}$, the integrand as a function of $(I_1, I_2)$ is written as

$$\exp\left[i \frac{2\pi}{\hbar} (M_1 I_1 + M_2 I_2) + \tau\,(E - H(I_1, I_2))\right]\,. \tag{2.5}$$

For a given set of integers $(M_1, M_2)$, the dominant contribution to the integrals over $(I_1, I_2)$ come about when the phase is stationary, and the integration may be evaluated by the saddle-point approximation. At the stationary points,

$$\frac{2\pi}{\hbar} M_i = \tau \omega_i\,, \quad i = 1, 2\,, \tag{2.6}$$

where we have used the Hamilton's equation to define the frequencies $\omega_i = \dot{\phi}_i = \frac{\partial H}{\partial I_i}$. This implies that

$$\frac{\omega_1}{\omega_2} = \frac{M_1}{M_2}\,. \tag{2.7}$$

That is, only closed periodic orbits on the torus with commensurate frequencies contribute to $\delta g$. This clearly links classical periodic orbits to the oscillating part of the density of states, and hence to quantum shells.

### 2.1.2 Axially-symmetric deformed harmonic oscillator

We illustrate the above result by a simple model of an axially-symmetric deformed harmonic oscillator [Geilikman 69, Sheline 72]. The system of harmonic oscillator is a special example, for which the trace formula is exactly given [Brack 95, Brack 97]. For a given set of frequencies in the system, e.g., $\omega_i$ $(i = 1, 2, \ldots)$, $\delta g$ is written as a sum over contributions from all the harmonics of each frequency. When the frequencies are in rational ratios, all the orbits are closed and shell gaps are formed in the quantum spectrum, each shell consisting of degenerate levels. The degeneracy of quantum levels reflects the degeneracy of periodic orbit families. If the frequencies are incommensurate, multi-dimensional Lissajous orbits are not closed, although they are confined in a torus in the phase space. There exist periodic orbits in lower dimension in such cases, but their contribution to $\delta g$ is much smaller due to less degeneracy of the orbit families.

These effects may be visualized by plotting the spectrum of the deformed oscillator as a function of the frequency ratio. We write the Hamiltonian for the axially-

symmetric oscillator as

$$H = \frac{\mathbf{p}^2}{2M} + \frac{1}{2}M\left[\omega_\perp^2(x^2+y^2) + \omega_z^2 z^2\right]. \tag{2.8}$$

The quantum eigenvalues may be written as

$$E_{n_\perp,n_z} = \hbar\omega_\perp(n_\perp+1) + \hbar\omega_z\left(n_z+\frac{1}{2}\right), \tag{2.9}$$

where $n_\perp, n_z = 0, 1, 2, ....$ In Fig.2.2 we plot $\{E_{n_\perp,n_z}\}$ as a function of the deformation parameter $\delta \equiv (\omega_\perp - \omega_z)/\omega_0$, where $\omega_0 = (2\omega_\perp + \omega_z)/3$ is the mean oscillator frequency. The formation of shell gaps at various frequency ratios as the system deforms is clearly seen. The arrows indicate some simple ratios of $\omega_\perp$ and $\omega_z$, and magic numbers for the major shells are also shown (including the spin degeneracy). We can see the large shell gaps with the frequencies in simple ratios, e.g., $\omega_\perp : \omega_z = 2 : 1$ ($\delta = 0.6$), which are comparable in magnitude to the ones for the spherical case ($\delta = 0$). This is related to the existence of short periodic orbits. That is, the shorter the orbital period that governs shell structure, the longer the energy range over which the structure is ordered.

The cranking yields similar effects on the spectrum of the harmonic oscillator as the axial deformation in the above example. As the system starts rotating, it breaks the original symmetry of the isotropic oscillator and lifts the degeneracy of the energy levels. It then gives rise to a series of shell gaps, as the cranking frequency is increased, each set of gaps concurring with the formation of closed classical orbits. Interestingly, it generates the quantum gaps that are even larger than the original ones, when the

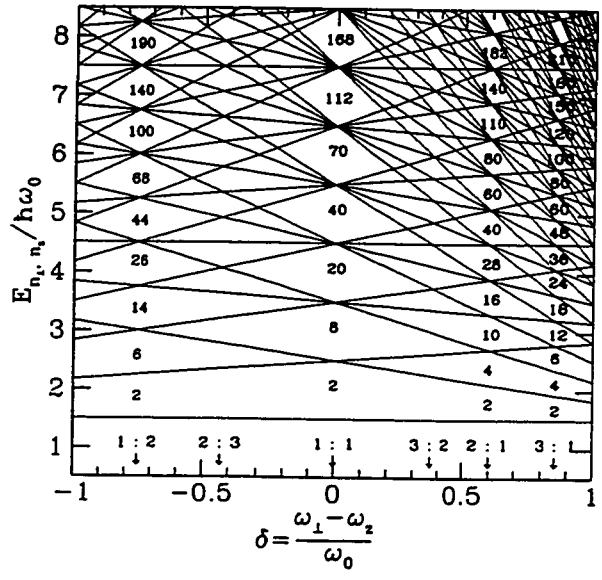


Figure 2.2: Energy spectrum of the axially-symmetric harmonic oscillator, Eq.(2.9), as a function of the deformation parameter $\delta$. The eigenvalues are measured in units of the mean oscillator energy. Some simple frequency ratios are indicated by arrows.

cranking frequency equals the oscillator frequency. They are equivalent to the Landau levels for a charged particle in a uniform magnetic field, each of which is infinitely degenerate. The collapse of the energy levels into the Landau levels is depicted as a function of the cranking frequency. We then go on to study a series of new quantum gaps that are generated as the system is cranked further. Not only that the spectrum beyond the Landau levels forms the Farey fan pattern, there are intriguing aspects in the level structure, particularly the lifting of the degeneracy of the Landau levels.

## 2.2 Two-Dimensional Cranked Oscillator

### 2.2.1 Formation of the Landau levels

We consider the two-dimensional motion of a particle in an isotropic harmonic-oscillator potential on the $xy$ plane, in a rotating frame. The Hamiltonian of the particle is given by

$$H \equiv H_0 + \omega l_z = \frac{1}{2M}(p_x^2 + p_y^2) + \frac{1}{2}M\Omega^2 (x^2 + y^2) + \omega l_z \,, \tag{2.10}$$

where $M$ is the mass of the particle and $\Omega$ the oscillator frequency. The system is rotating about the negative $z$ axis with a frequency $\omega$. The last term, $\omega l_z = \omega (x p_y - y p_x)$, comes from the transformation of the system from a rest frame to a rotating frame. Since this term commutes with the original Hamiltonian $H_0$, it is straightforward to write down the eigenvalues of $H$, in polar coordinates as [Fock 28, Darwin 30]

$$E_{n_r,l} = (2n_r + |l| + 1)\,\hbar\Omega + l\hbar\omega \,. \tag{2.11}$$

Here $n_r = 0, 1, 2, \ldots$ is the radial quantum number and $l = 0, \pm 1, \pm 2, \ldots$ is the angular-momentum quantum number along the $z$ axis. In Fig.2.3, we plot the energy levels $\{E_{n_r,l}\}$, varying the rotational frequency $\omega$ in the range $0 \leq \omega \leq 2\Omega$. We define

$$\nu = \frac{\omega - \Omega}{2\Omega} \,, \tag{2.12}$$

and the spectrum is shown in Fig.2.3 as a function of this dimensionless parameter $\nu$ for $-\frac{1}{2} \leq \nu \leq \frac{1}{2}$.

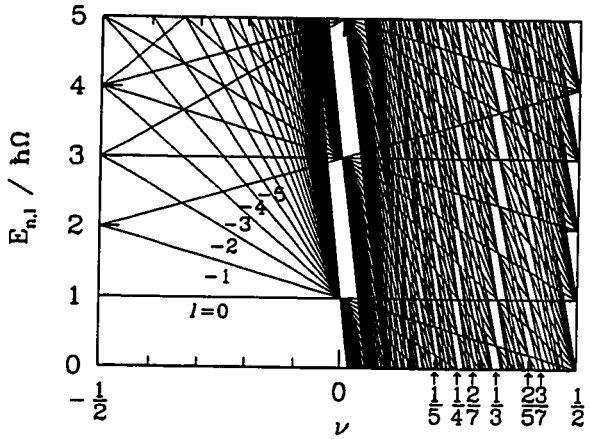


Figure 2.3: Energy spectrum of the cranked two-dimensional harmonic oscillator, Eq.(2.11), as a function of $\nu$, as defined in Eq.(2.12). The Landau levels are formed at $\nu = 0$. Angular momenta for first few states converging to the lowest Landau level are shown.

In Fig.2.3 we can see the collapse of the energy levels at $\omega = \Omega$ ($\nu = 0$) into highly degenerate levels, equally spaced with gaps twice as large as the original ones at $\omega = 0$. These are equivalent to the Landau levels for the quantized motion of a charged particle in a uniform magnetic field. Consider the $xy$ motion of a particle of charge $e$ in a magnetic field $\mathbf{B} = B\hat{z}$, governed by the Hamiltonian $H_{L.L.} = \frac{1}{2M}(\mathbf{p} - \frac{e}{c}\mathbf{A})^2$ (intrinsic spin ignored). With the symmetric gauge for the vector potential, $\mathbf{A} = \frac{1}{2}(\mathbf{B} \times \mathbf{r}) = (-\frac{1}{2}B\,y, \frac{1}{2}B\,x, 0)$, and $e \equiv -|e|$, the Hamiltonian reduces to

$$H_{L.L.} = \frac{1}{2M}\mathbf{p}^2 + \frac{1}{2}M\omega_L^2\,(x^2 + y^2) + \omega_L\,l_z\,, \tag{2.13}$$

where $\omega_L = \frac{|e|B}{2Mc}$ is called the Larmor frequency. This is equivalent to $H$ in Eq.(2.10) for $\omega = \Omega \equiv \omega_L$. The eigenvalues $\{E_{n_r,l}\}$ of Eq.(2.11) in this case, i.e., the Landau

levels, can be written as

$$E_n = \left(n + \frac{1}{2}\right)\hbar\omega_c\,, \qquad n = n_r + \frac{l+|l|}{2} = 0, 1, 2, \ldots\,, \tag{2.14}$$

in terms of the cyclotron frequency $\omega_c = 2\,\omega_L \equiv 2\,\Omega$.

For a free charged particle in a magnetic field, if the field is weak enough, the quadratic term in $B$ in Eq.(2.13) may be neglected against the kinetic energy as well as the linear Zeeman term. Then the Hamiltonian $H_{L.L.} \simeq \frac{\mathbf{p}^2}{2M} + \omega_L l_z$ can be regarded as that for a free particle in a rotating frame ; $\omega = \omega_L$ and $H_0 = \frac{\mathbf{p}^2}{2M}$ in the LHS of Eq.(2.10). We will see in later chapters the same effect as the cranking on level structure, in an electron system in a weak magnetic field.

As obvious from Eq.(2.14), the Landau levels are the energy levels of a one-dimensional harmonic oscillator of frequency $\omega_c$, each level having a degeneracy coming from the extra dimension in the system. The degeneracy of each Landau level is determined by the number of flux quanta ($\frac{hc}{|e|}$) available for a given field strength, $\frac{|e|}{hc}B\mathcal{A}$, where $\mathcal{A}$ is the area of the system. Therefore, if there is no boundary in the system and hence the area is infinite, as in the current system under consideration, the degeneracy will be infinite. This can be seen in the definition of the quantum number $n$ in Eq.(2.14), as zero and negative angular momenta $l = 0, -1, -2, \ldots, -\infty$ all result in the same energy for a fixed nodal quantum number $n_r$. This is indicated in Fig.2.3, where the zero and first few negative angular momenta are labelled for the corresponding levels that are converging to the lowest Landau level ($n_r = 0$).

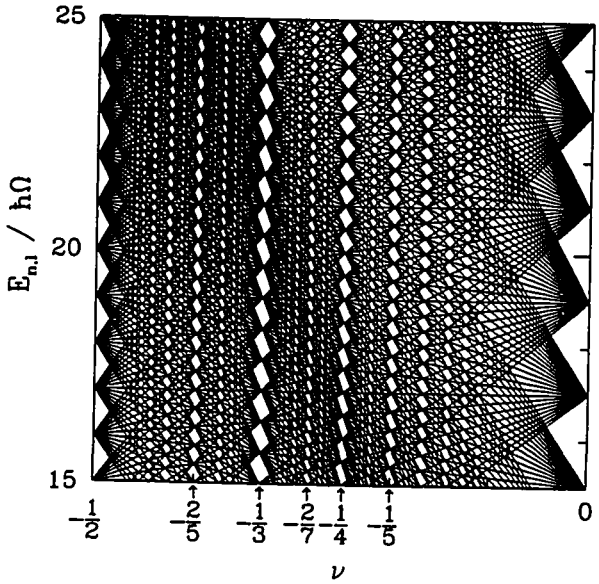


Figure 2.4: The same spectrum as in Fig.2.3, in the range $-\frac{1}{2} \leq \nu \leq 0$ for higher energies.

Thus all the states in the lowest Landau level have aligned (but different) angular momenta, and originate from different shells of the isotropic oscillator. Although this result is well known in the literature, its diagrammatic description through a cranked oscillator is not commonly shown. The pattern of the spectrum in Fig.2.3 for $\nu > 0$ is new, and has some interesting features which we explore in the next section.

Also in the range $-\frac{1}{2} \leq \nu < 0$, the convergence of the states to the Landau levels is preceded by a zig-zag repeating pattern formed by a series of quantum gaps. This is shown for higher energy in Fig.2.4. These gaps appear at values of the cranking frequency $\omega$ for which $\omega/\Omega$ is a rational number, a fact that relates these shell gaps with the occurrence of classical periodic orbits. This may be readily seen by looking

at the solutions of the classical equations of motion. Using the coordinate $z = x + iy$, the equations of motion for the Hamiltonian Eq.(2.10) may be written concisely as

$$\ddot{z} = (\omega^2 - \Omega^2)\, z + 2i\,\omega\dot{z}\,. \tag{2.15}$$

The first term on RHS consists of the centrifugal and the harmonic forces, and is attractive for the cranking frequency $\omega < \Omega$, and repulsive for $\omega > \Omega$ beyond the Landau levels. The second term is the Coriolis force that causes the particle to rotate about the direction of the rotation. The general solution of the above equation is

$$z = A\, e^{i\omega_+ t} + B\, e^{-i\omega_- t}\,, \tag{2.16}$$

where $A$ and $B$ are constants, and $\omega_\pm = \Omega \pm \omega$ are the two normal-mode frequencies for $\omega \neq \Omega$ ($\omega_-$ is negative for $\omega > \Omega$). When the ratio of these two frequencies is a rational fraction, thus with a rational $\nu = -\omega_-/(\omega_+ + \omega_-)$, closed periodic orbits are formed. If the two frequencies are incommensurate, the orbits will be in general Lissajous figures which will never close and eventually cover the whole space within a boundary set by the energy. In Fig.2.5 some of the closed orbits are shown for various values of $\nu$.

Quantum mechanically, it can be shown that the spectrum (2.11) is identical to that of the anisotropic oscillator with frequencies $\omega_\pm$, by introducing the following operators [Messiah 61]:

$$a_\pm = \frac{1}{\sqrt{2}}\,(a_x \mp i\, a_y)\,, \qquad a_\pm^\dagger = \frac{1}{\sqrt{2}}\,(a_x^\dagger \pm i\, a_y^\dagger)\,, \tag{2.17}$$

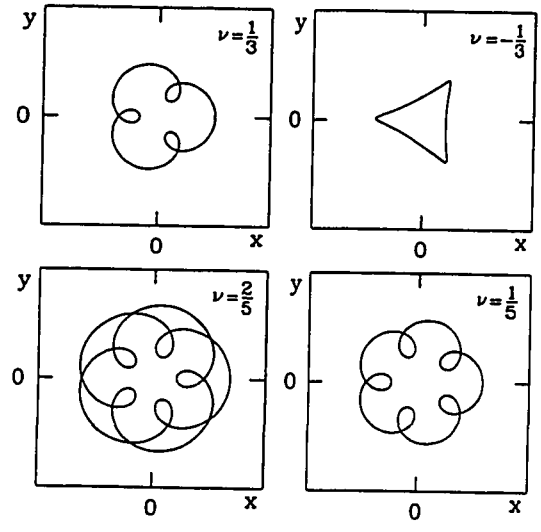


Figure 2.5: Classical periodic orbits of a particle obeying (2.16) for various rational $\nu$.

where $a_i$ and $a_i^\dagger$ ($i = x, y$, or $i = \pm$) are the annihilation and creation operators of quanta of type $i$, and $a_{x,y}$ and $a_{x,y}^\dagger$ are defined by the (scaled) coordinates and momenta as $a_x = \frac{1}{\sqrt{2}}(x + ip_x)$ etc. For the isotropic oscillator, either set of the operators diagonalizes the Hamiltonian as $H_0 = (n_x + n_y + 1)\,\hbar\Omega = (n_+ + n_- + 1)\,\hbar\Omega$, where $n_{x,y} = n_\pm = 0, 1, 2, \ldots$. The angular momentum, however, can be expressed only in terms of the numbers of '+ quanta' and of '− quanta', as $l_z = (n_+ - n_-)\,\hbar$. Hence, the eigenspectrum of $H$ in Eq.(2.10) may be written as

$$E_{n_+,n_-} = \left(n_+ + \frac{1}{2}\right)\hbar\omega_+ + \left(n_- + \frac{1}{2}\right)\hbar\omega_- , \qquad n_\pm = 0, 1, 2, \ldots , \tag{2.18}$$

with $\omega_\pm = \Omega \pm \omega$. Like the isotropic oscillator, the accidental degeneracies of the levels that arise when the ratio of the two frequencies is rational [Louck 73] are associated

with dynamical symmetry of the system, which is not obvious from the geometrical shape of the potential itself.

For the special case of $\omega = \Omega$, the centrifugal force exactly cancels the attractive harmonic force, and the equations of motion (2.15) reduce to $\ddot{z} = i\omega_c \dot{z}$, with $\omega_c = 2\Omega$. Taking the time derivative on both sides once more, $\frac{d^2}{dt^2}\dot{z} = -\omega_c^2 \dot{z}$, thus $\dot{z} = A\, e^{i\omega_c t}$. This may be written as $v_x = \dot{x} = v\cos(\omega_c t + \alpha)$ and $v_y = \dot{y} = v\sin(\omega_c t + \alpha)$, where $v^2 = v_x^2 + v_y^2 = \frac{2E}{M}$ and $\alpha$ a constant. The orbital motion is circular and given by

$$x = X + \frac{v_y}{\omega_c}\,, \qquad y = Y - \frac{v_x}{\omega_c}\,, \tag{2.19}$$

with an arbitrary centre $(X, Y)$. These are the cyclotron orbits. The equations of motion above, $\dot{v}_x = -\omega_c v_y$ and $\dot{v}_y = \omega_c v_x$, are identical to those for the canonical variables $(q, p)$ in the one-dimensional oscillator $H = \frac{1}{2M}p^2 + \frac{1}{2}M\omega_c^2 q^2$, $\dot{p} = -M\omega_c^2 q$ and $\dot{q} = p/M$, if we take $(v_y/\omega_c, Mv_x)$ as conjugate variables. Note that the Hamiltonian $H_{L.L.}$ depends on only these two variables, $H_{L.L.} = \frac{1}{2}M(v_x^2 + v_y^2)$. We can thus see that the quantized cyclotron motion results in the spectrum (2.14), same as for the one-dimensional oscillator, where $v_x$ and $v_y$ satisfy the commutation relation $[v_y/\omega_c, Mv_x] = i\hbar$. As the system is two-dimensional, there is another set of conjugate variables, which is the position of the centre $(X, Y)$. These variables commute with the Hamiltonian $H_{L.L.}$ and are conserved, but cannot be determined simultaneously since they don't commute with each other ($[X, M\omega_c Y] = i\hbar$). In fact, they satisfy the uncertainty relation $\Delta X \Delta Y = 2\pi l_0^2$, where $l_0 = \frac{\hbar c}{|e|B}$ is the magnetic length. This

uncertainty in the position of each "orbit", or state, gives rise to the degeneracy of a Landau level, $\frac{1}{2\pi l_0^2} = \frac{|e|B}{hc}$, per unit area. One can visualize the quantized "orbital" motion in terms of coherent states that are Gaussian wave packets following the cyclotron orbits [Malkin 69, Feldman 70].

Apart from this special case, where the period of the (only) primitive orbits is half of that of the (only) primitive orbits in the isotropic oscillator ($\omega = 0$), prominent gaps appear in Figs. 1 and 2 at simplest fractions of $\omega_+/\omega_-$. For example, the large gaps at $\nu = \pm 1/3$ correspond to the situation $\omega_+ : |\omega_-| = 2 : 1$.

### 2.2.2 Cranking beyond the Landau levels

Let us now examine the quantum states that are condensing at various fractional values of $\nu$ for $\omega \geq \Omega$. For convenience, we choose to study the states converging at the energy of the lowest Landau level, $E = \hbar\Omega$. Since the cranking does not change the nature of quantum states, wave functions are given by those of the isotropic oscillator. Defining the length scale for the isotropic oscillator $a_0 = \sqrt{\frac{\hbar}{M\Omega}}$, the (unnormalized) wave functions may be written as a product of Hermite polynomials with quantum numbers $n_x$ and $n_y$, as $\psi_{n_x,n_y}(x,y) = H_{n_x}(x/a_0)H_{n_y}(y/a_0)e^{-(x^2+y^2)/2a_0^2}$ [French 78]. At the isotropic-oscillator end, if we denote the shells by $N = n_x + n_y = 2n_r + |l| = 0, 1, 2, \ldots$, the maximum angular momentum (in units of $\hbar$) for a given shell is $|l| = N$. At $\omega = \Omega$, the nodeless ($n_r = 0$) states with the negative maximum $l = -N$ from each

shell converge into the lowest Landau level. One can construct the eigenfunctions of $l_z$ from linear combinations of $\{\psi_{n_x,n_y}\}$ for each oscillator shell $N$, and those with $l = -N$ are written as a function of $z = x + iy$ in the normalized form :

$$\psi_{N,\, l=-N}(z) = \frac{1}{\sqrt{\pi}} \frac{1}{\sqrt{N!}} \frac{1}{a_0^{N+1}} (z^*)^N e^{-|z|^2/2a_0^2}, \tag{2.20}$$

where $z^* = x - iy$. The resulting degeneracy per unit area at $\omega = \Omega$ is easily calculated by summing the absolute squares of these functions for $N = 0, \ldots, \infty$, and found to be $\eta_0 = \frac{1}{\pi a_0^2}$. This is equal to $\frac{1}{2\pi l_0^2} = \frac{|e|B}{hc}$ for $2\Omega = \omega_c$, as obtained above.

Now we proceed to examine the level structure in Fig.2.3 beyond the Landau levels. The repeating pattern in this region is known as a Farey fan, which has been studied in the context of number theory and continued fractions [McIlroy 92, Lagarias 92]. The Farey fan of order $k$ on the $xy$ plane consists of lines $y = -ax + b$, where $a$ and $b$ are integers and $a \leq k$. The $x$-intercepts of these lines between 0 and 1 form the Farey series of order $k$ that is the ascending sequence of fractions $p/q$, where $0 \leq p \leq q \leq k$ [Niven 1991]. The pattern in Fig.2.3 for $0 < \nu < 1$ is the Farey fan of order $k \to \infty$. The Farey series (the values of $\nu$ at which shell gaps are present) can be obtained by a sequence of division of the unit interval $[0, 1]$ by mediants : The mediant for two "Farey neighbours" $p_1/q_1$ and $p_2/q_2$ ($|p_1 q_2 - p_2 q_1| = 1$) is defined by [Lagarias 92]

$$\frac{p_1}{q_1} \oplus \frac{p_2}{q_2} = \frac{p_1 + p_2}{q_1 + q_2}. \tag{2.21}$$

That is, we start from dividing $[\frac{0}{1}, \frac{1}{1}]$ by their mediant $\frac{0}{1} \oplus \frac{1}{1} = \frac{1}{2}$, then split the two subintervals $[\frac{0}{1}, \frac{1}{2}]$ and $[\frac{1}{2}, \frac{1}{1}]$ by mediants $\frac{1}{3}$ and $\frac{2}{3}$, respectively, and so on.

At the energy $E = \hbar\Omega$, inspection of the level at $\nu = 1/m$, with $m$ an integer larger than 1, reveals that the number of converging states is exactly a fraction $1/m$ of the Landau level. For example, the successive isotropic-oscillator states meeting at $\nu = \frac{1}{3}$ at $E = \hbar\Omega$ have angular momenta $l = 0, -3, -6$, and so on. This is shown in Fig.2.6. Thus, for every triplet of adjacent states in the lowest Landau level, e.g., $(0, -1, -2)$, there is one state ($l = 0$ in this case) at $\nu = \frac{1}{3}$. Similarly, at $\nu = \frac{1}{5}$, the degeneracy per area is $\frac{1}{5}\eta_0$. As clearly seen in Fig.2.6 for $\nu = \frac{1}{3}$, the single-particle states collapsing at $\nu = 1/m$ are each from a separate Landau level, and have increasing number of nodes. Note that all the negative-$l$ states in the $n$-th Landau level ($n = 0, 1, 2, \ldots$) have the node number $n_r = n$ (see Eq.(2.14)). It is thus clear, for example, that the states with $l = 0, -3, -6, -9$, etc. converging towards $\nu = \frac{1}{3}$ have nodes $0, 1, 2, 3$, etc., respectively. At $\nu = \frac{1}{5}$, similarly, the $l = 0$ state has no node, the next state with $l = -5$ has one node, the $l = -10$ state has two nodes, and so on.

We may call the condensed levels at $\nu = 1/m$ as 'mothers', since these shell gaps give rise to a succession of 'daughters' as seen in Fig.2.6. One state from each quantum shell of the $\nu = \frac{1}{3}$ mother converges at $E = \hbar\Omega$, constituting the daughter at $\frac{2}{5}$, just as the mother herself was formed from the collapse of the states from each Landau level. The Landau levels, in turn, were each formed by the collapse of the states from the separate oscillator shells. The next-generation daughter for the $\nu = \frac{1}{3}$ family is formed at $\frac{3}{7}$, with the states from each shell at $\frac{2}{5}$. The successive convergence at $E = \hbar\Omega$ in this family is indicated by the thick lines in Fig.2.6. The single-particle

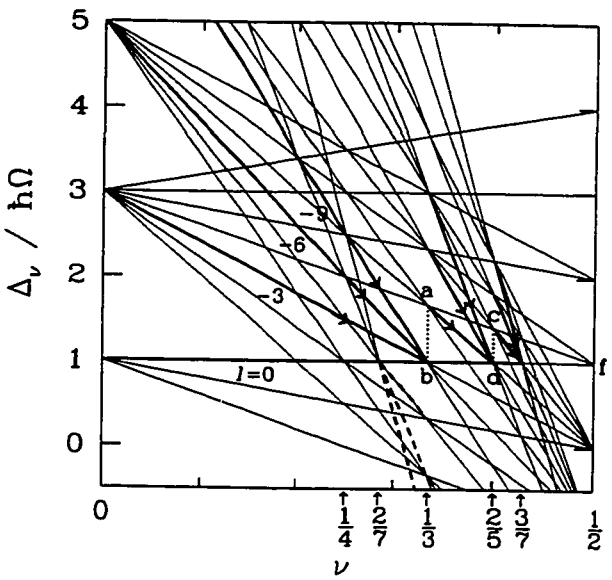


Figure 2.6: The 'mother-daughter' sequence of degenerate levels. One state from each Landau level converges at $\nu = \frac{1}{3}$ to form a mother, and similar convergence from the mother yields the daughter at $\frac{2}{5}$. Only a few converging lines are shown for clarity. The vertical lines ab and cd show the gaps at $\nu = \frac{1}{3}$ and $\frac{2}{5}$, respectively.

states converging at the daughters have different nodal structures than that of the mothers. Consider, for example, the daughters at $\nu = \frac{2}{5}$ and $\frac{3}{7}$ at $E = \hbar\Omega$. From Eq.(2.11), all the states at this energy obey the equation

$$(2n_r + |l|)\,\hbar\Omega + l\,\hbar\omega = 0\,. \tag{2.22}$$

It immediately follows that the converging states at $\nu = \frac{2}{5}$ have (other than $n_r = 0$ for $l = 0$) $n_r = 2$ for $l = -5$, and $n_r = 4$ for $l = -10$, etc. Similarly for $\nu = \frac{3}{7}$, $n_r = 3$ for $l = -7$, $n_r = 6$ for $l = -14$, and so on. That is, for the successive states at $\nu = p/q$, the angular momenta are multiples of $q$ and the nodes increase by $p$. A similar construction of different families is possible with even-denominator mothers, but then the daughters have alternately even and odd denominators.

The complexity of the structure in the quantum states is also reflected in the classical periodic orbits, some of which are shown in Fig.2.5. From this figure, we note that the number of loops in the orbit for $\nu = p/q$ ($> 0$) is determined by the denominator $q$. The loops result from the competition between the centrifugal force (the now repulsive first term in Eq.(2.15)) that pushes away the particle from the centre, and the Coriolis force that makes the particle rotate anticlockwise. It is seen in Fig.2.5 that both $\nu = \frac{1}{5}$ and $\nu = \frac{2}{5}$ have periodic orbits with five loops, while the $\nu = \frac{2}{5}$ orbit has a more complicated structure. The denominator $q$ of $\nu = p/q$ also determines the magnitude of the quantum gap. In Fig.2.6, we see that the gap at

$\nu = p/q$ is given by

$$\Delta_\nu = \frac{\hbar\omega_c}{q}\,, \tag{2.23}$$

and these gaps are shown for $\nu = \frac{1}{3}$ and $\frac{2}{5}$ in dotted lines.

It is worth mentioning that the sequence of the gaps generated by this dynamical model for $\nu > 0$ are the same, for the odd denominators, as the Haldane hierarchy [Haldane 83] in the fractional quantum Hall effect (FQHE) [Tsui 82, Du 93], where $\nu = p/q$ is the filling fraction of the Landau level. The hole-state sequences for the odd denominators in this hierarchy, e.g., $(\frac{2}{7}, \frac{3}{11}, \frac{4}{15}, \ldots)$, are generated in our model by the convergence of lines from the lower side of the $E = \hbar\Omega$ line. In Fig.2.6 the convergence from the $\nu = \frac{1}{3}$ mother to the 'hole-daughter' at $\frac{2}{7}$ is shown by the dashed line. The FQHE states, however, have a very different structure than the ones in our independent-particle model. In FQHE, the single-particle states of the lowest Landau level, (2.20), are thoroughly mixed by the Coulomb interaction among the electrons, and the many-body wave functions have highly-correlated nature of incompressible quantum fluid. In these states, there is little mixing of states from different Landau levels. By contrast, the wave functions generated by our model has thorough inter-Landau level mixing, and has no two-body correlations. Nevertheless, it is interesting that this integrable single-particle model generates a sequence of quantum gaps resembling the Haldane ones.

## 2.3 Summary

In this chapter, we have studied the spectrum of a particle in a two-dimensional cranked harmonic oscillator. We have graphically shown a series of shell gaps that are formed as the cranking frequency is varied, and their direct connection to the classical periodic orbits. We have also depicted the formation of the Landau levels when the cranking frequency equals to the oscillator frequency, thus showing the analogy between the cranking and the application of a homogeneous magnetic field in the system of charged particles. Furthermore, this is perhaps the simplest quantum model that generates the Farey fan pattern. In the following two chapters, we proceed to study shell structure of finite electron systems in an external uniform magnetic field. Analogously to the cranking, the system exhibits different shell structures as the magnetic field is varied, and these changes will be examined in connection to shortest periodic orbits in the corresponding classical system.

# Chapter 3

# Simple Metal Clusters in Magnetic Fields

## 3.1 Introduction

The system of simple metal clusters has been studied extensively for the last decade [de Heer 93, Brack 93], especially since the first observation of electronic shell structure of alkali metal clusters in early 1980s [Knight 84, Knight 85]. Metal clusters are small particles made up of metallic atoms, whose number varies from just a few to tens of thousands. This system is thus in the interesting region that bridges the microscopic system of atoms and the macroscopic system of bulk metals, and is often called "mesoscopic".

In a typical device for producing metal clusters, the metal is vaporized in a hot

oven and the vapor is pressured by an inert gas into a fine nozzle, through which it is expanded into a vacuum. During the expansion, the metal vapor is cooled down and condenses into clusters, some of them further cooling down by evaporating an atom or more. The mass abundances of clusters thus formed can be observed by time-of-flight mass spectrometry, in which clusters are ionized and accelerated by an electric field, and their charge-to-mass ratios are determined from the measured time of flight. The abundance spectra reflect the stability of the clusters. Clusters with the "magic numbers" of atoms are more stable, and are more abundant after cooling (through evaporating atoms). The striking order in the mass spectrum of sodium clusters first found for number of atoms $\lesssim$ 100 [Knight 84] was immediately identified as shell structure of valence electrons. Furthermore, later observation of the abundances of sodium clusters [Pedersen 91] has revealed not only the existence of the shell structure with up to 3000 valence electrons, but also "supershell" structure, a long wave-length, beating modulation of the electronic shell structure. This is shown in Fig.3.1 as a function of the atomic number $N^{1/3}$. In order to make the shell oscillations stand out, the logarithmic derivative of the intensity $I_N$ (for clusters with $N$ atoms) is plotted. It is defined by

$$\Delta_1 \ln I_N = \ln I_{N+1} - \ln I_N \simeq \frac{d\ln I_N}{dN} \simeq 2\frac{(I_{N+1} - I_N)}{(I_{N+1} + I_N)}, \tag{3.1}$$

so that the magic numbers appear at dips. In Fig.3.1, furthermore, factors of $N^{1/2}$ and $e^{cN^{1/3}}$ are multiplied to $\Delta_1 \ln I_N$ to compensate the effect of the temperature and the

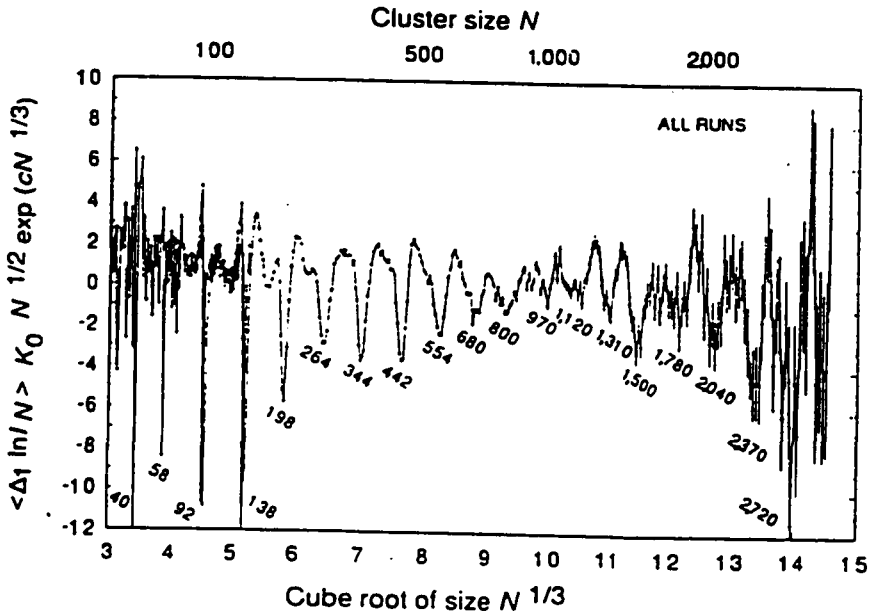


Figure 3.1: The abundance spectrum of sodium clusters [Pedersen 91] as a function of the cube root of the atomic number $N^{1/3}$. The logarithmic derivative of the intensity $I_N$ is plotted in order to make the shell structure stand out.

large size of the clusters, which tend to damp out the shell amplitudes [Pedersen 91, Bjørnholm 90].

The shell structure is well understood in terms of the quantized motion of delocalized valence electrons moving in a spherical "jellium" background, in which ion structures are replaced by a uniform distribution of positive charge. The mean-field potential may be approximated by a harmonic oscillator for smaller clusters ($\lesssim 40$ atoms) and by a potential with flat bottom and steep walls for larger clusters. The large clusters may be regarded to first order as a free electron gas confined in a spherical cavity with perfectly reflecting walls, and the supershell structure can be repro-

duced very well by this simple model [Balian 72]. The supershells can be explained semiclassically as an interference effect between the classical triangular and square periodic orbits of electrons in the cavity. This can be seen as follows. As discussed in Chapter 1, in periodic orbit theory, the oscillating part of the quantum density of states $\delta g(E)$ is written as a sum over contributions from all the classical periodic orbits in the system. Each periodic orbit $i$ contributes in the form $A_i \sin(S_i/\hbar + \alpha_i)$, where $A_i$ and $\alpha_i$ are constants and in the cavity system, $S_i/\hbar = kL_i$ with wave number $k$ and the length of the closed orbit $L_i$. In the spherical cavity, the planar orbits of triangular and square shape have dominant contributions, with comparable amplitudes. Their contributions add up to yield the beating effect :

$$\sin(kL_\triangle) + \sin(kL_2) \simeq 2\sin(kL)\cos(k\Delta L/2) \ , \tag{3.2}$$

where the average orbital length $L = (L_\triangle + L_2)/2$ and $\Delta L = (L_2 - L_\triangle)$, and the constant phases have been ignored. The slight difference in the orbit lengths, $\Delta L$, results in the long wave-length oscillation that envelopes the faster shell oscillations with period determined roughly by the triangular orbit. The shell correction $\delta E = E_{tot} - \tilde{E}_{tot}$ $(eV)$ calculated in the spherical cavity model for zero temperature is shown in Fig.3.2. The shell and supershell structure is more enhanced than in the measured spectrum in Fig.3.1, due to smearing effect by the finite temperature of the clusters in the latter. The beating pattern between the classical triangular and square orbits is clearly seen.

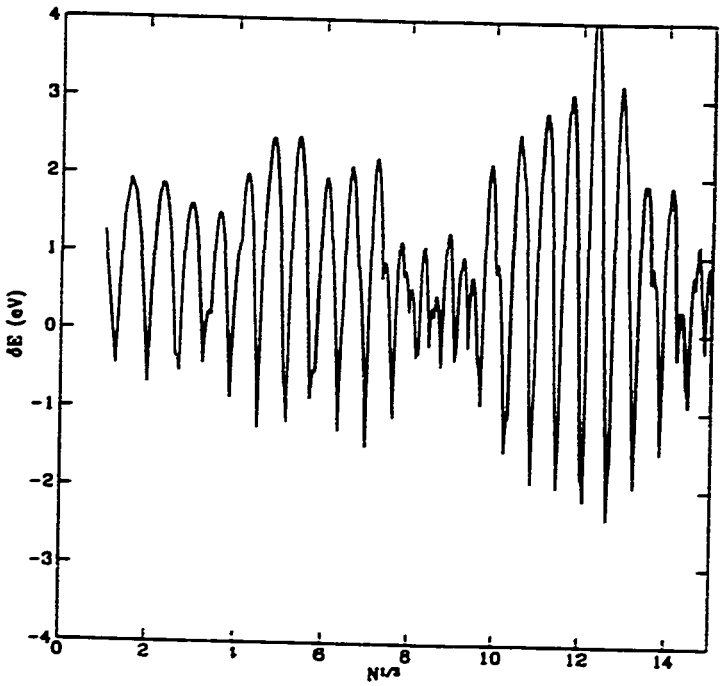


Figure 3.2: Shell correction $\delta E = E_{tot} - \tilde{E}_{tot}$ $(eV)$ for electrons in the metal clusters modelled by a spherical cavity with perfectly reflecting walls, as a function of $N^{1/3}$.

In this chapter, we examine what happens to this supershell structure if a uniform magnetic field is applied to the system. This is an interesting question especially from the semiclassical point of view, as the classical dynamics is dramatically changed under the field. In particular, the classical action of a given orbit will change to first order in the field, by the amount proportional to the magnetic flux enclosed by the original orbit. Thus there will be an additional relative phase between the triangular and square orbits in Eq.(3.2), proportional to the difference in their enclosing areas. As the area difference is larger compared to the length difference $\Delta L$, it is interesting to see how this change will affect the supershell structure. We study the problem by exact quantum-mechanical calculations and also semiclassically in connection with classical orbits.

# Simple metal clusters in magnetic fields

Kaori Tanaka
*Department of Physics and Astronomy, McMaster University, Hamilton, Ontario, Canada L8S 4M1*

Stephen C. Creagh* and Matthias Brack
*Institut für Theoretische Physik, Universität Regensburg, D-93040 Regensburg, Germany*
(Received 29 December 1995)

The electronic supershell structure of simple metal clusters in a uniform magnetic field is studied with a spherical infinite-well potential as a simple yet realistic model for confining the valence electrons. It is found that there is little perceivable change in the supershells with experimentally achievable field strengths. If yet stronger fields are applied, the supershell structure gets destroyed and then new beat structures come about as the field strength increases further. These phenomena are explained by a recently derived semiclassical trace formula for broken symmetry that has been applied to the present system. [S0163-1829(96)01824-3]

## I. INTRODUCTION

One of the most prominent features of simple metal clusters is the existence of electronic shell structure.[1,2] Moreover, it is fascinating that for these systems, unlike for atoms and nuclei, the number of particles — i.e., here of valence electrons — can go up to the order of $10^3-10^4$ or possibly even more.[1] Thus the systems can be made so large that they have opened up new possibilities for studying shell structure effects in free finite fermion systems of mesoscopic sizes. The so-called "supershells," a beating pattern in their electronic shell structure that has been observed for alkali[3,4] and other simple metal clusters,[5] form a striking example. This supershell structure is remarkably well explained in the simple picture of independent valence electrons moving in a spherical, uniform ionic background formed by only a few atoms to about 3000 atoms or more. It is amazing that this quantum-mechanical phenomenon can also be understood semiclassically in terms of periodic orbit theory.[6] In the present paper, we study what happens to this supershell structure if a uniform magnetic field is applied to the clusters, and how we can understand the quantum-mechanical results semiclassically.

The supershell structure was found by Balian and Bloch more than twenty years ago, at that time in a mathematical model that was motivated by nuclear systems, but with particle numbers too large to be realized experimentally.[6] They considered a system of particles confined in a spherical cavity with perfectly reflecting walls and calculated its level density, which exhibits a pronounced beating pattern. They could explain this beat semiclassically as being due mainly to the interference of the classical periodic orbits of triangular and square shape. Nishioka, Hansen, and Mottelson[7] later showed that the same interference effect occurs also for particles in more realistic smooth potentials suitable for alkali-metal clusters. Their results were confirmed in self-consistent Kohn-Sham calculations within the spherical jellium model using the local-density approximation.[8] The theoretical predictions triggered the first experimental observation of supershells for Na clusters.[3]

Although the spherical cavity studied by Balian and Bloch[6] is an extremely simple model for the effective potential felt by the valence electrons in metal clusters, it reproduces the gross-shell and supershell structure in Na and Li clusters surprisingly well.[2,3] In fact, the "magic numbers" of the spherical main-shell closures found in the cavity model are identical (except for clusters with $N<50$ valence electrons) with those found in the self-consistent jellium model[8] and agree with those observed experimentally[3,4] within their statistical uncertainties. The spherical cavity thus has proven to be a very simple, yet sufficiently realistic model for the mean field felt by the valence electrons in large clusters of simple metals. (This includes not only the external field of the ions, but also the average part of the Coulomb interaction amongst the valence electrons, including exchange and correlations in the spirit of density functional theory; see Refs. 2 and 8 for details.) We shall therefore use this model in our extension of the previous semiclassical studies to the inclusion of a magnetic field.

In the periodic orbit theory,[6,9] the oscillating part $\delta g(E)$ of the quantum level density for a given Hamiltonian is approximated semiclassically by a so-called trace formula, which relates the Fourier components of the oscillations to the actions and stability properties of the closed periodic orbits of the corresponding classical system. For the spherical cavity, the periodic orbits are all planar polygons that may be classified by their number of wall reflections $p$ and their number of turns around the center of the sphere $t$, with $p\geq 2t$. The trace formula derived by Balian and Bloch for the oscillating part of the level density of the spherical cavity reads

$$\delta g(E)=\sqrt{\frac{kR}{\pi}}\sum_{t=1}^{\infty}\sum_{p=2t+1}^{\infty}(-1)^t\sin 2\phi_{pt}\times\sqrt{\frac{\sin\phi_{pt}}{p}}\sin\left(\frac{S_{pt}(E)}{\hbar}-3p\frac{\pi}{2}+\frac{3\pi}{4}\right)-\sum_{t=1}^{\infty}\frac{1}{2\pi t}\sin\left(\frac{S_{2t,t}(E)}{\hbar}\right),\quad \phi_{pt}=\pi\frac{t}{p}. \tag{1}$$

0163-1829/96/53(23)/16050(9)/$10.00





Reprinted from Phys. Rev. B53, pp.16050-16058 (1996).

where $R$ is the radius of the cavity, $k$ the wave number of the particle, and $S_{pt}(E)=\hbar k L_{pt}$ is the action of the orbit with length $L_{pt}=2pR\sin\phi_{pt}$. Here the natural energy unit for this system, $E_0=\hbar^2/2m_eR^2$ with $m_e$ the mass of the particle, is set to unity. Shorter orbits (smaller $p$) have larger contributions to $\delta g$, and orbits with $p>2t$ contribute more than the diametrical ones ($p=2t$) because of their larger degeneracy (see the discussion at the beginning of Sec. III). In fact, the contribution from the diametrical orbits [the second term in Eq. (1)] is negligibly small and hence the triangular ($p=3$) and square ($p=4$) orbits give the leading contributions. Since the shortest orbits are responsible for the gross-shell structure of the level density, it is the interference of the triangular and squared orbits, due to the slight differences between their orbital lengths and amplitudes in the trace formula (1), that explains the beating supershell pattern.

Quantum mechanically, the shell effects in $\delta g$ come from the fact that the quantized energy levels are degenerate, due to the spherical symmetry, and further bunched into the so-called "main shells." In order to display the gross-shell features in the quantum-mechanical $\delta g(E)$, we average over an energy interval $\gamma$ that is smaller than the main-shell spacing but slightly larger than the typical distance of neighboring levels within a main shell. Applying the same averaging to the trace formula leads naturally to the suppression of contributions from long periodic orbits.

If a uniform magnetic field is applied to this system, the electron classically feels a constant Lorentz force in the plane perpendicular to the field. The classical orbits will therefore change and have actions different from those without the field. The orbits will be spirals with constant curvature, and most of the orbits will no longer close within the spherical boundary. It is to be expected that the shell structure might be very sensitive to the changes in actions that come into the phase of $\delta g$. In particular, these changes will affect the relative lengths of the triangular and square orbits and therefore modify the supershell structure. How this modification depends on the strength of the magnetic field is the object of our present study. If the field is weak enough, the change in the classical action of a given orbit can be approximated to first order in the field strength $B$, and will result simply in an additional phase in (1) proportional to the magnetic flux enclosed by the original orbit.

In Sec. II we study the quantum-mechanical level density in the presence of a magnetic field, and in Sec. III we examine the problem semiclassically. We will discuss the results and related problems in Sec. IV.

## II. QUANTUM CALCULATIONS IN THE PRESENCE OF A MAGNETIC FIELD

In the absence of an external field, the quantum-mechanical eigenvalues of the cavity are given by the zeros of the spherical Bessel functions. The (unnormalized) wave functions are written as $\psi_{n,l,m}(\mathbf{r})=j_l(k_{n,l}r)Y_{l,m}(\theta,\phi)$, where $j_l$ are the spherical Bessel functions of $l$th order and $Y_{l,m}$ the spherical harmonics, and $l=0,1,2,\ldots$ and $m=-l,\ldots,l$ are the angular-momentum projection quantum numbers. $k_{n,l}R$ is the $n$th zero of $j_l$ with nodal quantum number $n=1,2,3,\ldots$, which yields the energy eigenvalue $\varepsilon_{n,l}=\hbar^2k_{n,l}^2/2m_e$. In the presence of a uniform magnetic field $\mathbf{B}=B\mathbf{e}_z$, the single-particle Hamiltonian can be written, in the symmetric gauge $\mathbf{A}=\frac{1}{2}\mathbf{B}\times\mathbf{r}$, as

$$\hat{H}=\frac{1}{2m_e}\mathbf{p}^2+\omega_L L_z+\frac{1}{2}m_e\omega_L^2(x^2+y^2)+V(r), \qquad (2)$$

where $V(r)=0$ inside the cavity, $r<R$, and $V(r)=\infty$ outside, $r\geq R$. Here $m_e$ is the electron mass and $\omega_L=eB/2m_ec$ the Larmor frequency ($e>0$); the electron spins are neglected. Now the spherical symmetry is broken by the third term in the right-hand side (rhs) of Eq. (2), whereas $L_z=m\hbar$ is still a good quantum number though its degeneracy is now removed by the Zeeman term. We diagonalize the Hamiltonian (2) in the basis of the cavity wave functions $\{\psi_{n,l,m}\}$ in order to obtain its energy eigenvalues. In the actual calculations, we scale the Hamiltonian by the natural energy unit $E_0=\hbar^2/2m_eR^2$. Then it depends on the size $R$ of the cluster and on the magnetic field strength $B$ only through one dimensionless parameter $\kappa$, given by

$$\kappa=\left(\frac{R}{l_0}\right)^2=\frac{eB}{\hbar c}R^2, \quad l_0=\sqrt{\frac{\hbar c}{eB}}, \qquad (3)$$

where $l_0$ is the so-called magnetic length. In the following discussions we take all energies in units of $E_0$.

We are interested in the quantum-mechanical $\delta g(E)$ and to see how the supershell structure is affected by the magnetic field. We slightly smooth the quantum level density $g(E)=\Sigma_i\delta(E-E_i)$, replacing each $\delta$ function by a normalized Gaussian $e^{-[(E-E_i)/\gamma]^2}/\gamma\sqrt{\pi}$. We take the smoothing width $\gamma$ to be proportional to $\sqrt{E}$, which corresponds to smoothing over $kR=\sqrt{E}$ with a constant width. In the case without field, $\sqrt{E}=kR$ is the natural energy variable for the level density, since the quantum eigenvalues $\{k_{n,l}R\}$ for a given $l$ are asymptotically given by the zeros of a cosine function, hence equally spaced in $kR$. It can also be seen in the trace formula Eq. (1) that $\delta g(E)$ oscillates regularly as a function of $kR$. In the presence of a magnetic field we still look at the level density as a function of $kR=\sqrt{E}$, which is now the (dimensionless) mechanical momentum of an electron rather than its canonical momentum. $kR$ remains a proper variable for the reasons above as long as the perturbation due to the field is not too large, as we will see below. We take the smoothing width $\gamma=0.8\sqrt{E}$, which corresponds to smoothing with a constant width of $\gamma=0.4$ in the variable $kR$.

The oscillating part $\delta g(E)$ of the level density is then obtained by subtracting from $g(E)$ its smoothly varying part $\bar{g}(E)$. For the spherical cavity system without external field, this smooth part is analytically given by[10]

$$\bar{g}(E)=\frac{kR}{3\pi}-\frac{1}{4}+\frac{1}{3\pi kR}, \qquad (4)$$

where $kR=\sqrt{E}$ as stated above. It turns out that the first terms in this expansion are unchanged when magnetic field is included. We have checked this numerically by the smoothing described above with a width $\gamma$ large enough to wipe out all shell structure. We will therefore use the analytical expression (4) also when the magnetic field is present.

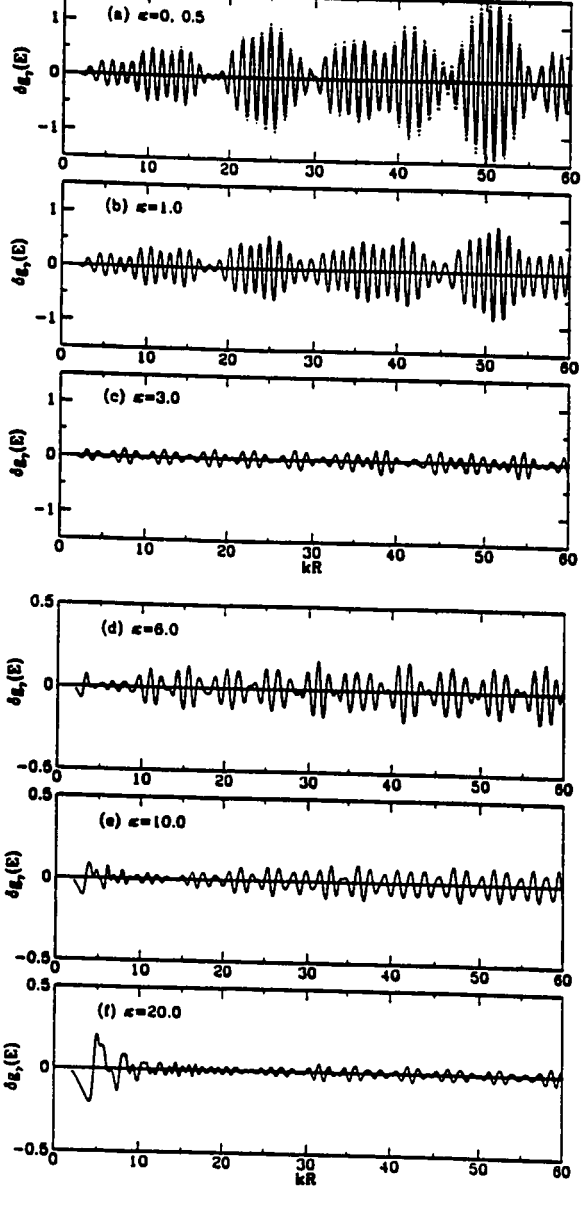


FIG. 1. The quantum-mechanical $\delta g_\gamma(E)$ with a Gaussian smoothing of width $\gamma=0.4\sqrt{E}$ as a function of $kR=\sqrt{E}$: (a) $\kappa=0$ (dotted line) and $\kappa=0.5$ (solid line), (b) $\kappa=1$, (c) $\kappa=3$, (d) $\kappa=6$, (e) $\kappa=10$, and (f) $\kappa=20$.

Let us first see how $\delta g(E)$ changes with values of $\kappa$ that correspond to experimentally available field strengths. In Fig. 1(a), the quantum mechanical $\delta g(E)$ for $\kappa=0.5$ is plotted by a solid line, along with that for zero field shown by a dotted line. $\kappa=0.5$ corresponds to $B\simeq 32$ T for a number of $N=3000$ electrons, if we use the semiempirical formula[7] for the cluster radius $R=2.25N^{1/3}$ Å, which for $N=3000$ yields $R\simeq 32$ Å. It can be seen that, surprisingly, $\delta g$ changes little even for this large field strength. Although the amplitudes are somewhat reduced, the supershell structure is the same as for $B=0$. There is also hardly any perceivable change in the energy shell corrections, which have basically the same beating supershell structure. This result seems to be quite different from that for the hydrogen atom in a uniform magnetic field.

In order to understand this, let us first make a rough estimate of magnitudes of the various terms in the Hamiltonian (2). The kinetic energy in this system is of the order of 1 eV, with a Fermi energy around 3 eV. The Zeeman term, $m\hbar\omega_L=m\mu_B B$, where $\mu_B$ is the Bohr magneton and $m$ the azimuthal quantum number as defined above, reduces to $5.8\times 10^{-5}mB$ eV. For $B\simeq 30$ T, this term is of the order of $10^{-3}-10^{-2}$ eV. The third term in Eq. (2) reads as $\sim 10^{-4}$ eV for $N=3000$. Hence the perturbations, and especially the $B^2$ term, are quite small compared to the kinetic energy. This latter term, however, plays a crucial role in the diamagnetic problem of the hydrogen atom,[11] leading already to the appearance of chaotic behavior as well as Landau levels near threshold for $B\simeq 6$ T.

We would like to understand the difference between these two systems: why is the effect of a magnetic field so small for metal clusters even for such a strong field? For that we look at the energy-scaled Hamiltonian, which can be written for both systems as

$$\hat{H}=\hat{H}_0+\kappa m+\tfrac{1}{4}\kappa^2\rho^2, \tag{5}$$

where $\hat{H}_0$ is the dimensionless Hamiltonian for zero field and $\rho^2=\bar{x}^2+\bar{y}^2$, with $\bar{x}$ and $\bar{y}$ measured by a proper length scale of the system. Here we have taken the length scale $R$ for the metal clusters, and the Bohr radius $a_0$ for the hydrogen atom. The energy scales are $E_0=\hbar^2/2m_eR^2$ (as stated above) and $\hbar^2/2m_ea_0^2$, respectively, for the two systems; $\kappa$ for the hydrogen atom is defined as $(a_0/l_0)^2$. Now we can see the difference of the two systems through Eq. (5), in the spirit of first-order perturbation theory. The eigenvalue of $\hat{H}_0$ for the hydrogen atom is given by $-1/n^2$ with $n=1,2,\ldots$ (spins neglected), which goes to zero as $n$ increases. It is the states with large $n$, the so-called Rydberg states, that are important for the irregular behavior in a magnetic field. For those states, the mean radii are many multiples of $a_0$, so that even for small $\kappa$ the magnetic length $l_0$ can become comparable, and hence the electronic motion can be greatly disturbed by the field. This also means that the third term in the Hamiltonian (5) can become the most dominant.

In the case of the spherical cavity, however, the situation is quite different. The unperturbed (kinetic) energy $k_{n,l}^2$ grows as $\sim n^2\pi^2$, becoming more and more dominant at higher energies. The Zeeman splittings can be large enough to cause level crossings for not too large $\kappa$. On the other hand, the mean radii of the electronic states are never larger than the cavity radius $R$ (i.e., $\rho$ is always smaller than unity), and one needs a rather large $\kappa$ for the third term in Eq. (5) to have a significant influence, i.e., for $l_0$ to be comparable to the range of the electronic motion.

It is thus the difference in the spatial extension of the electronic orbits that explains the different behavior of the two systems: although single atoms appear to be much smaller than large metal clusters, the large mean radii of their highly excited Rydberg states become comparable to the magnetic length $l_0$ for much smaller field strengths than possible for the valence electrons in metal clusters even of a size of 30 Å or more.

It is still interesting to see what happens in our system with larger values of $\kappa$, even though these correspond to

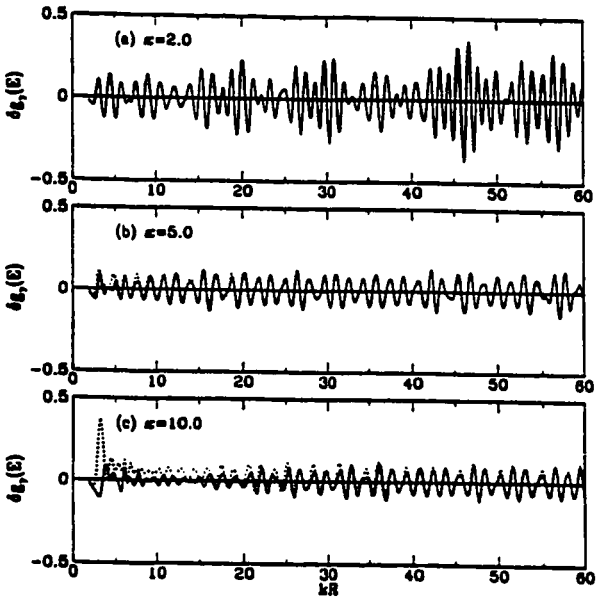


FIG. 2. Comparison of the quantum $\delta g_\gamma(E)$ obtained with exact eigenvalues (solid lines) and with the eigenvalues of the "cranking Hamiltonian" Eq. (6) in which only the Zeeman term is included (dotted lines), for (a) $\kappa=2$, (b) $\kappa=5$, and (c) $\kappa=10$. ($\gamma$ is the same as in Fig. 1.)

magnetic fields that are too high to be realized for currently available cluster sizes in which the electronic shell structure can still be observed.[1] As $\kappa$ increases, we see interesting changes in the supershell structure: the supershells get destroyed and new beat structures come about.

Figure 1(b) shows $\delta g$ for $\kappa=1$, in which we can see a substantial decrease in amplitudes and some changes in the structure, such as the third and fourth supershells merging into one. At $\kappa$ around 1.5 the original beating pattern has disappeared, and at $\kappa\simeq 2$ we have a different beat structure, though with much reduced amplitudes. These new beats are gone again at $\kappa=2.5$ and we have yet another regular beating pattern, which is shown in Fig. 1(c) for $\kappa=3$.

Interestingly, as we increase $\kappa$ even further, we keep having this phenomenon that one beat pattern appears after another, whereas the overall amplitudes keep decreasing. The beats shown in Fig. 1(c) are gone at $\kappa=5$, and the next ones coming at $\kappa=6$ are shown in Fig. 1(d). (Note the increased scale of the vertical axis for this figure as well as all the following figures of $\delta g$.) In Fig. 1(e) we see that there are almost no beats for $\kappa=10$, and again another regular pattern with much smaller amplitudes is seen in Fig. 1(f) for $\kappa=20$. For $\kappa\gtrsim 10$, we can also see how a Landau-like level structure starts to appear for lower energies.

We should note that up to $\kappa\lesssim 5$, the effect of the $\kappa^2$ term in the Hamiltonian (5) is negligibly small over the whole energy range and that we obtain roughly the same results also when neglecting this term in the Hamiltonian. In Fig. 2 we compare $\delta g(E)$ for $\kappa=2$, 5, and 10 obtained with the exact eigenvalues of the full Hamiltonian (solid lines) to that obtained with only the Zeeman term included (dotted lines). The two curves are indistinguishable for $\kappa=2$, whereas they start deviating for lower energies at $\kappa=5$ and differ largely and over a much larger energy range for $\kappa=10$.

We can thus conclude that for $\kappa\lesssim 5$, the gradual changes in the shell structure and the series of varying beat patterns are caused essentially by the rearrangement caused by the Zeeman splittings. That is, the approximate Hamiltonian that governs the system and gives all the essential results is given by

$$\hat{H}\simeq\hat{H}_{\rm rot}=\frac{1}{2m_e}\mathbf{p}^2+V(r)+\omega_L L_z. \tag{6}$$

This describes the original system in a frame rotating about the $z$ axis with a frequency $-\omega_L$. From earlier work, we know that simply rotating a two-dimensional isotropic harmonic oscillator with the same frequency as the oscillator frequency does generate Landau levels, and that a series of new quantum gaps is formed as we further crank the system[12] with higher frequencies. The present results give another example of the formation of new shells at different values of the "cranking" frequency.

In order to see how the shell structure is reorganized as a function of $\kappa$, we plot in Fig. 3(a) the energy levels given by the cranking Hamiltonian (6) for $0<\kappa<7$ in the energy range $0<E<200$ (i.e., roughly the first supershell for $0<kR<14$), and the same in Fig. 3(b) for the range $450<E<650$ (i.e., for $21<kR<26$ as part of the second supershell). Although it is not possible to show an energy range covering several supershells in one plot, since the level scheme would be too crowded and the plot would become essentially black, the excerpts shown illustrate how lighter and blacker regions corresponding to higher and lower level densities, respectively, alternate as $\kappa$ is varied.

## III. SEMICLASSICAL ANALYSIS OF THE LEVEL DENSITY

We would now like to analyze our results from a semiclassical point of view. In the absence of a magnetic field, the system has a high degree of symmetry: the SO(3) rotational symmetry. Accordingly, the periodic orbits form families of highly degenerate orbits: each of the planar polygons is threefold degenerate, since it can be continuously rotated about three Euler angles without changing its length and thus its action. (The diameter orbit with $p=2t$ makes an exception: it has only a twofold degeneracy since rotation about its own direction does not lead to a new orbit. This is the reason that its contribution to the trace formula is of higher order in $\hbar$ and plays a negligible role for the shell structure.) Now, in the semiclassical calculation of the level density one has to sum over all closed periodic orbits of the classical system.[6,9] When the orbits occur in degenerate families, one has to integrate over the parameters that describe their degeneracies.[6,13,14] These parameters may, for the present SO(3) symmetry, be taken as the Euler angles and, more generally, as the group parameters that describe the particular continuous symmetry of the system.[14] This integration has implicitly been performed in the trace formula derived by Balian and Bloch, so that only a discrete sum over the distinct families of orbits is left in Eq. (1).

When the magnetic field is switched on, the spherical symmetry of the system is broken and a large fraction of the degenerate orbit families is destroyed. However, there re-

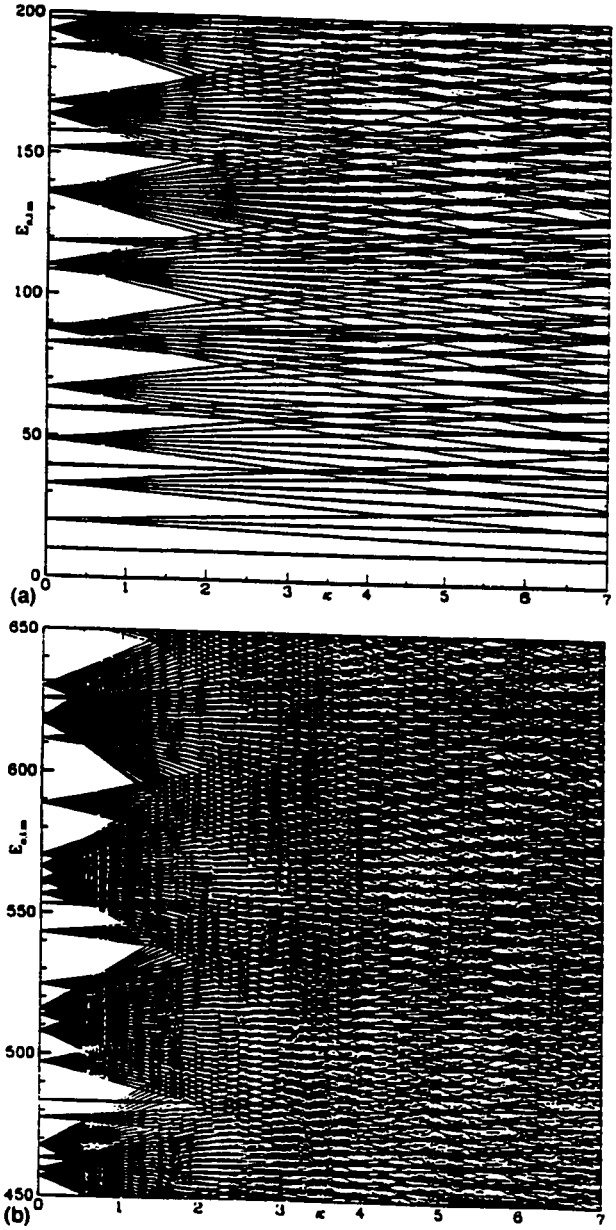


FIG. 3. Energy levels of the Hamiltonian (6) vs $\kappa$ in the energy range (a) $0<E<200$ and (b) $450<E<650$.

mains an axial U(1) symmetry and, correspondingly, all periodic orbits will have a one-dimensional degeneracy, which can be described by the rotational angle $\theta$ about the direction of the field. Most of the orbits that do not lie in the plane perpendicular to the magnetic field will be forced out of their plane of motion by the Lorentz force and turn into spirals. They will in general cease to be periodic: only some selected and rather complicated spiral orbits will become periodic after several reflections at the boundary. These will be rather long and thus give small contributions to the trace formula. The shortest orbits will be among those lying in the plane perpendicular to the magnetic field. These orbits are composed of portions of circular cyclotron orbits and have the same topology as those in the field-free system: they can thus be labeled by the same indices $p$ and $t$. To lowest order in the magnetic field, their actions will be changed by the magnetic flux through the surrounded unperturbed areas, which is most easily calculated from the vector potential of the external magnetic field.[15]

Thus, the structure of the classical dynamics is dramatically changed by the magnetic field, and this was the motivation of our present study. On the other hand, we have seen above that the quantum-mechanical level density does not undergo any sudden changes as the field is switched on and, in fact, it is very little affected for smaller $\kappa$, even up to a few tens of Tesla for realistic metal cluster sizes. The aim of the present section is therefore within the semiclassical framework to understand these smooth changes and, for the larger field strengths, the disappearance and recurrence of beating patterns described in the previous section.

In principle, it should pose no basic problem to rederive the trace formula in the presence of the magnetic field; the summation over periodic orbits here requires only one extra integration over the degeneracy parameter corresponding to the U(1) symmetry, i.e., the polar angle $\theta$ just mentioned. However, even if this were performed, a generic problem would still exist: the transition of the higher symmetry in the field-free case to the lower symmetry in the presence of the field cannot be done in a smooth way. Since each degree of degeneracy gives an extra power of $\hbar^{-1/2}$ in the amplitudes of the semiclassical trace formula,[13,14] these amplitudes change abruptly and in a nonanalytical way when the magnetic field is switched on. Inversely, if one starts from the semiclassical trace formula applicable to the axially symmetric case with magnetic field and lets the field strength tend to zero, the amplitudes will diverge: the semiclassical result of the case with lower symmetry simply does not hold in the limit of higher symmetry.

In order to overcome this difficulty, a "trace formula for broken symmetry" has recently been developed by one of us,[16] which is constructed precisely to bridge the transition from higher to lower symmetry in a smooth, nonsingular way. The formula has been derived in the framework of semiclassical perturbation theory and reads

$$\delta g(E)=-\frac{1}{\pi}\mathrm{Im}\left\{\sum_{\Gamma} \mathcal{A}_\Gamma(E) \times e^{i[S_\Gamma(E)/\hbar-\sigma_\Gamma\pi/2]}\mathcal{M}_\Gamma(\epsilon/\hbar,E)\right\}. \quad (7)$$

Here $S_\Gamma$ are the actions and $\sigma_\Gamma$ the Maslov indices, respectively, of the unperturbed periodic orbit families labeled by $\Gamma$. The only change with respect to the trace formula of the unperturbed system[14] is the appearance of a modulation factor $\mathcal{M}_\Gamma(\epsilon/\hbar,E)$ under the summation over the orbit families $\Gamma$. It is defined by

$$\mathcal{M}_\Gamma(\epsilon/\hbar,E)=\langle e^{i\Delta S_{\gamma_g}/\hbar}\rangle_{g\in G}=\int d\mu(g)e^{i\Delta S_{\gamma_g}(E)/\hbar}. \quad (8)$$

$\Delta S_{\gamma_g}(E)$ is the lowest-order change in the classical action of an individual orbit $\gamma_g$ within the family $\Gamma$ and is given by

$$\Delta S_{\gamma_g}(E)\sim-\epsilon\oint_{\gamma_g}\hat{H}_1 dt, \quad (9)$$

where the action integral is evaluated along the unperturbed periodic orbit $\gamma_g$, and $\epsilon$ is a small parameter characterizing the perturbation $\epsilon\hat{H}_1$ of the Hamiltonian that causes the symmetry breaking. The modulation factor (8) is defined as the average of the additional phase factor due to $\hat{H}_1$, averaged over the group elements $g$ that characterize the continuous symmetry of the unperturbed system. In the integral on the rhs of Eq. (8), $d\mu(g)$ is a suitably normalized group measure (usually called the "Haar measure") of the group $G$. For zero perturbation, i.e., for $\epsilon=0$, $\mathcal{M}_\Gamma$ becomes unity and Eq. (7) becomes identical with the original trace formula.[14]

In general Eq. (7) is expected to work as long as the argument of the modulation factor $\mathcal{M}_\Gamma$ is of the order of unity or smaller. For significantly larger perturbations, errors in the action become significant, but then the standard formulas adjusted for the reduced symmetry[9,14] are valid. There is an intermediate regime where the argument is moderately large in which both approaches give consistent results. Note that $\mathcal{M}_\Gamma$ in general depends on the energy $E$.

In our present case, we will start from the "cranking Hamiltonian" (6) in which the perturbation is the Zeeman term that contains the magnetic field $B$ in lowest order; the neglect of the diamagnetic terms proportional to $B^2$ in our original Hamiltonian (2) does not matter in this first-order perturbative treatment. The unperturbed SO(3) symmetry shall be characterized by the three Euler angles $(\alpha,\beta,\eta)$; they are chosen in such a way that $\beta$ is the angle between the plane of motion of a given orbit and the direction of the magnetic field (i.e., the $z$ axis). The change in action (9) of the orbit $\gamma_g$ then becomes

$$\Delta S_{\gamma_g} = -\omega_L \oint_{\gamma_g} L_z dt = -\frac{e}{c} B A_{\gamma_g}$$
$$= \mp \frac{e}{c} B R^2 \frac{p}{2} \sin(2\pi t/p)\cos\beta. \qquad (10)$$

Here $A_{\gamma_g}$ is the projection onto the $(x,y)$ plane of the area enclosed by the unperturbed periodic orbit $\gamma_g$, which here is labeled by the numbers $p$ and $t$ (see Sec. II), and we have used the classical relation $L_z = 2m_e dA_{\gamma_g}/dt$. The $\mp$ sign corresponds to the counterclockwise or clockwise orientation of the motion around the $z$ axis, respectively.

Note that $\Delta S_{\gamma_g} = -eBA_{\gamma_g}/c$ may also be obtained from the very definition of the action, $S_\Gamma = \oint_{\gamma_g} \mathbf{p}\cdot d\mathbf{q}$, using the fact that in the presence of the vector potential $\mathbf{A}$, the canonical momentum $\mathbf{p}$ equals $m_e\dot{\mathbf{q}} - e\mathbf{A}/c$ and by transforming the second part of the action integral using Stokes's theorem; $eBA_{\gamma_g}/\hbar c$ hereby is, of course, nothing but the magnetic flux through the unperturbed orbit in dimensionless units. It can also easily be shown that the changes in both the lengths and the areas $A_{\gamma_g}$ of the orbits — and in the amplitudes $\mathcal{A}_\Gamma(E)$, for that matter — brought about by their bending in the magnetic field are strictly of second and higher order in $B$ and thus can be safely ignored in a first-order treatment.

The definition of the modulation factor (8) then leads to

$$\mathcal{M}_{pt}(\kappa) = \frac{1}{8\pi^2}\int_0^{2\pi} d\alpha \int_0^{2\pi} d\eta \int_0^{\pi} \sin\beta e^{\mp iF(p,t;\kappa)\cos\beta} d\beta, \qquad (11)$$

with $F(p,t;\kappa) = \kappa(p/2)\sin(2\pi t/p)$. The integrals over $\alpha$ and $\eta$ are trivial, and that over $\beta$ reduces to an integral representation of the spherical Bessel function of order zero, $j_0(\mp F) = \sin F/F$, giving finally

$$\mathcal{M}_{pt}(\kappa) = j_0\left[\kappa\frac{p}{2}\sin(2\pi t/p)\right]. \qquad (12)$$

Note that $\mathcal{M}$ here is real and independent of the energy. It is worth pointing out that the two opposite directions of the motion about the field direction yield the same modulation factor, once their phase factors are averaged over the orbit family. Also note that the modulation factor for the diametrical orbits ($p=2t$), giving the second term in Eq. (1), is unity. This is no surprise since the unperturbed diametrical orbits enclose no area and hence no magnetic flux. An analogous result has been obtained by Ullmo, Richter, and Jalabert[17] in a calculation of susceptibilities of two-dimensional (2D) electron gases, there for rectangular and circular 2D billiards (though for the circular billiard there is no decay of amplitude because the circular symmetry is not broken by the magnetic field).

We arrive thus at the following perturbative trace formula for the spherical cavity in a magnetic field, correct to first order in $B$:

$$\delta g(E,B) = \sqrt{\frac{kR}{\pi}}\sum_{t=1}^{\infty}\sum_{p=2t+1}^{p_m}(-1)^t \sin 2\phi_{pt}\sqrt{\frac{\sin\phi_{pt}}{p}}\sin\left(\frac{S_{pt}}{\hbar} - 3p\frac{\pi}{2} + \frac{3\pi}{4}\right) j_0\left(p\frac{eBR^2}{2\hbar c}\sin 2\phi_{pt}\right)$$
$$-\sum_{t=1}^{\infty}\frac{1}{2\pi t}\sin\left(\frac{S_{2t,t}}{\hbar}\right), \quad \phi_{pt} = \pi\frac{t}{p}. \qquad (13)$$

Note that the summation over the number $p$, which is proportional to the repetition number of the primitive periodic orbits, must be limited here to an upper value $p_m$, because the argument of the modulation factor $j_0$ is proportional to $p$ itself. (This is natural as this argument contains the change in the total action of the repeated periodic orbit.) Since the argument of the modulation factor is supposed to be smaller than unity (or, at least, not much bigger), we cannot sum over arbitrarily long orbits. In practice this does not matter as long as one is interested only in the gross-shell effects of the level density and includes a Gaussian averaging that automatically suppresses the contributions from long orbits.

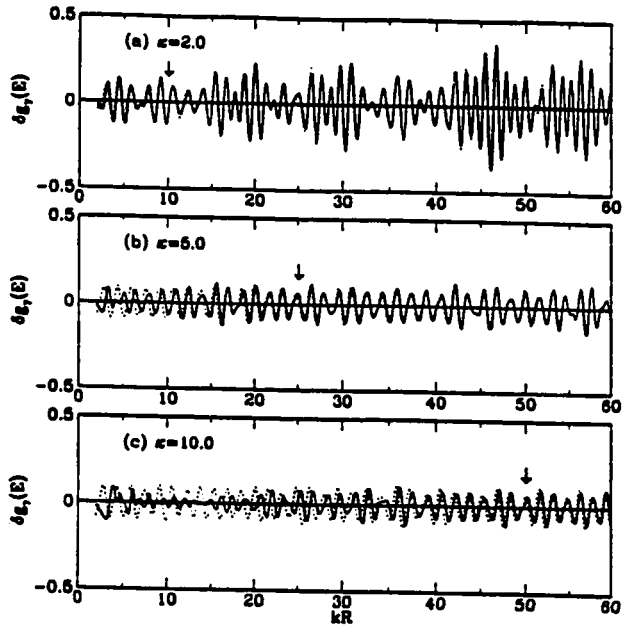


FIG. 4. Comparison of exact quantum $\delta g_\gamma(E)$ (solid lines) and semiclassical $\delta g_\gamma(E)$ (dotted lines) for (a) $\kappa=2$, (b) $\kappa=5$, and (c) $\kappa=10$. ($\gamma$ as in Fig. 1.)

We shall now investigate to what extent our quantum results for the level density $\delta g(E)$ can be reproduced and thus be interpreted semiclassically by the new trace formula. In Fig. 4, we compare the exact quantum-mechanical $\delta g(E)$ (solid lines) with the semiclassical results (dotted lines) for $\kappa=2$, 5, and 10. (The same Gaussian average as before was applied in both cases.) We see that Eq. (13) yields an excellent agreement with the quantum results up to $\kappa=2$. The largest deviations occur at low energies, and the lower limit of the best agreement extends to higher energies as $\kappa$ increases. But even at $\kappa=5$, the trace formula (13) still works fairly well for $kR\gtrsim 20$.

The increasing disagreement with decreasing energy can be understood in terms of the new Landau orbits that are created in the magnetic field but cannot be reproduced by the perturbative trace formula. Even for small $\kappa$, there is always a lower limit in energy for which cyclotron orbits exist that have a radius smaller than the cavity radius $R$: this happens simply because the cyclotron radius is proportional to the wavelength $k$ and thus to $E^{1/2}$. The perturbative approximation underlying Eq. (13) will always fail below this lower-energy limit. For small fields (e.g., in the case $\kappa=2$ in Fig. 4), this limit falls below the position of the lowest quantum state $\varepsilon_{10}$ of the unperturbed system and thus has no physical consequence. In stronger fields, however, the lower limit increases. The consequence is most dramatically seen in Fig. 4 for the case $\kappa=10$, where the quantum level density already starts building up the lowest Landau orbits. The missing Landau orbits in the perturbative trace formula thus explain its complete failure for $kR\lesssim 25$.

We may introduce a "confidence limit" as the value of $kR$ above which the cyclotron radius is larger than, say, five times the cavity radius $R$. This would, in the dimensionless units we are using, simply be the value $(kR)_0=5\kappa$. For energies higher than $(kR)_0^2$, the bending of the classical orbits in the magnetic field becomes negligible and thus the first-order treatment in $B$ is sufficient (cf. Refs. 15 and 18). This critical value $(kR)_0$ is indicated in Fig. 4 by a vertical arrow for each value of $\kappa$. Indeed, above these values, the agreement of the semiclassical with the quantum level density is very good in all cases. Even for somewhat smaller energies, the disagreement consists only in a phase shift of the oscillations, still giving a reasonable semiclassical reproduction of the gross-shell structure. Only when $kR$ is substantially smaller than $(kR)_0$ does the perturbative trace formula fail entirely.

For energies of the order of $(kR)_0^2$ or larger, we are now in a place to interpret the quantum results from Sec. II in terms of the semiclassical trace formula (13). For the shortest unperturbed orbits (e.g., the triangles and squares), $F\simeq\kappa$ and hence for $\kappa\lesssim 0.5$ we have $j_0(F)\simeq 1$. This explains the small changes in $\delta g(E)$ for the small values of $\kappa$. We understand that the spiral-type orbits are almost periodic around the unperturbed families and contribute to the trace almost as significantly as the truly periodic orbits. For larger $\kappa$, the semiclassical $\delta g(E)$ also reproduces well the changing beat structure up to $\kappa\lesssim 5$. In fact, up to these values of $\kappa$ we can see from Eq. (10) that $\Delta S\simeq\hbar\kappa\simeq\hbar$ is still a small perturbation on the semiclassical level, which breaks the periodicity of most of the orbits and yet does not prevent them from contributing to the trace. This is in contrast to the situation where the perturbation is so large, also on the semiclassical level, that it completely destroys the orbit families and only isolated orbits in the phase space exist, for which the original Gutzwiller trace formula[9] is applicable and should, in fact, be used (except for the cyclotron orbits with radii smaller than $R$, which again have a continuous degeneracy).

In order to relate the quantum-mechanical $\delta g(E)$ to the trace formula in a different way, we take its Fourier transform with respect to $kR$. When there is no field, the Fourier transform yields exactly a length spectrum of the responsible classical orbits, as we can see from Eq. (1); the signals of the Fourier power spectrum give simply the orbit lengths measured in units of $R$. In the presence of the magnetic field, however, we have to be careful. For a given magnetic field, orbits with different energies have different curvatures, the cyclotron radius being proportional to the velocity. This means that for a given $\kappa$, $\delta g(kR)$ as a continuous function of $k$ contains a whole set of orbits with different curvatures and length scales, more curved ones at lower energies and less curved ones at higher energies. Hence its Fourier transform in terms of $kR$ can, strictly speaking, not yield the correct length spectrum. Nevertheless, we may inspect the Fourier transforms of $\delta g(kR)$ for small enough $\kappa$, for which we can ignore the curvature of the orbits, and that is exactly the range for which the perturbative trace formula can be applied.

As $kR$ becomes larger, the orbits get less and less distorted by the magnetic field, approaching the unperturbed polygonal orbits asymptotically. The perturbative trace formula thus works better and better, while the perturbation in the actions (i.e., the magnetic flux enclosed) becomes relatively smaller and smaller, so that the actions asymptotically approach their unperturbed values (i.e., the mechanical momentum times the orbit length). In other words, the level density approaches that of the unperturbed system asymptoti-

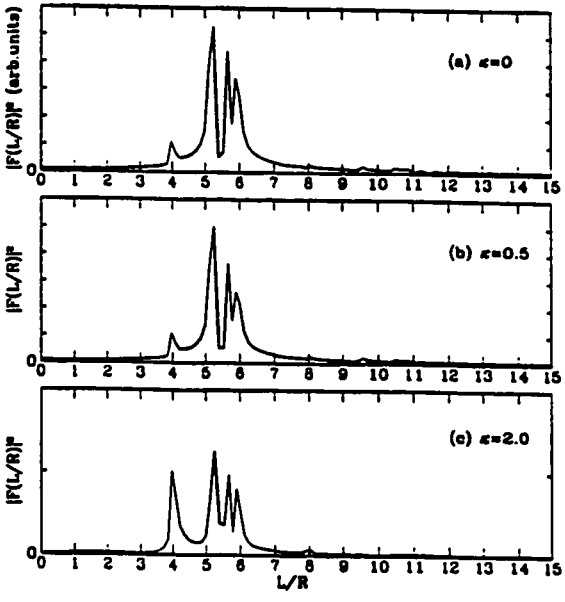


FIG. 5. Fourier transforms of the quantum $\delta g_\gamma(kR)$ as a function of the orbital length $L/R$ for (a) $\kappa=0$ [corresponding to $\delta g$ in Fig. 1(a), dotted line], (b) $\kappa=0.5$ [cf. solid line in Fig. 1(a)], and (c) $\kappa=2$ [cf. solid line in Fig. 2(a)].

cally for high energies, as we have also found it to occur quantum mechanically, in contrast to the case of the hydrogen atom in Sec. II. Therefore, in taking the Fourier transform of $\delta g(kR)$, we should restrict the range of $kR$ to not too high values if we want to see the effect of the magnetic field on the orbit lengths. If we sample too high energies, the Fourier spectrum will be dominated by the lengths of the unperturbed orbits of the field-free system.

We show in Fig. 5 the Fourier amplitudes of the quantum $\delta g(kR)$, obtained for the range $kR \lesssim 50$ for $\kappa \lesssim 2$. This range of $kR$ yields, in fact, enough resolution in the length spectrum to identify the most dominant short orbits. Figure 5(a) shows the amplitudes for the case of zero field [i.e., for the $\delta g$ shown in Fig. 1(a) with a dotted line]. We clearly see the signals of the triangular, square, pentagon, and hexagon orbits; the signals of all longer orbits are suppressed by the Gaussian averaging with the chosen value of $\gamma$. We can see that the triangles and squares give the most dominant contributions and the contribution from the diametrical orbit is, as explained earlier, quite small. For $\kappa=0.5$ the main peaks are slightly suppressed, but the dominance of the same two leading orbits and hence their interference is still retained as we could expect.

In Fig. 5(c) for $\kappa=2$, now, these two leading amplitudes are dramatically reduced and have values comparable to that of the diameter orbit. Up to this point, the perturbation has been effective only to first order in $B$, and since there is no first-order effect on the diameter orbit, its Fourier amplitude has hardly been affected [note the increased vertical scale in Fig. 5(c)]. Thus, from this value of $\kappa=2$ on, the higher degeneracy of the unperturbed orbits with $p>2t$ has been removed by the magnetic field and that henceforth, the simple and pronounced supershell beat pattern of just two leading orbits (triangles and squares) is replaced by a more complicated interference of at least four orbits with comparable amplitudes, including the shortest diameter orbit. Their detailed balance together with their increasing lengths in the stronger fields are responsible for the disappearance and recurrence of the beating pattern.

## IV. SUMMARY AND CONCLUSIONS

Quantum interferences play a fundamental role in physics and give rise to a wealth of interesting phenomena and observational tools. The beating pattern of the density of quantum states in a spherical cavity, theoretically instigated by Balian and Bloch over twenty years ago,[6] is just one example that has found its experimental realization in the recently observed supershell structure in the stability of large metal clusters.[3-5] At the same time, it constitutes a prime example for the semiclassical interpretation of a quantum phenomenon in terms of classical orbits.

Our objective was to study the effect of an external homogeneous magnetic field on this supershell pattern of the level density in a large metal cluster modeled by a spherical cavity. Whereas the classical periodic orbits are dramatically affected by the perturbation, since the breaking of the spherical symmetry destroys a large part of the degenerate orbit families, only small and relatively smooth changes of the quantum-mechanical level density take place for fields that are not too strong — the latter result being understood in terms of first-order perturbation theory, which leads to the familiar Zeeman splitting of the quantum levels. In fact, the supershell structure is retained up to the highest available magnetic field strengths for typical cluster sizes in which electronic shell effects can be observed presently. For still larger fields, the amplitude of the supershells is reduced and eventually the beat pattern vanishes and then reappears in different forms when the field strength is increased even further.

In order to assess the problem semiclassically, we have made use of a recently developed trace formula for broken symmetry,[16] in which the perturbing Hamiltonian responsible for the symmetry breaking is treated only to lowest order. We have derived the explicit analytical first-order trace formula for the cavity in a magnetic field and found that it reproduces the quantum level density very well in those very situations where the first-order perturbation theory also works well quantum mechanically. We have hereby given another example for the usefulness of the new trace formula (7), which is able to handle the transition of higher to lower symmetry without the typical singularities that have hampered the semiclassical periodic orbit theory for quite some time.

It is worth repeating that in general, as indicated in Eqs. (9) and (8), the action shift due to a symmetry breaking perturbation and hence also the modulation factor $\mathcal{M}$ in the trace formula (7) depends on the energy, typically in a monotonously increasing way.[16] In the present system, $\mathcal{M}$ in Eq. (12) is, however, energy independent. This explains why the perturbative trace formula here works for arbitrarily high energies — in fact, it works best in the high-energy limit where the perturbation of the classical orbits by the magnetic field becomes negligible and the exact spherical symmetry is restored. This situation is different from other forms of symmetry breaking, e.g., through a deformation of the system,

where the small parameter of the theory is multiplied by a positive power of the energy and the exact symmetry of the unperturbed Hamiltonian thus is restored in the zero-energy limit (see Refs. 16 and 18 for several examples). Conversely, in the low-energy limit of the present system, the cyclotron radius can become smaller than the cavity radius. This gives rise to a new class of degenerate orbits that build up the Landau levels and cannot be reproduced by the first-order perturbation theory. For weak fields ($\kappa \lesssim 2$), however, the lower-energy limit for which this happens falls below the position of the lowest-energy level and therefore it puts no practical restriction on the applicability of our perturbative trace formula (13).

For fields that are not too strong we have also been able to show, through Fourier transforms of the quantum level density, how the amplitudes of the most dominant short classical orbits are rearranged by the magnetic field, and this could give us a clue to the way in which the supershell beat structure is modified by the field. For stronger fields where the first-order perturbation no longer works, the Fourier transform with respect to the mechanical momentum $k$ loses its meaning, because the length scale of the system itself depends on the energy. It is well known (see, e.g., Ref. 11) that in such cases, the study of the classical dynamics still may be simplified by the scaling of coordinates, momenta, and energy by suitable powers of the external magnetic field strength. Specifically in our present notation, the transformations $\mathbf{r} \rightarrow \kappa^{2/3}\mathbf{r}$ and $\mathbf{p} \rightarrow \kappa^{-1/3}\mathbf{p}$ will yield a scaled Hamiltonian $\kappa^{-2/3}\hat{H}$ that no longer depends explicitly on $\kappa$. It is then sufficient to solve the classical equations of motion as a function of one scaled energy parameter $\xi = \kappa^{-2/3}E$ only, instead of the two parameters $\kappa$ and $E$ explicitly. As the scaled action is then given by $\kappa^{1/3}S$, it is possible to take Fourier transforms of the level density with respect to the variable $\kappa^{-1/3}$, with a fixed scaled energy $\xi$ and thus with a fixed (scaled) cyclotron radius, yielding again unique Fourier peaks that exhibit the scaled actions of the leading classical periodic orbits. This procedure has been used successfully in the study of atoms in strong magnetic fields,[11] which provides an application of the periodic orbit theory to chaotic systems. As we have discussed in Sec. II, however, the present system does not give us access to a similar situation, since the magnetic length is much larger than the typical extensions of the valence electrons in experimentally observable metal clusters for technically accessible field strengths.

We close this discussion by mentioning that in semiconductor heterostructures, so-called quantum dots can be manufactured that are a two-dimensional analog of metal clusters. These quantum dots can have sizes of tens of nanometers, which become comparable to the magnetic length in fields of the order of a few Tesla. Recently, rather regular oscillations of the conductance in a circular quantum dot as a function of the applied magnetic field strength have been observed and interpreted[15] in terms of classical orbits in a circular billiard, quite analogously to our present study.

## ACKNOWLEDGMENTS

We would like to thank Rajat K. Bhaduri for suggesting this problem and for valuable insights and discussions. We also thank M. V. N. Murthy for stimulating discussions. One of us (K.T.) appreciates the hospitality of the Physics Department of the University of Regensburg during her stay. This research was supported by a grant from the Natural Sciences and Engineering Research Council of Canada and by Grants No. SC1*CT92-0770 and No. CHRX-CT94-0612 of the Commission of the European Communities.

*Present address: Division de Physique Théorique, Institut de Physique Nucléaire, Université de Paris-Sud, F-91406 Orsay Cedex, France.

[1] W. A. de Heer, Rev. Mod. Phys. 65, 611 (1993).
[2] M. Brack, Rev. Mod. Phys. 65, 677 (1993).
[3] J. Pedersen *et al.*, Nature 353, 733 (1991).
[4] C. Bréchignac *et al.*, in *Physics and Chemistry of Finite Systems: From Clusters to Crystals*, edited by P. Jena *et al.* (Kluwer Academic Publishers, Dordrecht, 1992), Vol. I, p. 369.
[5] J. Lermé *et al.*, Phys. Rev. B 52, 2868 (1995), and earlier references quoted therein.
[6] R. Balian and C. Bloch, Ann. Phys. (N.Y.) 69, 76 (1972).
[7] H. Nishioka, Klavs Hansen, and B. R. Mottelson, Phys. Rev. B 42, 9377 (1990).
[8] O. Genzken and M. Brack, Phys. Rev. Lett. 67, 3286 (1991).
[9] M. C. Gutzwiller, J. Math. Phys. 12, 343 (1971).
[10] R. Balian and C. Bloch, Ann. Phys. (N.Y.) 60, 401 (1970).
[11] H. Friedrich and D. Wintgen, Phys. Rep. 183, 37 (1989), and references quoted therein.
[12] R. K. Bhaduri, S. Li, K. Tanaka, and J.C. Waddington, J. Phys. A 27, L553 (1994).
[13] V. M. Strutinsky and A. G. Magner, Fiz. Elem. Chastits At. Yadra 7, 356 (1976) [Sov. J. Part. Nucl. 7, 138 (1976)].
[14] S. C. Creagh and R. G. Littlejohn, Phys. Rev. A 44, 836 (1991); J. Phys. A 25, 1643 (1992).
[15] S. M. Reimann, M. Persson, P. E. Lindelof, and M. Brack, Z. Phys. B (to be published).
[16] S. C. Creagh, Ann. Phys. (N.Y.) (to be published).
[17] D. Ullmo, K. Richter, and R. A. Jalabert, Phys. Rev. Lett. 74, 383 (1995).
[18] M. Brack, S. C. Creagh, P. Meier, S. M. Reimann, and M. Seidl in *Large Clusters of Atoms and Molecules*, edited by T. P. Martin (Kluwer, Dordrecht, 1996), p. 1; P. Meier *et al.* (unpublished).

## 3.3 Comments

In Fig.3.3 we show the shell correction $\delta E = E_{tot} - \tilde{E}_{tot}$ (for zero temperature) for $B = 30$ T. We have included only the linear Zeeman terms in the Hamiltonian, which is a good approximation even with this strong field. Comparing with Fig.3.2, we see only slight changes in the shell oscillations and especially no perceptible change in the positions of the supershell nodes. This is contrary to our expectation which motivated this work, that the supershell structure, especially its node positions, must be sensitive to phase changes coming from perturbation in the classical action due to the magnetic field. In order to understand this, let us estimate the phase change for the leading triangular and square orbits to first order in the field.

When there is no field, from the Balian-Bloch formula, Eq.(1) in the article, one can see that the phase difference between the contributions from the $t = 1$ triangular ($p = 3$) and square ($p = 4$) orbits is $\Delta S/\hbar - (3-4)3\pi/2$, where $\Delta S = S_\Delta - S_2$, while the overall amplitudes are approximately the same. As the length of the orbit $(p,t)$ is given as $L_{pt} = 2pR\sin(\pi t/p)$, $\Delta S/\hbar = 2kR\,(3\sin(\pi/3) - 4\sin(\pi/4))$. At the Fermi energy, which is about 3 eV independent of the atomic number or the number of valence electrons, $N$, the wave number $k$ is about $0.88\mathring{A}^{-1}$, and we use the semiempirical formula for the cluster radius, $R = 2.25N^{1/3}\mathring{A}$. When the phase difference becomes $\pi$, the two contributions have a destructive interference and hence the supershell oscillation has a node there. This happens at $N^{1/3} \simeq 8.6$ and thus

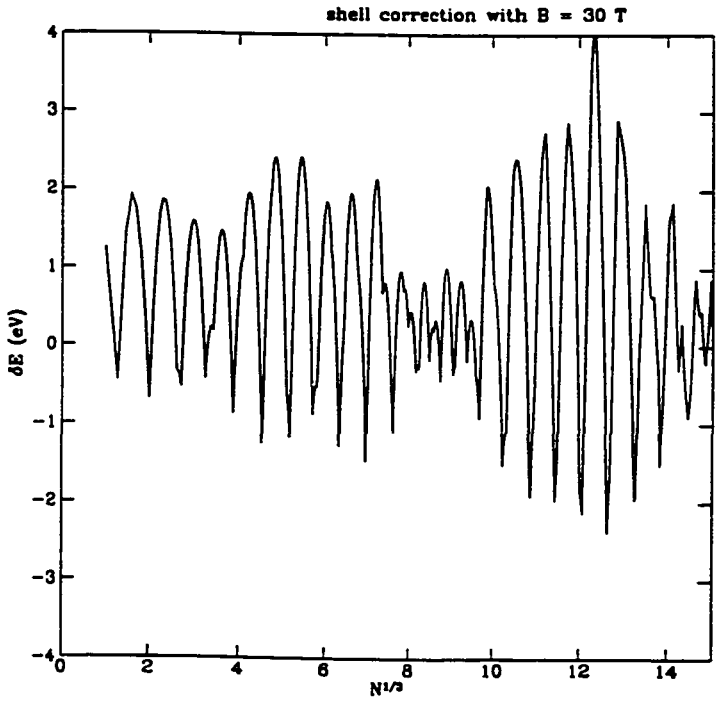


Figure 3.3: Shell correction $\delta E = E_{tot} - \tilde{E}_{tot}$ (zero temperature) for the metal clusters in a uniform magnetic field of $B = 30$ T.

$N \simeq 640$. Similarly, a constructive interference occurs at the phase difference $2\pi$, which turns out to be at $N^{1/3} \simeq 12$, i.e., $N$ around 1750. These agree well with the node and antinode positions in $\delta E$ in Fig.3.2 and also with the measured spectrum in Fig.3.1, considering the statistical uncertainties. The antinode position $N \simeq 1750$ seems to be slightly off from that seen in Fig.3.2, and this can be understood as due to longer orbits contributing more to the trace at higher energies.

Under a uniform magnetic field, each orbit acquires an extra phase that is to first order in the field, the magnetic flux enclosed by the original orbit measured in units

of $\hbar c/e$. Thus the extra phase difference between the contributions from the $t = 1$ triangular and square orbits are $\Delta\phi_B \equiv (eB/\hbar c)\,\Delta\mathcal{A}$. With $eB/\hbar c \simeq 1.5\,10^{-5}B/\mathring{A}^2$, this turns out to be $\Delta\phi_B = 5.29\,10^{-5}N^{2/3}B$. Taking $B = 30$ Tesla, this amounts to a phase increase in the supershell oscillation at the node around $N = 640$ of about $0.1/2 = 0.05$ (see Eq.(3.2)), and still about 0.1 near the antinode $N \simeq 1750$. We can now see that even with such a high magnetic field, perturbation in the supershell phase is so small that it hardly affects the overall structure. It is also seen in Fig.3.2 that the magic numbers, i.e., shell dips in $\delta E$, are especially robust against the perturbation. This is due to the fact that the perturbation, e.g., $(eB/\hbar c)\,\mathcal{A}_\Delta$ is even much smaller compared to the original action $k_F L_\Delta$, and hence it has little effect on the Bohr quantization condition, $kL = 2\pi n$.

As discussed in the article, one would need unrealistically high magnetic fields to see any substantial change in the shell and supershell structure of metal clusters. This is due to the fact that the electronic motion is confined within the cluster of radius $\sim 30\mathring{A}$ at the maximum, to which the magnetic length can be barely comparable with the field of 75 Tesla. The spherical symmetry of the system also results in such strong shell effects.

The electronic shell structure may be observed in yet larger clusters. However, as $N$ becomes larger, the observation will be more difficult due to competition between the effects of the size and temperature of clusters. As $N$ increases, the shell gaps decrease and may be more easily washed out by the finite temperature of the

cluster. On the other hand, if the clusters are cooled down too much, shell effects may be dominated by geometrical ion structure, in which magic numbers correspond to numbers of atoms for close-packing, and this seems to be more likely to occur in larger clusters. The mass spectra of sodium clusters have been measured with up to $N = 25000$, with clusters made in a different condition in a different cluster source from the one for the spectrum in Fig.3.1, and such a transition was observed [Martin 90a, Martin 90b]. It is not known exactly under what condition and how this transition occurs, and it is still an open question how large the clusters can be, in which electronic shell structure is observable.

We now proceed to study shell structure of quantum dots, which may be regarded as a two-dimensional analogue of metal clusters as the system of "free" electrons confined in a finite domain. It will be more interesting to study this system in the sense that electronic shell effects can be observed in quantum dots as large as microns and effects of magnetic fields can be readily seen.

# Chapter 4

# Magnetization and Magnetic Susceptibility of A Quantum Dot

## 4.1 Introduction

With recent advanced technologies it has become possible to make detailed studies of so-called "artificial atoms" or "quantum dots" [Kastner 93]. These are systems of two-dimensional electron gas confined in a finite region at the interface of semiconductor heterostructure, which is almost an ideal gas with high mobility at low temperatures. The size of a quantum dot can be controlled externally, as well as the number of confined electrons which can vary from one to about 5000. The observed bulk properties of a quantum dot are well described by a picture of independent electrons moving in an effective single-particle potential [Kastner 92, Chakraborty 92, Maksym 90], and

shell structure has been observed [Lindelof 96]. The lateral potential for confining electrons in a quantum dot is often well approximated by a two-dimensional harmonic oscillator [Kumar 90]. The electron-electron interaction, basically due to its repulsive nature, makes the mean-field potential shallower than the external one and flattens the bottom as the number of electrons increases. Thus the single-particle potential is effectively a harmonic oscillator for a quantum dot with small number of electrons, with a frequency smaller than the external one, and a potential with flat bottom and steeply rising walls with large number of electrons.

In this chapter, we study the magnetization and magnetic susceptibility of a quantum dot for the two limiting cases in the single-particle picture. Our aim is to compare the magnetization between the two limits, which reflects shell structure of the mean-field potential. We also interpret the quantum shell structure in terms of shortest classical orbits – particularly we examine the Aharonov-Bohm oscillations in the strong-field limit from this point of view.

Ashoori *et al.* [Ashoori 92, Ashoori 93], using single-electron capacitance spectroscopy, have measured the ground-state energies of a AlGaAs/GaAs quantum dot with 1-50 electrons in a uniform magnetic field perpendicular to the dot. The single-electron energy as a function of the magnetic field can be identified as the lowest Fock-Darwin level [Fock 28, Darwin 30], i.e., the ground state of a harmonic oscillator in a uniform magnetic field, with frequency $\hbar\omega = 5.4$ meV. The gross nature of the spectrum with larger number of electrons is consistent with $\hbar\omega \simeq 1$ meV. There have

been other experimental evidence for the Fock-Darwin levels [Hansen 89, Weis 93] in smaller quantum dots in a magnetic field, one of the latest observation with a InGaAs/GaAs dot by Rinaldi *et al.* [Rinaldi 96]. The shell structure has been observed in the conductance of a larger quantum dot of effective radius $R \simeq 0.4\,\mu$m with about 1700 electrons [Persson 95a, Persson 95b] and $R \simeq 0.3\,\mu$m with about 1000 electrons [Reimann 96b]. The conductance exhibits oscillations both as a function of the dot size and of a uniform magnetic field applied perpendicular to the dot. These oscillations can be explained in terms of a single-particle picture in a circular hard-wall or a "disc" potential [Persson 95b], and semiclassically through periodic orbits of an electron within the disc [Reimann 96b]. Reimann *et al.* have also found that a harmonic oscillator potential does not yield the right behaviour of these shell oscillations. Kumar, Laux and Stern [Kumar 90] have made a self-consistent Hartree analysis of the system of a quantum dot with a small number of electrons, and found that the single-particle energy levels are quite similar to the Fock-Darwin levels. Murthy, Shankar and Sinha [Murthy] have shown by a self-consistent Thomas-Fermi analysis that the mean-field potential flattens as the number of electrons increases and becomes "disc"-like with 1000 electrons.

The above mean-field picture seems to resemble that for nuclei [Mayer 49, Myers 66] and for simple metal clusters [de Heer 93, Brack 93]. Also in these systems, the mean-field potential is approximated by a harmonic oscillator for small number of fermions, and as the system becomes larger, by a potential with flat bottom and steeply rising

walls, e.g., Woods-Saxon potential. For these systems there is a semiempirical formula for the effective radius that is proportional to the cube root of the particle number. However, there is an important difference between these systems and the system of quantum dots : The confining potential for a quantum dot, which determines the effective shape and size of the dot is externally adjustable. That is, even if the same number of electrons are confined in a circular dot, its size and effective single-particle potential may be different for different experiments using different devices. Hence, although once given an external potential, the mean-field picture can be constructed as above, there is no empirical formula for the effective radius or oscillator frequency of a quantum dot as a function of the number of confined electrons. Accordingly we do not know what the mean-field potential is like simply for a given number of electrons, e.g., if it is like either a harmonic oscillator or a hard-wall potential.

We study the magnetization and magnetic susceptibility of a quantum dot with the single-particle picture. We examine the two limiting cases of effective one-body potential, the harmonic oscillator and the disc potential. As we are interested in the quantum shell effect, we consider the case of zero temperature. The purpose of this study is that by looking at the magnetic properties, in which different mean-field potentials will be reflected in different ways, one will be able to tell what kind of mean-field potential the system has. This is possible as magnetic properties are robust in the following sense. Once a uniform magnetic field $\mathbf{B}$ is applied to the system, a

length scale is set by the field, i.e., the magnetic length $l_0 = \sqrt{\frac{\hbar}{m_e\omega_c}} = \sqrt{\frac{\hbar c}{eB}} \simeq \frac{26}{\sqrt{B}}$nm. Classically this corresponds to the cyclotron radius $R_c = m_e vc/eB$, where $m_e$ is the electron mass and $v$ is the velocity. On the other hand, the system has its own length scale set by the mean field. However, the properties of a quantum dot will depend on only one parameter, the ratio of these two length scales that exist under a uniform magnetic field. Thus in order to study magnetic properties, we do not have to assume a size of the quantum dot nor vary the two physical parameters, the field strength and the size of the system, separately.

The response functions are also robust in the sense that, for example, the magnetization is determined by the derivative of the total energy of the system against the magnetic field, and not the total energy itself. For every electron added to a quantum dot, the total energy of the system increases by a constant amount, which corresponds to the classical charging energy, i.e., the electrostatic Hartree energy of the Coulomb interaction between electrons [Kumar 90, McEuen 93]. The total energy itself includes the effect of the inter-electron interaction and cannot be reproduced only by the effective single-electron picture. The magnetization and susceptibility, however, depend only on the derivatives of the total energy and may be directly connected to the single-particle density of states.

Sivan and Imry [Sivan 88] have studied the effect of finite size on the de Haas-van Alphen (dHvA) oscillations in a quantum dot in the quantum-Hall-effect regime. As-

suming a sharp boundary for confining electrons as in a disc, they estimated the contribution of so-called edge states to the magnetization and found the Aharonov-Bohm (AB)-type oscillations [Bogachek 72] due to these states. Meir, Entin-Wohlman and Gefen [Meir 90] have examined the dHvA and AB effects with harmonic confinement, using the grand partition function in the limit of zero temperature. In the present work, we reexamine the magnetization of a quantum dot with harmonic and disc confinement by explicit quantum-mechanical calculations, including the strong-field limit as considered in the above two works. There are two objectives in our study. One is to have a direct comparison of the magnetization between the two limits of the mean-field potential – we will thus have an indicator of the mean field, without explicitly referring to the effective size of the dot or the field strength as discussed above. The other is to understand the quantum shell structure semiclassically in connection with short periodic orbits of the electrons.

The connection between quantum shells and classical orbits is particularly interesting in the system of a quantum dot under the influence of an external magnetic field. As the size of a quantum dot may be as large as the order of microns, even with a magnetic field of the order of milli-Tesla, the magnetic length can become comparable to the size of the quantum dot and the effect of the magnetic field can be dramatic. This is in contrast with the system of simple metal clusters, whose size can only go up to about $30\mathring{A}$ and there is no perceptible change in its supershell structure with experimentally available field strenghts, as we saw in the last chapter. In the

system of a quantum dot, with realistic strengths of the magnetic field, we can see drastic changes in the electronic shell structure and classically in the orbit structure, all the way up to the formation of cyclotron orbits.

We first examine the case with harmonic confinement in Sec.4.2 and the circular hard-wall confinement in Sec.4.3. In Sec.4.2.1, we look at the quantum energy levels and magnetization, and in 4.2.2, classical orbits and their connection to shell structure in the magnetization. We discuss semiclassical values of the magnetization in 4.2.3 and effect of spins in 4.2.4. We make analogous studies for disc confinement in Sec.4.3.1 and B, respectively. Finally, in Sec.4.3.3 we study shell structure and classical orbits in the weak-field limit, in comparison with the system in a spherical cavity. We summarise and discuss the results in Sec.4.4.

### 4.1.1 Magnetization and Susceptibility

We consider the two-dimensional motion of a single electron in the effective confining potential $V(r)$ and in an external uniform magnetic field $\mathbf{B} = B\hat{\mathbf{z}}$.C Choosing the symmetric gauge $\mathbf{A} = \frac{1}{2}\mathbf{B} \times \mathbf{r}$ for the magnetic field, the single-particle Hamiltonian is written as

$$\hat{H} = \frac{1}{2m_e^*}\,\mathbf{p}^2 + \omega_L\, L_z + \frac{1}{2}m_e^*\,{\omega_L}^2\, r^2 + V(r)\,, \tag{4.1}$$

where $r^2 = x^2 + y^2$, $m_e^*$ is the effective mass of an electron and is $0.067m_e$ in GaAs, and $\omega_L = eB/2m_e^*c$ is the Larmor frequency ($e > 0$). To begin with, spins have not

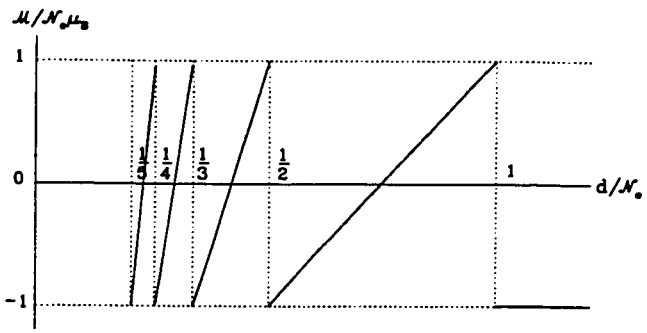


Figure 4.1: De Haas-van Alphen oscillations in the magnetization. The $\mathcal{M}$ is measured in units of $\mathcal{N}_e\mu_B$ and plotted as a function of $d/\mathcal{N}_e = \frac{eB}{hc}\frac{\mathcal{A}}{\mathcal{N}_e}$.

been included. We are going to examine two types of effective confining potentials, the isotropic harmonic-oscillator ($\mathcal{N}_e \lesssim 100$) and the circular hard-wall potential ($\mathcal{N}_e \gtrsim 1000$). The latter of which is the two-dimensional version of the system we have examined in the previous chapter.

We calculate the magnetization and susceptibility of a quantum dot for zero temperature :

$$\mathcal{M} = -\frac{\partial E_{tot}}{\partial B} \quad ; \quad \chi = \frac{\partial \mathcal{M}}{\partial B} = -\frac{\partial^2 E_{tot}}{\partial B^2} \,, \tag{4.2}$$

where $E_{tot}$ is the total energy of the system for a given number of electrons $\mathcal{N}_e$.

The low-temperature magnetization of an electron gas in the Landau levels exhibits the de Haas-van Alphen (dHvA) oscillations as the magnetic field strength is changed. At low temperatures, the electrons tend to occupy the lowest available

states in the Landau levels, Eq.(2.14) in Chapter 2. For a fixed $\mathcal{N}_e$, as $B$ is increased, the degeneracy of each Landau level $d \equiv \frac{eB}{hc}\mathcal{A}$ increases and can accommodate more electrons, where $\mathcal{A}$ is the area of the system. Hence some electrons jump down to lower states, which results in the oscillations in $\mathcal{M}$ as a function of $B$, between $-\mathcal{N}_e\mu_B$ and $\mathcal{N}_e\mu_B$. This is illustrated in Fig.4.1 as a function of $d/\mathcal{N}_e$.

## 4.2 Harmonic Confinement

### 4.2.1 Quantum energy levels and magnetization

We first examine the case with the harmonic-oscillator effective confinement, that is, $V(r) = \frac{1}{2}m_e^*\omega^2 r^2$ in Eq. (4.1). This is suitable for quantum dots with small number of electrons, e.g., for $\mathcal{N}_e \lesssim 100$ [Murthy, Ashoori 93]. It is advantageous to study this model first, as the problem is analytically solvable, before studying the case with disc confinement for which all the calculations will be numerical.

The Hamiltonian (4.1) in this case may be regarded as that of the system of a two-dimensional harmonic oscillator with frequency $\Omega = \sqrt{\omega^2 + \omega_L{}^2}$ in a frame rotating clockwise about the $z$ axis with frequency $\omega_L$. Thus the quantum energy eigenvalues are immediately written down as [Fock 28]

$$E_{n_r,l} = \hbar\sqrt{\omega^2 + \omega_L{}^2}\,(2n_r + |l| + 1) + \hbar\omega_L l\,, \tag{4.3}$$

where $n_r = 0, 1, 2, \ldots$ is the number of nodes, and the angular momentum $L_z = l\hbar$ with

$l = 0, \pm 1, \pm 2, ....$ Like the cranked oscillator in Chapter 2, this spectrum is identical to that of a two-dimensional anisotropic harmonic oscillator with frequencies $\omega_+$ and $\omega_-$ defined as

$$\omega_\pm = \sqrt{\omega^2 + {\omega_L}^2} \pm \omega_L \,. \tag{4.4}$$

As we saw in Chapter 2, a series of quantum gaps are formed as a function of the magnetic field, whenever the ratio of these two frequencies are rational. As we have discussed in Sec.4.1, in studying magnetic properties, we do not have to know *ab initio* the value of the mean-field $\omega$. If we scale the single-particle energy (4.3) by the natural energy unit $\hbar\omega$, it can be written in terms of one parameter, $b \equiv \omega_L/\omega$. This may be also written as the ratio of the two length scales, $b = \frac{1}{2}(a_0/l_0)^2 = \frac{1}{2}a_0^2 eB/\hbar c$, where $a_0 = \sqrt{\frac{\hbar}{m_e^* \omega}}$. Thus once given a field strength $B$, $b$ can be converted to a value of $\omega$, or vice versa : Taking a typical value of $\hbar\omega \sim 1$ meV for a small quantum dot [Ashoori 93] and the maximum possible value of $B \sim 10$ Tesla, the maximum realistic value of $b$ is of the order of 10. In Fig.4.2, we show the quantum energy levels as a function of $b$. The dotted lines are the Landau levels, which can be obtained by setting $\omega = 0$ in the energy levels (4.3). For small $b$ ($\lesssim 1$) the sequence of quantum gaps looks exactly the same as that of the cranked oscillator (see Fig.2.4 in Chapter 2) : In this region, $b^2$ is negligible and the effect of the field is the same as cranking. We can see that the largest gaps are formed at the primitive ratios of $\omega_-/\omega_+$ such as $1/2, 1/3, 1/4, ...$ and the next largest ones at $2/3, 3/4, 4/5, ...$, and so on.

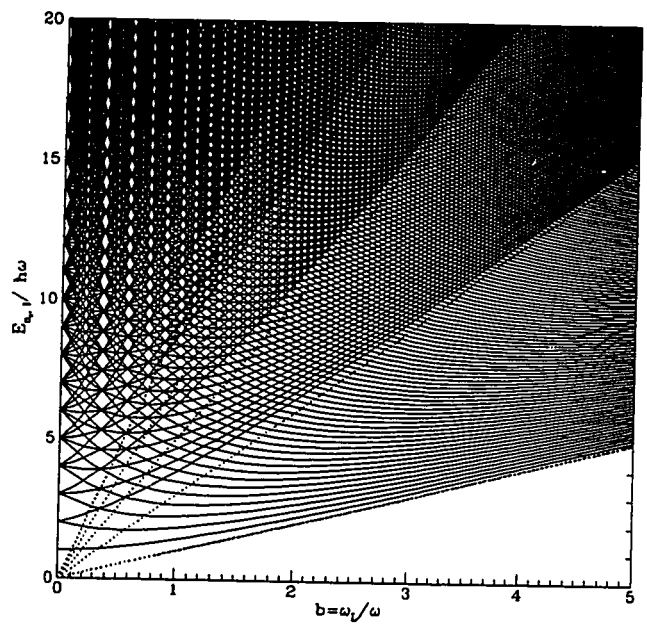


Figure 4.2: Energy levels for the harmonic confinement, Eq.(4.3), in units of $\hbar\omega$ as a function of $b = \omega_L/\omega$. The dotted lines are the Landau levels, with $\omega \equiv 0$ in Eq.(4.3). At larger $b$, the formation of the "Landau sheets" are clearly seen.

In the limit of $b \to \infty$, we have $\omega_- \to 0$ and $\omega_+ \to 2\omega_L = \omega_c$, where $\omega_c$ is the cyclotron frequency. That is, the system approaches the Landau-level limit. Here the Landau levels are energy levels of a one-dimensional oscillator of frequency $\omega_c$, each level having a degeneracy coming from an extra dimension, which will be infinite if the system has no boundary. It is seen in Fig.4.2 that as $b$ increases, the energy levels start converging towards the Landau levels. However, unlike the case with $\omega \equiv 0$, where the "cranking" frequency $\omega_L$ equals to the frequency $\Omega$, the levels do not collapse to the Landau levels completely. Instead of forming discrete, infinitely-degenerate levels, they form separate "sheets" of levels, each of which has infinite number of levels lying on it almost continuously, and corresponds to a Landau level with the same set of quantum numbers yielding the same value of $n_L \equiv n_r + \frac{l+|l|}{2}$ [Chakraborty 92, Meir 90]. Let us call them "Landau sheets". This is because the "cranking" frequency $\omega_L$ never becomes exactly equal to the frequency $\Omega$, or $\omega_-$ never becomes exactly zero. Physically it means that the particle will always feel the oscillator potential of $\omega_-$, no matter how shallow it becomes. In Fig.4.2 at larger value of $b$ we can see the distinct Landau sheets clearly, piling on one on top of another.

Calculating the magnetization $\mathcal{M}$ is straightforward, as the energy levels (4.3) are explicit functions of the magnetic field, and $\mathcal{M}$ is given by the sum of the $B$-derivatives of the single-particle levels for the occupied (for zero temperature, the

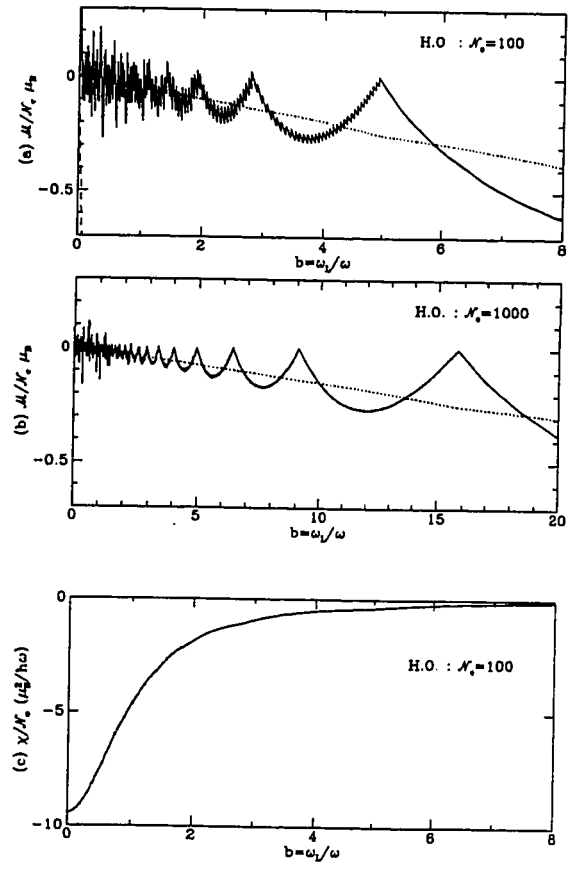


Figure 4.3: Magnetization for the harmonic confinement, Eq.(4.5), in units of $\mathcal{N}_e\mu_B$ as a function of $b$ for (a) $\mathcal{N}_e = 100$ and (b) $\mathcal{N}_e = 1000$. The dotted and dashed lines are the "semiclassical" values of the magnetization in the strong-field and strong-confinement limits respectively, as discussed in Sec.4.2.3. (c) Susceptibility in units of $\mathcal{N}_e\mu_B^2/\hbar\omega$ as a function of $b$ for $\mathcal{N}_e = 100$.

lowest) $\mathcal{N}_e$ levels. That is,

$$\mathcal{M} = -\mu_B \sum_{n_r,l}^{\leq E_F} \left(\frac{\omega_L}{\Omega}(2n_r + |l| + 1) + l\right), \tag{4.5}$$

where $\mu_B = e\hbar/2m_e^*c$ is the Bohr magneton and $\frac{\partial \hbar\omega_L}{\partial B} = \mu_B$. Accordingly the susceptibility is obtained by summing the second derivatives. We plot in Fig.4.3(a) $\mathcal{M}(b)$ in units of $\mathcal{N}_e\mu_B$ for $\mathcal{N}_e = 100$. The dotted and dashed lines are the "semiclassical" values for the magnetization which we will discuss later. The susceptibility for $\mathcal{N}_e = 100$ is shown in Fig.4.3(c), in which shell structure is barely seen.

In Fig.4.3(a) we see interesting features of $\mathcal{M}$, reflecting a series of shell gaps as a function of $b$. For small $b$ ($\lesssim 2$ for $\mathcal{N}_e = 100$) it has rapidly changing beats or "supershells", and as $b$ becomes larger, the dHvA-type oscillation sets in with rather regular, small shell oscillations superimposed on it. Eventually beyond the last peak in the dHvA oscillation, there is no more shell oscillation and $\mathcal{M}$ smoothly and slowly decreases towards $-\mathcal{N}_e\mu_B$. This is the situation where all the occupied levels are only on the Landau sheet that corresponds to the lowest Landau level. These features are common with any number of particles, except that the smaller $\mathcal{N}_e$ is, i.e., the smaller the Fermi energy is, the dHvA effect appears at smaller $b$. We show $\mathcal{M}(b)$ for $N_e = 1000$ in Fig.4.3(b) to demonstrate this, though harmonic confinement is not a proper approximation as the single-particle potential for this large number of electrons. In this figure we can see basically the same structure of $\mathcal{M}$ as for $\mathcal{N}_e = 100$, except that the tiny oscillations superimposed on the dHvA oscillations can hardly

be seen in the given scale. In this case, the peak at $b \simeq 16$ is the last dHvA peak, beyond which all the particles are on the lowest Landau sheet.

The level structure forming the Landau sheets in the strong-field limit results in some quantitative difference in the dHvA oscillations from those of the usual Landau levels. In the case of the Landau levels, $\mathcal{M}$ has a sawtooth shape, oscillating between $+\mathcal{N}_e\mu_B$ and $-\mathcal{N}_e\mu_B$, as a function of the field. The latter value arises when the Landau levels are completely occupied up to the Fermi energy, e.g., when all the particles are in the lowest Landau level with energy $\hbar\omega_L$. In the current system, for $b$ so large that $(2b)^2 \gg \mathcal{N}_e$, for which all the occupied levels are on the lowest Landau sheet ($n_L = 0 : n_r = 0, l \leq 0$), $\mathcal{M} \to -\mathcal{N}_e\mu_B$. Except for this limit, $\mathcal{M}$ does not oscillate between $\pm\mathcal{N}_e\mu_B$, and it is mostly negative (i.e., $\frac{\partial E_{tot}}{\partial B} \gtrsim 0$) all the way through its dHvA oscillations, with much smaller amplitudes. The difference is that there are not separate and degenerate levels, but the Landau sheets of continuous levels. Each peak in the dHvA oscillations occurs when the Fermi energy gets out of one Landau sheet, not like jumping down from a Landau level to the next lower one.

### 4.2.2 Density of states and connection to classical orbits

Any response function of a many-fermion system will reflect characteristics of the density of states at the Fermi energy, which determines how easily the system can respond. The magnetization and susceptibility are directly related to the density

of states $g(E)$ , as they are the first- and second-order response of the total energy $E_{tot} = \int_0^{E_F} dE\, g(E)\, E$ to changes in magnetic field. Thus we expect to see the basic features of these response functions in $g(E)$ also, and this will enable us to interpret them in terms of classical orbits through periodic orbit theory. We saw in the last chapter that as shell corrections involve an energy integration ($\delta E = E_{tot} - \tilde{E}_{tot}$, where $\tilde{E}_{tot}$ is the smooth part of $E_{tot}$), they reflect $g(E)$ in a somewhat smoothed way. This is why the overall supershells of the metal clusters can be understood in terms of the shortest periodic orbits of high degeneracy, the triangular and square orbits. The shell structure of the magnetization may also be connected to shortest orbits in the classical system, and we smooth the density of states a little to see this connection.

For the harmonic-oscillator system we have an analytical expression for the density of states. In the present case, a two-dimensional anisotropic oscillator, the analytical expressions are different for rational and irrational ratios of the two frequencies, $\omega_\pm$ here. For irrational ratios the density of states is written as [Brack 94, Brack 97]

$$g(E,B) = \frac{E}{(\hbar\omega)^2} + \sum_{n=1}^{\infty}(-)^n \left[ \frac{\sin\left(n\frac{2\pi E}{\hbar\omega_+}\right)}{\hbar\omega_+ \sin\left(n\pi\frac{\omega_-}{\omega_+}\right)} + \frac{\sin\left(n\frac{2\pi E}{\hbar\omega_-}\right)}{\hbar\omega_- \sin\left(n\pi\frac{\omega_+}{\omega_-}\right)} \right] . \qquad (4.6)$$

Even for rational ratios, one may use this formula by making the ratio irrational by adding a small irrational number. The oscillating term $\delta g(E)$ in the above equation can be obtained as the Gutzwiller trace formula from the classical orbits – this is one of the cases where the Gutzwiller formula is exact [Brack 95]. In the system

of an isotropic oscillator or anisotropic one with rational frequency ratios, there are continuous families of degenerate orbits. In the case of irrational ratios, however, there are only two kinds of primitive periodic orbit, one with the frequency $\omega_+$ and the other one with $\omega_-$. Orbits that involve both of these frequencies, e.g., Lissajous trajectories, will never close, and the two primitive periodic orbits are isolated in the phase space. It is thus simpler to understand the characteristics of $\delta g$ by applying the above formula, in terms of these two primitive length or time scales in this system.

We smooth the density of states by convoluting Eq.(4.6) with a normalized Gaussian of width $\gamma$, that is to replace each delta function in $g(E) = \sum_{n_r,l} \delta(E - E_{n_r,l})$ by $\frac{1}{\gamma\sqrt{\pi}} e^{-((E-E_{n_r,l})/\gamma)^2}$. We are interested in the smoothed oscillating part $\delta g_\gamma(E)$ in order to see the shell structure : The term $\sin(n\frac{2\pi E}{\hbar\omega_\pm})$ is now multiplied by a factor $e^{-(\gamma T_{\pm,n}/2\hbar)^2}$, where $T_{\pm,n} = n\frac{2\pi}{\omega_\pm}$ is the period of the $\omega_\pm$ oscillation with $n$ repetitions. Consequently contributions from the orbits with longer periods (many repetitions) will be damped away. In Fig.4.4(a) we plot $\delta g_\gamma(E_F, b)$ for $\mathcal{N}_e = 100$ as a function of $b$, the two terms in Eq.(4.6) separately, with the width $\gamma = 0.2\,\hbar\omega$ and with $n \leq 20$. The solid line is the first term in $\delta g$, the $\omega_+$ contribution and the dotted line is the second term, the $\omega_-$ contribution. Now we can clearly see the supershells at smaller $b$ as a beating effect between the two frequencies which are comparable, and then as $b$ becomes large, there is only one frequency $\omega_+$ that determines the overall behaviour of the shell structure, i.e., the dHvA oscillations. In fact with this smoothing width, the $\omega_-$ contribution has been damped away completely for $b \gtrsim 2$.

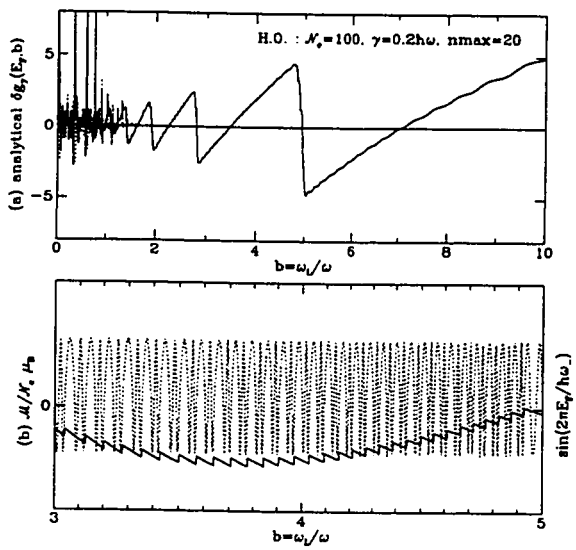


Figure 4.4: (a) The $\delta g_\gamma(E_F, b)$ in Eq.(4.6), with the smoothing width $\gamma = 0.2\hbar\omega$ and with $n \leq 20$, for $\mathcal{N}_e = 100$ as a fuction of $b$. The contribution from $\omega_+$ (the first term in $\delta g$) and that from $\omega_-$ (the second term) are plotted separately, in solid and dotted lines respectively. (b) Comparison of $\mathcal{M}$ (solid line) and the term $\sin\left(\frac{2\pi E_F}{\hbar\omega_-}\right)$ (dotted line) for $\mathcal{N}_e = 100$ for $3 \leq b \leq 5$. Note that there are two oscillations in $\sin\left(\frac{2\pi E_F}{\hbar\omega_-}\right)$, i.e., $\Delta\left(\frac{E_F}{\hbar\omega_-}\right) = 2$, for each small oscillation in $\mathcal{M}$.

The classical equations of motion for the Hamiltonian (4.1) may be written in terms of the coordinate $z = x + iy$ as

$$\ddot{z} = -\omega^2 z + 2i\omega_L \dot{z} \,. \tag{4.7}$$

The first term is the linear harmonic force due to confinement and the second term is the Lorentz force that results in cyclotron orbits when $\omega = 0$. The general solution of this is $z = Ae^{i\omega_+ t} + Be^{-i\omega_- t}$, with $A$ and $B$ constants. We can immediately see that we have closed periodic orbits whenever the ratio of $\omega_+$ and $\omega_-$ is rational. The above solution may be written in the $x$ and $y$ coordinates as

$$\begin{aligned} x &= R_1 \cos(\omega_+ t + \alpha) + R_2 \cos(\omega_- t + \beta) \\ y &= R_1 \sin(\omega_+ t + \alpha) - R_2 \sin(\omega_- t + \beta) \,, \end{aligned} \tag{4.8}$$

where we have written $A$ and $B$ in terms of real constants as $A \equiv R_1 e^{i\alpha}$ and $B \equiv R_2 e^{-i\beta}$. The energy $E$ and angular momentum $L_z = xp_y - yp_x$ are written in terms of the amplitudes $R_{1,2}$ and the ratio $b = \omega_L/\omega$ as

$$E = m_e^* \Omega (R_1^2 \omega_+ + R_2^2 \omega_-) \tag{4.9}$$

$$L_z = m_e^* \Omega (R_1^2 - R_2^2) \,. \tag{4.10}$$

Thus for a given energy $E$ and field $b$, angular momentum is restricted in the range $-\frac{E}{\omega_-} \leq L_z \leq \frac{E}{\omega_+}$ : The maximum and minimum $L_z$ correspond to $R_2 \equiv 0$ and $R_1 \equiv 0$, or the minimum and maximum amplitude for a given $E$, respectively. When $\omega = 0$, $\omega_+ \equiv \omega_c$ and $\omega_- \equiv 0$, and we have cyclotron orbits with $E = \frac{1}{2} m_e^* R_1^2 \omega_c^2$

and $L_z = \frac{1}{2}m_e^* R_1^2 \omega_c = \frac{E}{\omega_c}$, i.e., fixed angular momentum for a given energy. At the isotropic-oscillator ($b = 0$) end, we have a continuous spectrum of orbits for a given $E$ with angular momentum $-\frac{E}{\omega} \leq L_z \leq \frac{E}{\omega}$.

When $b$ is large ($\omega_+ \to \omega_c$ and $\omega_- \to 0$), the orbit with the maximum $L_z$ (anti-clockwise circular motion with frequency $\omega_+$ and the minimum amplitude) approaches to the cyclotron orbit, whereas the spectrum of orbits extends to negative larger $L_z$ that is not reachable for the same $E$ when $b = 0$. The orbits with large negative $L_z$ are "skipping orbits" for this system with a soft boundary, e.g., cycloidal motion [Darwin 30]. The one with the negative maximum $L_z$ is the limiting case of these skipping orbits, that is clockwise circular motion with frequency $\omega_-$ and the maximum amplitude for a given $E$. Hence this limiting case of skipping orbit is like going along the edge of the system that is effectively set by the energy – let us call this an "edge orbit". If the ratio of $\omega_+$ and $\omega_-$ is irrational, these two circular orbits are the only primitive periodic orbits.

We have seen in Fig.4.4(a) that the nearly-cyclotron orbits with $\omega_+$ give rise to the overall dHvA oscillations in $\mathcal{M}$. The small shell oscillations on each dHvA oscillation must come from longer orbits that involve $\omega_-$, i.e., the edge orbits when the frequency ratio is irrational. This is obviously the case as seen in Fig.4.4(b), where we plot the term $\sin\left(\frac{2\pi E_F}{\hbar\omega_-}\right)$ as a function of $b$ along with $\mathcal{M}$ for $3 \leq b \leq 5$ : We can see that the small oscillations in $\mathcal{M}$ coincide with those in $\sin\left(\frac{2\pi E_F}{\hbar\omega_-}\right)$. In fact, in Fig.4.4(a) the smoothing width was large enough so that the contribution of these edge orbits to $\delta g_\gamma$

was completely damped away in this strong-field region. These small oscillations in $\mathcal{M}$ are of the AB-type [Meir 90], and we can interpret them in terms of the classical edge orbits.

In Fig.4.4(b) we see two oscillations in $\sin\left(\frac{2\pi E_F}{\hbar\omega_-}\right)$ per small oscillation in $\mathcal{M}$, that is, the change in $\frac{E_F}{\hbar\omega_-}$, $\Delta\left(\frac{E_F}{\hbar\omega_-}\right) = 2$. In this strong-field limit, we can define the effective area of the system for a given energy by the area enclosed by the edge orbit. From Eq.(4.9), for $\omega_L \gg \omega$, the radius $R_2$ is given approximately as $R_2^2 = \frac{2E}{m_e^*\omega^2}$. (The same effective radius can also be obtained by the virial theorem, $m_e^*\Omega^2\langle r^2\rangle = E - \omega_L L_z$, where $\langle r^2\rangle$ and $L_z = l\hbar$ are related by $\langle r^2\rangle = \frac{\hbar}{m_e^*\Omega}(2n_r + |l| + 1) \simeq \frac{\hbar}{m_e^*\Omega}|l|$ $(|l| \gg 1)$. Note that this yields $\langle r^2\rangle$ twice as large as the one given by the virial theorem for zero field, $\frac{E}{m_e^*\omega^2}$.) Thus $\frac{E_F}{\hbar\omega_-} \simeq \frac{eB}{hc}\pi R_2^2 = \frac{\phi}{\phi_0}$, where $\phi$ is the magnetic flux enclosed in the effective area and $\phi_0 = hc/e$. Therefore $\Delta\left(\frac{\phi}{\phi_0}\right) = 2$, that is, two flux quanta are added to the system for each small oscillation in $\mathcal{M}$. This is different from the case with the usual Landau levels, as we will see later for disc confinement. In such a case, as the magnetic flux is increased by $\phi_0$, an edge state crosses the Fermi energy which stays on one Landau level during a dHvA oscillation. This causes a particle to move down from the Landau level to the edge state, resulting in an AB oscillation in $\mathcal{M}$. In the current case, since there are no degenerate Landau levels, $E_F$ itself oscillates as a function of $b$, as it moves from one Landau sheet to another. Each of the AB oscillations in Fig.4.4(b) takes place in two steps : As $\phi$ is increased by $\phi_0$, first $E_F$ moves from the second $(n_L = 1)$ Landau sheet to the lowest $(n_L = 0)$

one as a particle moves down, and then $E_F$ moves back to the second Landau sheet as another $\phi_0$ is added to the system. While $E_F$ is on the lowest Landau sheet, it decreases as $b$ increases, whereas when $E_F$ is on the second Landau sheet, it increases as $b$ increases. This is why the two oscillations of $\sin\left(\frac{2\pi E_F}{\hbar\omega_-}\right)$ per AB oscillation in $\mathcal{M}$ in Fig.4.4(b) have different periods.

It has been shown in Ref.[Meir 90] that the AB oscillations appear, superimposed on the dHvA oscillations, each of them corresponding to variation of the magnetic flux in the system by one flux quantum. In Fig.4.4(b) we see two oscillations in $\sin\left(\frac{2\pi E_F}{\hbar\omega_-}\right)$ per small oscillation in $\mathcal{M}$, that is, the change in $\frac{E_F}{\hbar\omega_-}$, $\Delta\left(\frac{E_F}{\hbar\omega_-}\right) = 2$. If we define the effective radius of the system by the virial theorem, $\langle r^2\rangle = \frac{E_F}{m_e^*\omega^2}$, (this yields the effective area of the original system which the magnetic field goes through) and use $\omega_- \simeq \frac{1}{2}\frac{\omega^2}{\omega_L}$ for large $b$ ($\omega_L >> \omega$), then we have $\frac{E_F}{\hbar\omega_-} \simeq \frac{eB}{\hbar c}\langle r^2\rangle = 2\frac{\phi}{\phi_0}$. Here $\phi$ is the magnetic flux enclosed by the effective area of the system $\pi\langle r^2\rangle B$, and $\phi_0$ is the flux quantum $hc/e$. Thus $\Delta\left(\frac{E_F}{\hbar\omega_-}\right) \simeq 2\Delta\left(\frac{\phi}{\phi_0}\right) = 2$ is consistent with one flux quantum added to the system, $\Delta\left(\frac{\phi}{\phi_0}\right) = 1$. Therefore the small oscillations on the dHvA oscillation seen in Fig.4.4 are the AB oscillations, and now its connection to the classical edge orbits is clear.

### 4.2.3 Semiclassical value of the magnetization

It is worth noting that the smooth or Thomas-Fermi (TF) density of states, $g_{TF}(E) = \frac{E}{(\hbar\omega)^2}$ in Eq.(4.6), does not depend on the magnetic field. In the strong-field limit, the Landau sheets are formed and $g(E)$ for a given $b$ has a series of plateaus whose height increases as $E$ increases[Brack 96]. We can see that $g_{TF}(E)$ still describes the average behaviour of $g(E)$ for the Landau sheets as follows. As discussed above, in the strong-field limit, the effective area of the system is set by the edge orbit for a given $E$. For a given $b$, the states on each Landau sheet increase in energy as a function of the radius $\sqrt{\langle r^2 \rangle}$ or $|l|$ ($l \leq 0$). For $b \gg 1$, we can assume that these levels within the effective area are almost degenerate and approximate the average density of states as $\frac{1}{\hbar\omega_c}$, as for the actual Landau levels, times the number of levels within the effective area, $\frac{eB}{hc}\pi R_2^2$. This yields the smooth density of states as $\frac{E}{(\hbar\omega)^2}$, which is $g_{TF}(E)$ above.

The fact that the effect of a magnetic field does not come into the TF value of the density of states is indeed general and equivalent to Van Leeuwen's theorem, which states that the classical susceptibility of an electron gas is zero. That is, the classical partition function $Z_{cl} = \int d\mathbf{r} \int d\mathbf{p}\, e^{-\hat{H}/k_B T}$ is invariant under the variable change $\mathbf{p} \rightarrow \mathbf{p} + \frac{e}{c}\mathbf{A}$, and $g_{TF}(E) = \mathcal{L}_E^{-1} Z_{cl}$. The Landau susceptibility is the first-order $\hbar$ correction to the classical value. Bhaduri and Jennings [Bhaduri, Jennings 76] have obtained the Landau susceptibility from the leading $\hbar$ correction to $Z_{cl}$ in the Wigner-

Kirkwood expansion, in a general form as $\chi_L \equiv -\frac{1}{3} g_{TF}(E_F)\mu_B^2$, for any smooth confining potential. Thus the Landau susceptibility may be understood as a "semiclassical" value of the susceptibility that corresponds to the leading-order $\hbar$ correction to the TF density of states. Let us define the "semiclassical" value of the magnetization determined by the Landau susceptibility as $\tilde{\mathcal{M}}_L \equiv \chi_L B$. It is plotted in Fig.4.3(a) and (b) with dotted lines and we can see that it yields smooth behaviour against the shell oscillations in the quantum magnetization $\mathcal{M}$.

One might expect that the quantum susceptibility $\chi$ itself oscillates around its semiclassical value $\chi_L$ between positive and negative values, as $\mathcal{M}$ in Fig.4.3 appears to have both positive and negative slopes. This is not the case, however, as seen in Fig.4.3(c). The $\chi$ is always negative for any value of $b$, approaching 0 as $b$ becomes large. The latter corresponds to the situation that all the particles are on the lowest Landau sheet, and the energy levels increase almost linearly in $b$ as the actual Landau levels. That the quantum susceptibility is always negative and approaches zero eventually as a function of the magnetic field, is also the case for hard-wall confinement. The negative $\chi$ means that $\mathcal{M}$ has a negative slope at each value of $b$, and this can be understood from the fact that the single-particle levels are always concave-up, i.e., $\frac{\partial^2 E_{tot}}{\partial B^2} > 0$. In fact, this is not the case for a quantum dot within which the classical dynamics is chaotic. At stronger magnetic fields applied to a dot, e.g., of an elliptic shape, "avoided crossings" of energy levels occur as a function of the field [Nakamura 93]. When there are avoided crossings, some (occupied) single-particle

levels are concave-down and add positive value to $\chi$, and hence $\chi$ may jump up to positive values. It has also been discussed in the literature that $\chi$ oscillates around $\chi_L$ at higher temperatures. Such oscillations of the susceptibility happen when $k_BT$ is much greater than the level spacings but is of the order of the energy $\hbar v_F/R$, where $v_F$ is the Fermi velocity and $R$ the size of the system [Shapiro 93, Ullmo 95, Richter 96].

As discussed above, the Landau susceptibility $\chi_L$ is the semiclassical value, which in a usual statistical-mechanical treatment, is obtained in the high-temperature or weak-field limit, $\mu_B B \ll k_B T$ : For zero temperature, it is obtained in the limit of $B \to 0$. It may also be understood as the "bulk" value in the limit that the system is very large, or the confining potential is weak enough so that even in the limit of $B \to 0$, the system has the (quasi-) Landau-level structure, or classically the (quantized) cyclotron orbits. This corresponds in the current system to the limit $\omega \to 0$. In fact, if the system is "small", or the confining potential is so strong that it dominates the quantum level structure as $B \to 0$, the semiclassical susceptibility is different from the Landau value. One finds that in the limit of $B = 0$ in the current system, where the energy levels are basically those of the isotropic harmonic oscillator with Zeeman splittings, the semiclassical susceptibility is proportional to $E_F^3$, rather than $E_F$ as in $\chi_L$. This can be seen as follows : The quantum susceptibility (at $T = 0$) for arbitrary $B$ is obtained from Eq.(4.5) as

$$\chi(B) = \frac{\partial \mathcal{M}}{\partial B} = -\frac{\mu_B^2}{\hbar\omega}\left(\frac{\omega}{\Omega}\right)^3 \sum_{n_r,l}^{\leq E_F} (2n_r + |l| + 1) \,. \tag{4.11}$$

In the limit $B \to 0$, $\Omega \to \omega$ and $\chi(0) = -(\frac{\mu_B}{\hbar\omega})^2 \sum \hbar\omega(2n_r + |l| + 1)$. If the field is weak enough so that up to the Fermi energy $E_F$, there is no level crossing due to Zeeman splittings, the lowest $\mathcal{N}_e$ levels are the same lowest ones as for $B \equiv 0$. That is, the sum in $\chi(0)$ is nothing but the total energy for zero field, $E_{tot}(0)$, as we can see by setting $\omega_L = 0$ in the energy levels (4.3). It is interesting that the susceptibility is nonzero as $B \to 0$ in this strong-confinement limit, whereas one might expect it to be zero, as the energy levels are dominated by the Zeeman terms linear in $B$ and the effect of $B^2$ is negligible in this limit : It is indeed the quadratic term that results in nonzero $\chi(0)$.

We define the "semiclassical" value of $\chi(0)$ by replacing $E_{tot}(0)$ with its smooth or TF part $\tilde{E}_{tot}(0)$. That is, $\tilde{E}_{tot}(0) = \int_0^{E_F} dE\, E\, g_{TF}(E) = \frac{E_F^3}{3(\hbar\omega)^2}$. Thus the semiclassical susceptibility in this strong-confinement limit is given as

$$\chi_H \equiv -\frac{1}{3}\frac{E_F^3}{(\hbar\omega)^2}(\frac{\mu_B}{\hbar\omega})^2 . \tag{4.12}$$

The semiclassical magnetization $\tilde{\mathcal{M}}_H \equiv \chi_H B$ is plotted, using dashed lines, in Fig.4.3(a). We can see for $\mathcal{N}_e = 36$ (closed shell for $b = 0$) that $\tilde{\mathcal{M}}_H$ is almost indistinguishable from the exact $\mathcal{M}$ in the given scale, until the first crossing (the first dip in $\mathcal{M}$) occurs. (Note that the smooth part $\tilde{E}_{tot}(0)$ is the leading term in $E_{tot}(0)$.) The $\tilde{\mathcal{M}}_H$, however, ceases to be the smooth part of $\mathcal{M}$ right after the first level-crossing. Soon after, in fact for $b \ll 1$, the Landau susceptibility starts yielding the right smooth behaviour of the magnetization.

### 4.2.4 Effect of spins

Let us now consider the effect of electron spins. In a usual free electron gas, e.g., in a metal, it will contribute to the Zeeman term as $B\mu_B g S_z$, where $g$ is the Landé factor ($\simeq 2$ in normal metal) and $S_z$ is the $z$-component of the electron spin $1/2$. The Landau levels then become $\hbar\omega_c(n+1/2\pm 1/2)$ $(n = 0, 1, 2, ...)$, where the $\pm$ sign corresponds to the spin aligned or anti-aligned with the direction of the magnetic field. In the strong-field limit the spin paramagnetism is stronger than the orbital diamagnetism, with the semiclassical value given by the Pauli susceptibility, $\chi_P \equiv g(E_F)\mu_B^2$, which makes the total semiclassical susceptibility positive. The total magnetization oscillates around the semiclassical value $(\chi_L + \chi_P)B$ again for the entire range of $b$ except for $b \ll 1$ (after the first level-crossing for a given $\mathcal{N}_e$). It has finer shell structure superimposed on the dHvA oscillations, compared to the orbital magnetization itself in Fig.4.3(a). This is because some levels are now degenerate with different combinations of $L_z$ and $S_z$ of opposite signs.

In the actual GaAs quantum dots, the electron has an effective mass $m_e^*$ associated with its orbital motion in the semiconductor, which is much lighter than the actual mass. However, the actual mass comes into the dipole moment due to spin, as it has nothing to do with the electron's orbital motion. On the other hand, the orbital motion affects the spin dipole moment through the Landé factor, which is related to the orbital angular momentum and for GaAs, $g^* = -0.44$. The Zeeman energy due to

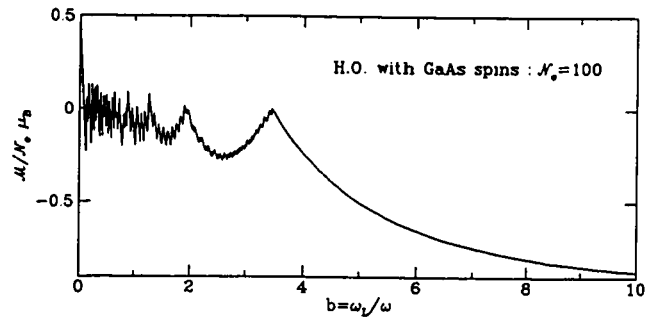


Figure 4.5: Magnetization for the harmonic confinement for $\mathcal{N}_e = 100$ with spins included with the Landé factor $g^* = -0.44$ for GaAs. Note the finer structure in the last dHvA oscillation compared to the one in Fig.4.3(a) with the same $\mathcal{N}_e$.

spins is further reduced relatively against the energy of the orbital motion by the ratio of $m_e^*/m_e$. It results in much smaller level splittings compared to the bare spin effect as discussed above [Ashoori 93]. We plot in Fig.4.5 the magnetization for $\mathcal{N}_e = 100$ with spins included. It has basically the same structure as the orbital one in Fig.4.3(a) (Note that the Fermi energy in this case is lower than the one for Fig.4.3(a) with the same $\mathcal{N}_e$, due to the spin degeneracy), except that it has smaller shell structure superimposed on the dHvA oscillation at larger $b$, where the spin splittings become visible. Thus in this mean-field picture, the effect of spins is negligible and we will consider only the orbital magnetism in the next section for hard-wall confinement.

## 4.3 Hard-wall Confinement

### 4.3.1 Quantum energy levels and magnetization

We next examine the case with the circular hard-wall or "disc" confining potential $V(r) = 0$ $(r < R)$ $; \infty$ $(r \geq R)$ in Eq.(4.1). This system is the two-dimensional version of the one we have studied in the last chapter, free electrons in a spherical cavity in a uniform magnetic field. Unlike its three-dimensional counterpart, under a uniform magnetic field applied perpendicular to the dot, the cylindrical symmetry that the system originally had is preserved and the system remains integrable. It is interesting to compare the two- and three-dimensional cases, especially regarding the shell structure and classical orbits.

We again scale the Hamiltonian by the natural energy unit of the system $E_0 = \hbar^2/2m_eR^2$ and define the parameter $\kappa = \hbar\omega_L/E_0 = (R/l_0)^2$. The scaled energy is written as $E = (kR)^2$ in terms of the dimensionless wave number $kR$, the natural energy variable for the original system. The energy eigenvalue $E_{n_r,l}$, with the nodal and angular-momentum quantum numbers $n_r$ and $l$ as defined in the last section, is given by the $(n_r + 1)$-th zero of the confluent hypergeometric functions ${}_1F_1(-\alpha_{n_r,|l|}; |l| + 1; \kappa/2)$ [Geerinckx 90]. However, it is numerically easier to obtain the eigenvalues by diagonalizing the radial part of the Hamiltonian (4.1) in the basis of the cylindrical Bessel functions $J_{|l|}(k_{n'_r,|l|}r)$, where $k_{n'_r,|l|}$ is the wave-number eigenvalue of the original system ($\kappa = 0$), the $(n'_r + 1)$-th zero of $J_{|l|}$. The energy

eigenvalues $\{E_{n_r,l}\}$ thus obtained from the diagonalization agree very well with those obtained from the zeros of the confluent hypergeometric functions, and we use these eigenvalues for further calculations.

In Fig.4.6, we show the energy levels $\{E_{n_r,l}\}$ as a function of $\kappa$, scaled by the lowest level $E_{1,0}$ in the zero field case. As we will see later, the original system exhibits supershell structure, i.e., a beating pattern in the shell structure, like its three-dimensional counterpart, although the beating pattern is not as prominent. We will discuss this point later in terms of classical orbits. In Fig.4.6 we can see the change of the beat structure as $\kappa$ is varied, as lighter and denser regions of levels or positions of quasi gaps alternate. The main difference from the system of metal clusters and also the merit which the system of quantum dots has, is that the size of a quantum dot can be much larger, up to the order of microns. This means that with a magnetic field of the order of milli-Tesla, already $\kappa \sim 1$. Thus in a physical system $\kappa$ may become very large and we can observe formation of the Landau levels also. For larger $\kappa$ in Fig.4.6, we see clearly the formation of the distinct, highly-degenerate Landau levels : The dotted lines radiating from the origin, which are the actual Landau levels, become indistinguishable from the levels that condense into one of them.

We look at the magnetization $\mathcal{M}$ for $\mathcal{N}_e = 100$ in order to compare with that in harmonic confinement in Fig.4.3(a). The $\mathcal{M}$ is shown in Fig.4.7 for (a) $\kappa \leq 60$ and (b) $\kappa \leq 300$. In the latter figure for longer range, we can see rapid beat oscillations

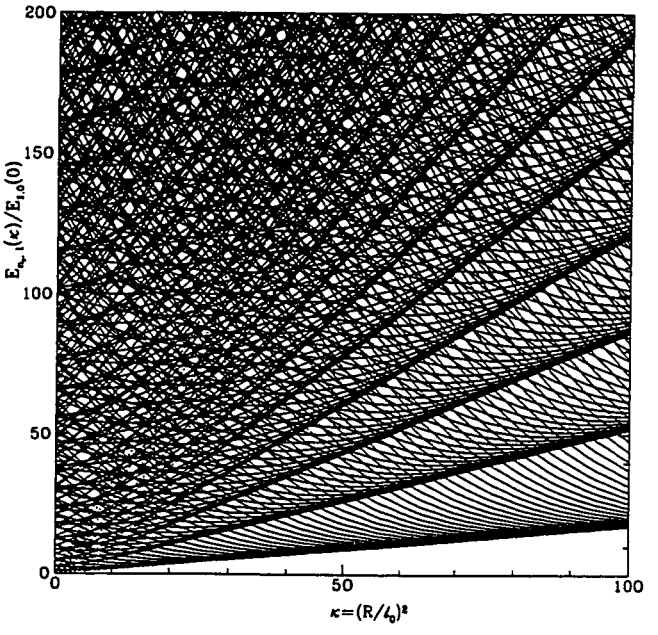


Figure 4.6: Energy levels for the disc confinement as a function of $\kappa = (R/l_0)^2$, scaled by the lowest level for $\kappa = 0$. The dotted lines are the Landau levels, which are indistinguishable with the levels that condense into one of them at larger $\kappa$.

for $\kappa \lesssim 50$ and the dHvA oscillations for larger $\kappa$. The dHvA oscillations in $\mathcal{M}$ are more pronounced in this case, and it has regular, small subshells on the rising side of the last two peaks, like we saw in $\mathcal{M}$ with the harmonic oscillator potential. Beyond the last peak at $\kappa \simeq 200$, $\mathcal{M}$ quickly approaches -1 and here all the particles are in the lowest Landau level. Accordingly the susceptibility goes to zero, as seen in Fig.4.7(d). For a quantum dot with radius $R$ of the order of microns, the value of $\kappa = 300$ corresponds to $B \simeq 0.2$ T.

The dotted line around which the quantum $\mathcal{M}$ oscillates is the semiclassical magnetization $\tilde{\mathcal{M}}_L = \chi_L B$. The TF density of states in this case is independent of energy, $g_{TF}(E) = \frac{1}{4E_0}$, and thus the Landau susceptibility $\chi_L$ is given as $-\frac{1}{12E_0}\mu_B^2$. As discussed in the last section, the TF density of states is not affected by a magnetic field. Indeed this $g_{TF}(E)$ turns out correctly to be the smooth part of the density of states for the Landau levels ; $1/\hbar\omega_c$ times the degeneracy, i.e., the number of the flux quanta in the area of the system, $\pi R^2 eB/hc = \kappa/2 = \hbar\omega_c/4E_0$. This agrees with the fact that, as there is no force from the confining potential inside the hard-wall boundary, the Landau levels are built if the magnetic field is strong enough so that the magnetic length, or classically the cyclotron radius, is much smaller than the radius of the disc. As we have seen in the last section, if the effective single-particle potential is of harmonic oscillator, the system does not yield the exact Landau levels. Thus the appearance of the Landau levels, which can be seen in the magnetization as in Fig.4.7, will be an indication that the effective potential has a flat bottom, even

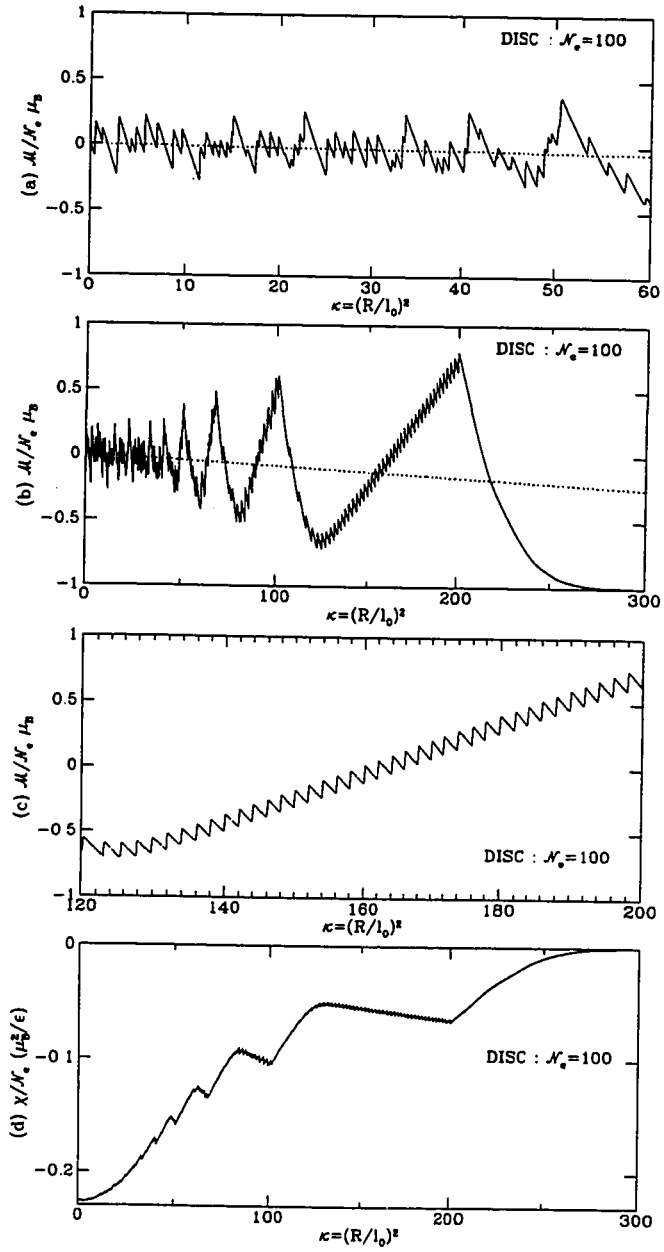


Figure 4.7: Magnetization for the disc confinement for $\mathcal{N}_e = 100$ as a function of $\kappa$ for (a) $0 \leq \kappa \leq 60$, (b) $0 \leq \kappa \leq 300$, and (c) $120 \leq \kappa \leq 200$ ; we can clearly see the regular oscillations with a period $\Delta\kappa = 2$ on the last dHvA oscillation. (d) Susceptibility for the disk with $\mathcal{N}_e = 100$.

though the device potential for a quantum dot is harmonic.

### 4.3.2 Density of states and connection to classical orbits

We can see the formation of the Landau levels also in the oscillating part of the density of states $\delta g(E_F, \kappa)$. In Fig.4.8(a) we show the Gaussian-smoothed $\delta g_\gamma(E_F, \kappa)$ for $\mathcal{N}_e = 100$ obtained from the quantum eigenvalues with $\gamma = 0.8\sqrt{E}$. As discussed in the last chapter, the energy-dependent width corresponds to smoothing in the variable $kR = \sqrt{E}$ with a constant width and is suitable for the billiard system. For larger $\kappa$ the Landau levels start appearing as main shells with a constant energy gap, but there are always other levels that are yet to converge to one of these Landau levels. The $\delta g_\gamma$ in Fig.4.8(a) as a function of $\kappa$ looks quite different from that with harmonic confinement especially in the dHvA region. The peculiar oscillations seen in Fig.4.8(a) come from the Landau-level structure : whenever the Fermi energy lands on one of the degenerate Landau levels, $\delta g_\gamma(E_F, \kappa)$ jumps up to a positive value, and it keeps increasing as more levels come down to that Landau level, and then jumps down as $E_F$ goes down towards the next Landau level. This becomes clear if we compare $\delta g$ with that of the actual Landau levels.

The density of states for the Landau levels within the area of the disc is analytically written as

$$g_{L.L.}(E, \kappa) = \frac{1}{4E_0}[1 + 2\sum_{n=1}^{\infty}(-)^n \cos(n\frac{2\pi E}{\hbar\omega_c})] \,. \tag{4.13}$$

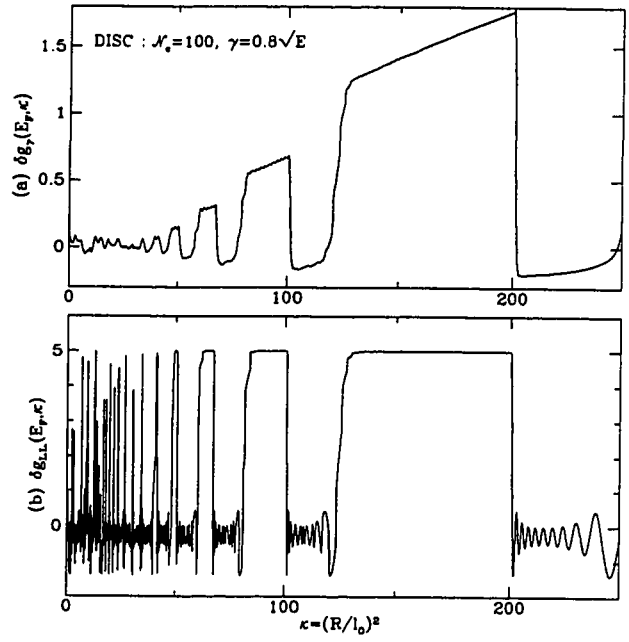


Figure 4.8: (a) The Gaussian-smoothed $\delta g_\gamma(E_F, \kappa)$ for the disc as a function of $\kappa$ with $\gamma = 0.8\sqrt{E}$. (b) The $\delta g_{L.L.}(E_F, \kappa)$ in Eq.(4.13), the density of states for the Landau levels in the disc, with $n \leq 10$. Both are for $\mathcal{N}_e = 100$. By comparing the two figures, the formation of the Landau levels becomes clear for $\kappa \gtrsim 50$, as discussed in the text.

We plot in Fig.4.8(b) $\delta g_{L.L.}(E_F, \kappa)$ with $n \leq 10$ without Gaussian smoothing ; as the oscillating part in this case is simply a cosine function of energy, it can be "smoothed" by summing a finite number of harmonics, and $n \leq 10$ seems to yield a smoothing comparable to Fig.4.8(a). In the above expression, we can see that if $E$ is on a Landau level, $E = \hbar\omega_c(n' + 1/2)$, the cosine term for a given $n$ reduces to $\cos(n\pi) = (-)^n$. Hence whenever the Fermi energy is on a Landau level, $\delta g_{L.L.}(E_F, \kappa)$ is a positive constant independent of $\kappa$, and this is seen in Fig.4.8(b). It is clear from this figure that the level structure is dominated by the Landau levels for $\kappa \gtrsim 50$, where the Fermi energy is on the fifth Landau level. This means that for $\kappa \gtrsim 50$, the shell structure is mainly governed by one frequency $\omega_c$, or one classical length scale that is the cyclotron radius.

In addition to the Landau levels, there are always edge states due to the finite size of the system, or finite number of flux quanta available for a given $\kappa$. These edge states give rise to finer shell structure as seen in $\delta g$ in Fig.4.8(a). This is seen more prominently in $\mathcal{M}$ in Fig.4.7, namely the small shell oscillations superimposed on the overall dHvA oscillations that are governed by $\omega_c$. Especially those on the last dHvA oscillation are very regular and pronounced. As predicted in Ref.[Sivan 88], these small oscillations are due to the AB effect ; each of them corresponds to one flux quantum added to the system and one edge state converges into a Landau level, as $\kappa$ is increased. In Fig.4.7(c), we show $\mathcal{M}$ for $120 \leq \kappa \leq 200$, i.e., a blow-up of the small oscillations on the last dHvA oscillation. We can see the very regular oscillations with

a period $\Delta\kappa = 2$. Hence $\Delta\kappa = 2 = 2\pi R^2 \frac{e}{\hbar c}\Delta B$ and this corresponds to a change in the flux $\Delta\phi = \pi R^2 \Delta B = hc/e$, that is, exactly one flux quantum $\phi_0$.

Classically the finer shell structure can be understood in terms of longer orbits that bounce around the boundary, i.e., skipping orbits. For a given energy and field strength, the shortest limit of the skipping orbits is the edge orbit that goes along the edge of the disc. Let us roughly evaluate its contribution to the semiclassical trace as the leading one from the skipping orbits. The classical action $S = \oint \mathbf{p} \cdot d\mathbf{q} = \oint (m_e^* \mathbf{v} - \frac{e}{c}\mathbf{A}) \cdot d\mathbf{q}$ for the edge orbit is written as $m_e^* v\, 2\pi R + \frac{eB}{c}\pi R^2$. Note the sign of the second line integral is negative due to the clockwise direction of the motion. Thus $S/\hbar = k\, 2\pi R + \kappa\pi$ and the field-dependent contribution of the edge orbit to the trace is basically $\cos(\kappa\pi)$. This yields oscillations as a function of $\kappa$ with a period $\Delta\kappa = 2$. Therefore the AB oscillations discussed above can also be explained simply in terms of the classical edge orbits.

### 4.3.3 Semiclassical analysis : disc v.s. spherical cavity

Let us conclude this section by looking at the relation between the quantum shell structure and classical periodic orbits in the weak-field region with smaller $\kappa$, where there is a variety of orbit families. The shell oscillations as a function of both the magnetic field and the dot radius (the number of electrons) have been observed in the conductance of large dots ($R \simeq 0.3 - 0.4\mu$m) in a weak magnetic field (-20

mT $\lesssim B \lesssim$ 40 mT) [Persson 95b, Reimann 96b]. Reimann *et al.* have explained these oscillations in terms of classical orbits of electrons in the disc, by expanding the semiclassical trace formula up to linear order in $B$ [Reimann 96b]. We examine changes in the shell structure, as well as in the classical orbit structure at smaller $\kappa$, in more detail within the first-order approximation. Our purpose here is to compare the effect of the field with that in the system of large metal clusters modeled as a three-dimensional version of the disc system.

When there is no field, all the classical periodic orbits are polygons which may be classified by the number of reflections at the disc walls $p$ and the number of turns around the centre of the disc $t$, with $p \geq 2t$ [Balian 72], and each of which forms a continuous family. The semiclassical trace formula is given as [Reimann 96a]

$$\delta g(E) = \frac{1}{\sqrt{\pi\, kR}} \sum_{t=1}^{\infty} \sum_{p=2t}^{\infty} f_{pt} \sqrt{\frac{\sin^3 \phi_{pt}}{p}} \sin\left( \frac{S_{pt}(E)}{\hbar} - 3p\frac{\pi}{2} + \frac{3\pi}{4} \right) , \qquad (4.14)$$

where $\phi_{pt} = \pi \frac{t}{p}$ and $S_{pt}(E) = \hbar k L_{pt}$ is the action of the orbit with length $L_{pt} = 2pR\sin\phi_{pt}$, and $f_{pt}$ is unity for the diametrical orbits with $p = 2t$ and it is 2 for the orbits with $p > 2t$. Here the natural unit for the density of states $1/E_0$ is set to unity, and $E$ is the dimensionless energy $E = (kR)^2$ as defined above.

The main difference in the classical orbit families in the disc system from its three-dimensional counterpart is that the diametrical orbits have the same degree of degeneracy as the other orbits with $p > 2t$. This is related to the lower symmetry (cylindrical U(1)) of the system compared to the three-dimensional case, which has

the SO(3) rotational symmetry. In the latter, each orbit with $p > 2t$ is threefold degenerate and forms a continuous family under rotation about three Euler angles, whereas the diametrical orbit is invariant under rotation about its own direction, thus having only twofold degeneracy. This is why its contribution to the shell structure is negligibly small, and consequently the next shortest, triangular and square orbits have the dominant contribution, giving rise to the pronounced beat effect. In the two-dimensional disc, however, there is only one plane of motion, and consequently the contribution from the diametrical orbits to the trace is comparable to that from the other polygonal orbits and is in fact one of the most dominant as they are the shortest. This is the reason that the shell structure of the original disc system does not have prominent beats as in the spherical cavity, but a more complicated interference pattern. This is somewhat similar to the situation in the cavity system under a uniform magnetic field, when the field is so strong that the higher degeneracy of the orbits with $p > 2t$ is removed and their contribution to the shell structure is comparable to that of the diametrical orbits. Note that this is within the first-order approximation, where the diametrical orbits are not affected by the field (see Fig.4.6 in the article in Chapter 3).

The difference in the orbit structure in the two- and three-dimensional cases may be seen clearly in the Fourier transform of the quantum level density :

$$f(L) = \int_0^\infty dk e^{-ikL} g(E) = \sum_{n_r,|l|} \frac{1}{k_{n_r,|l|}} e^{-ik_{n_r,|l|}L} , \qquad (4.15)$$

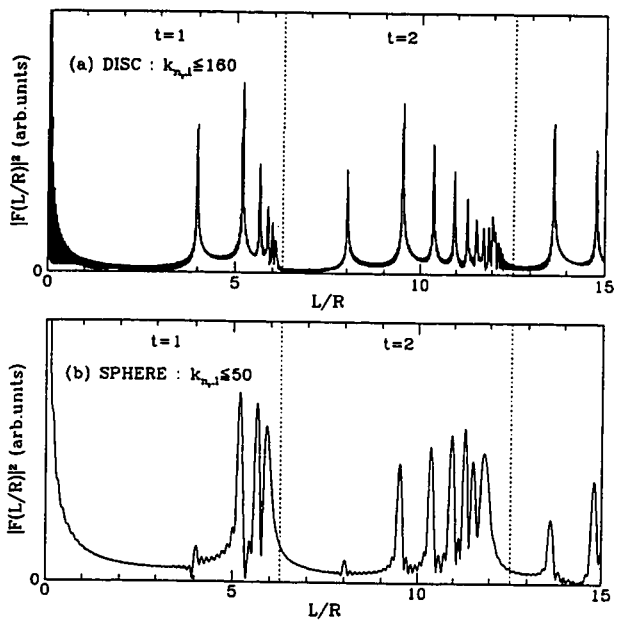


Figure 4.9: Fourier amplitudes of the density of states $g(E)$ for zero field, Eq.(4.15), as a function of the orbital length $L$ in units of the radius $R$. The cases of the (a) disc and the (b) sphere are compared. Note the difference in the peak heights for the diametrical orbits.

where $g(E) = 2\sum_{n_r,|l|}\delta(k^2 - k^2_{n_r,|l|})$ and $k_{n_r,|l|}$ is the wave-number eigenvalues as discussed above. This is shown in Fig.4.9(a) and compared with the three-dimensional case in Fig.4.9(b). The range of the wave number taken here is $k_{n_r,|l|} \leq 160$ for the disc and $k_{n_r,|l|} \leq 50$ for the sphere, and consequently the Fourier spectrum in Fig.4.9(a) has finer resolution than in (b). We can see the different "band" structure of orbits [Balian 72], which is classified by the number of turns around the origin $t = 1, 2, 3, ...$, and in which the difference in the dominance of the diametrical orbits is obvious.

When a uniform magnetic field is applied to this system, the cylindrical symmetry, i.e., the rotational symmetry about $z$ axis, remains. As long as the field is weak enough so that the cyclotron radius is larger than the disc radius, the structure of the classical orbits also remains the same in terms of their topology : the sides of each polygon will be bent due to the Lorentz force but these orbits can still be classified by the same parameters $(p, t)$ and each form a continuous family. As discussed in the last chapter, if the field is weak enough, the change in the action of an orbit can be approximated to first order in the field $B$ by the magnetic flux enclosed by the original orbit. The bending of the trajectory that changes the length of the orbit as well as the area enclosed by the orbit will result in changes in the action of the order of $B^2$. Thus to first order in $B$, $\Delta S_{pt} = \mp\frac{e}{c}BA_{pt}$, where $A_{pt} = R^2\frac{p}{2}\sin(2\pi t/p)$ is the area enclosed by the orbit $(p, t)$ and the $\mp$ corresponds to a positive or negative angular momentum i.e., counterclockwise or clockwise motion about $z$ axis, respectively. By adding this $\Delta S_{pt}$ to the original action in the trace formula (4.14) and averaging the contributions

from the two opposite senses of motion, we obtain the trace formula (4.14) with a factor $\cos(\Delta S_{pt}/\hbar)$ multiplied to the original contribution from each orbit family $(p,t)$. The same result may be obtained by applying the "trace formula for broken symmetry" [Creagh 96] as we have done for the cavity, though there is no symmetry breaking here. The modulation factor in this case is $\frac{1}{2\pi}\int_0^{2\pi} d\phi e^{\mp iF(pt;\kappa)} = e^{\mp iF(pt;\kappa)}$, where $F(pt;\kappa) = \kappa\frac{p}{2}\sin(2\pi t/p)$. As the field becomes strong (up to the point that the cyclotron radius becomes equal to the disc radius), the contribution from a given orbit oscillates with a constant amplitude, and there is no decay of the contributions. This is in contrast to the three dimensional case, where the modulation factor in first-order perturbation theory is the spherical Bessel function $j_0(\Delta S_{pt}/\hbar)$ whose amplitude decays as $\kappa$ increases. The difference is that in the current case there is no symmetry breaking and hence the orbit families are not destroyed by the perturbation, whereas in the spherical cavity, most of the families of periodic orbits are destroyed due to the symmetry breaking by the perturbation.

It is interesting to see how the shell structure changes as $\kappa$ is increased. In Fig.4.10 we plot the quantum $\delta g_\gamma(E)$ (solid lines) as a function of $kR = \sqrt{E}$, along with the semiclassical $\delta g_\gamma(E)$ (dotted lines) obtained from Eq.(4.14) or the perturbed trace formula for $\kappa \neq 0$. Here $\gamma$ is again taken as $0.8\sqrt{E}$. The semiclassical $\delta g$ is smoothed with the Gaussian factor $e^{-(\gamma T_{pt}/2\hbar)^2} = e^{-(\gamma_k L_{pt}/2R)^2}$, where $T_{pt} = L_{pt}/v(E)$, $v(E)$ is the velocity, and $\gamma = 2\gamma_k\sqrt{E}$ with $\gamma_k = 0.4$ in this case. With this smoothing width, the semiclassical $\delta g_\gamma$ converges, with both the number of sides $p$ and turns $t$ summed

up to 20.

As $\kappa$ increases, the original beating pattern in Fig.4.10(a) is smoothly transformed into a more regular beating pattern at $\kappa = 0.7$ shown in 8(b). This is gone at (c) $\kappa = 1$, and we have another supershell structure at (d) $\kappa = 2$. This disappearance and reappearance of different beating patterns keep repeating as $\kappa$ is increased further. This is a similar phenomena as we saw in the spherical cavity system. In the spherical cavity, however, substantial change in the original supershell structure does not happen until $\kappa$ is beyond 1 and the original beats are gone only at $\kappa \simeq 1.5$. Besides, $\kappa \simeq 0.5$ already corresponds to the maximum available field strength ($B \simeq 30$ T) for the largest size of a metal cluster ($R \simeq 30\mathring{A}$), and these changes in the shell structure are not presently observable. Thus not only is the same value of $\kappa$ translated into a much smaller $B$ for a quantum dot than that for a metal cluster, but the effect of the magnetic field with the same $\kappa$ value is larger in the disc system than in the cavity. In other words, the supershell structure in the cavity system is more robust against perturbation by the field. The difference comes from the symmetry of the system. Whereas the disc system has only one-dimensional rotational symmetry, U(1), the cavity system has much higher symmetry, SO(3). As a result when there is no field, the quantum levels in the cavity are highly degenerate, $2l + 1$ for each level with angular momentum $l$, whereas in the disc each level is only twofold degenerate with nonzero angular momentum. Classically the difference is in the degeneracy of each orbit family for the two systems as discussed above. In the disc, to first order in $B$, the

magnetic field perturbs all the orbits in a given family of $(p,t)$ with the same amount $\Delta S_{pt}$ evaluated above. In the spherical cavity, in addition to these orbits there are extra members of orbits in a family whose planes of motion are not on the $xy$ plane and as their angle with the $xy$ plane increases towards $\pi/2$, the perturbation in the action decreases towards zero. Hence for smaller $\kappa$ there are significant contributions from orbits that are little perturbed and this is why the original supershells are so robust.

Up to $\kappa = 2$ in Fig.4.10, $\delta g_\gamma$ obtained from the perturbed trace formula is almost indistinguishable with the quantum $\delta g_\gamma$, except for the slight difference at very low energy for $\kappa = 2$. At $\kappa = 5$ in Fig.4.10(e) it is seen that the semiclassical $\delta g_\gamma$ still reproduces the quantum results well, except for deviations at lower energies, $kR \lesssim 20$, now more apparent. At (f) $\kappa = 10$, the perturbed trace formula fails completely for $kR \lesssim 25$. This is due to the cyclotron orbits at lower energies missing in the perturbed trace formula. Thus for $\kappa \lesssim 5$, the perturbed trace formula works fairly well, and the changes in the shell structure can be understood semiclassically as due to changes in the magnetic flux enclosed by the original orbits. The maximum value $\kappa \simeq 5$ is consistent with $B \simeq 40$ mT for $R \sim 0.3\,\mu$m as pointed out in Ref.[Reimann 96b], up to which effects of higher order in $B$ can be safely neglected.

That the semiclassical perturbation theory works well up to $\kappa \simeq 5$ is also true for the spherical cavity system. It is interesting to see how far in $\kappa$ the first-order perturbation works quantum mechanically. In Fig.4.11, we compare the $\delta g_\gamma(E)$ obtained

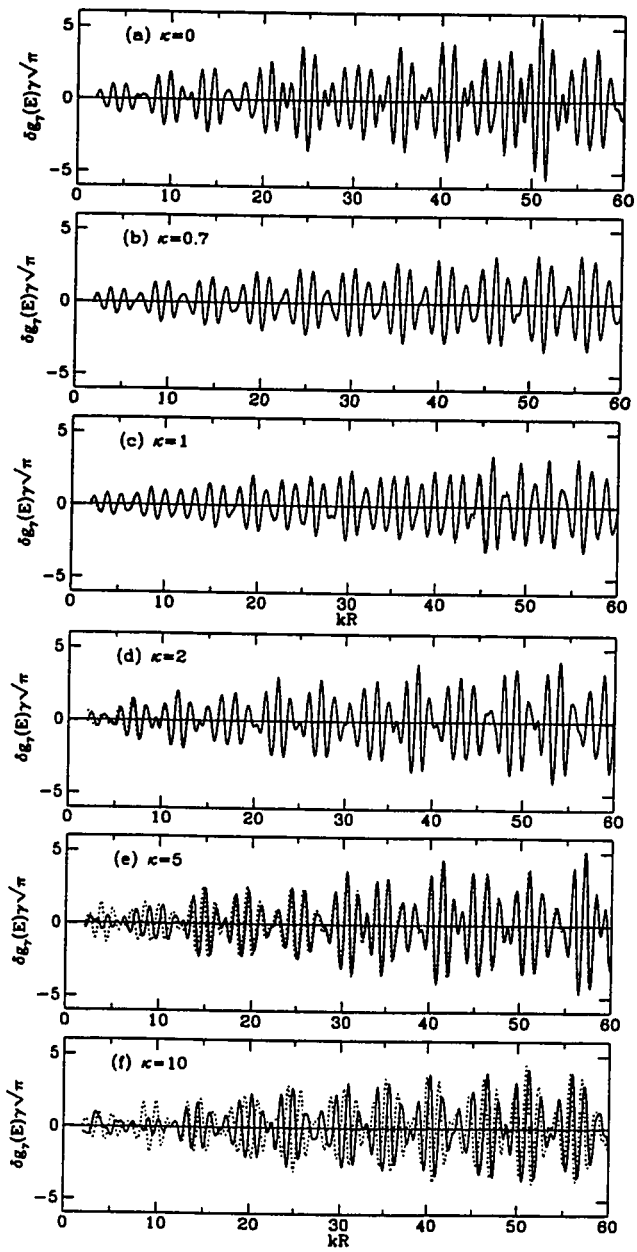


Figure 4.10: The oscillating part of the density of states $\delta g_\gamma(E)$ with the smoothing width $\gamma = 0.8\sqrt{E}$ as a function of $kR = \sqrt{E}$ for $\kappa = 0$, 0.7, 1, 2, 5 and 10. The quantum-mechanical $\delta g$ is plotted in solid lines and the semiclassical $\delta g$ from the perturbed trace formula in dotted lines.

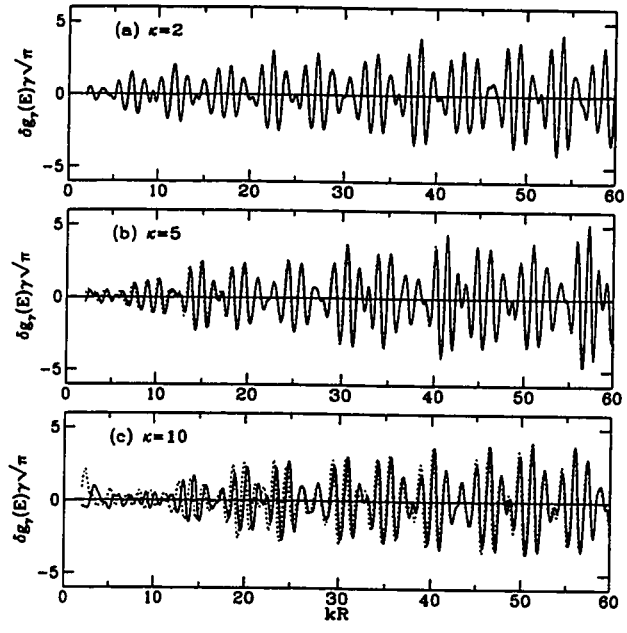


Figure 4.11: The quantum $\delta g_\gamma(E)$ as a function of $kR$ obtained from the exact eigenvalues (solid lines) and by including only Zeeman terms (dotted lines). $\gamma = 0.8\sqrt{E}$.

from the exact eigenvalues with that including only the Zeeman terms in Eq.(4.1), for $\kappa = 2, 5$ and 10. The quantum first-order perturbation reproduces the exact results quite well for $\kappa \lesssim 5$, whereas at $\kappa = 10$ deviations at low energy are substantial, especially failing to yield the Landau levels. Therefore the changes in the supershell structure for $\kappa \lesssim 5$ can be understood quantum mechanically as rearrangements of levels by the Zeeman splittings, which is also true for the cavity system.

To see the connection to classical orbits better, we take Fourier transforms of $\delta g_\gamma$ with respect to $kR$. As discussed in the last chapter, $\delta g$ for a given $\kappa$ as a function of $k$ contains a continuous spectrum of classical length scales and curvatures defined by

the cyclotron radius $R_c = m_e vc/eB = kl_0^2$. Hence the Fourier transform does not give the right length spectrum in the strict sense as for the field-free case. However, for small enough $\kappa$, for which we can neglect the curvature of the orbits, and for which the perturbative trace formula works, we can still interpret the Fourier spectrum in connection to the original orbits in first-order approximation.

In Fig.4.12 we show the Fourier amplitudes of $\delta g_\gamma(E)$ with the same smoothing width as in Fig.4.10 for $\kappa = 0, 0.7, 1$ and 2. For $\kappa = 0$ we see the dominance of the shortest few orbits lead by the diametrical one, while longer orbits are greatly suppressed by the smoothing width and only the $t = 2$ diametrical and the "star" $((p,t) = (5,2))$ orbits are visible. At $\kappa = 0.7$ the main contributions are only from the diametrical and the triangular orbits, and now we can understand the regular beating pattern of $\delta g_\gamma$ as an interference between these two orbits. Then at $\kappa = 1$ where the beating pattern is gone, we can see that $\delta g_\gamma$ is basically dominated by the diametrical orbit only, whereas all the other short orbits are largely suppressed. (Note that to first order in $B$, the diametrical orbits which enclose no area are not affected by $\kappa$.) For $\kappa = 2$ we have a similar configuration of contributions from the shortest orbits as for $\kappa = 0$, except for the pentagonal orbit. This explains the appearance of the new beats at $\kappa = 2$, which look quite similar to the original supershells. Thus up to $\kappa \sim 5$ we can see evidence of rearrangements of contributions from the original orbits in Fourier spectra.

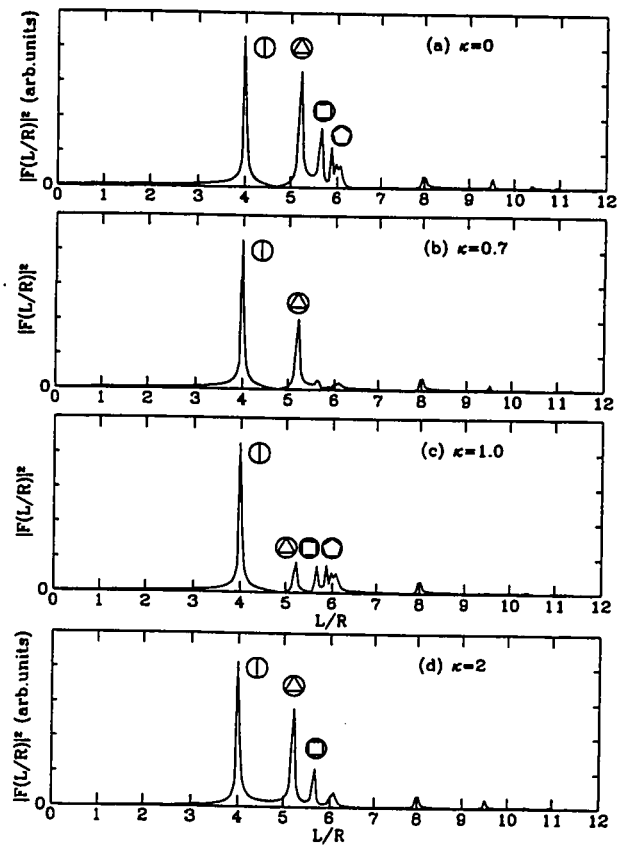


Figure 4.12: Fourier transforms of the quantum $\delta g_\gamma(E)$ in Fig.4.10 for $\kappa = 0$, 0.7, 1 and 2, as a function of the orbital length measured by the disc radius. The orbits are indicated for major peaks and we can see the changes in the contribution from each orbit to the density of states as $\kappa$ increases.

## 4.4 Summary

Quantum shell effects in finite fermion systems and their semiclassical interpretation in terms of periodic orbits has been a fascinating subject for more than two decades [Balian 72, Berry 76, Gutzwiller 90]. Recent technological advancement in fabricating mesoscopic systems has made it possible to realize "free" finite fermion systems much larger than atoms and nuclei, both in scale and number of fermions. These systems, such as simple metal clusters and quantum dots, have brought intriguing new aspects to the study of shell effects and their link to classical orbits. Quantum dots, especially, can be made so large that a quantum to classical transition may be observable.

We have examined the magnetization of a quantum dot for two limiting cases of mean-field potential, an isotropic harmonic oscillator for small number of electrons and a circular hard-wall or disc potential for a large number of electrons. Our aim was to compare the shell structure reflected in the magnetization between the two limits, as an indicator of the mean field, as well as to understand the quantum structure in terms of classical periodic orbits.

We have calculated the magnetization as a function of a parameter that is the ratio of the magnetic length and the length scale set by the mean field, so that we do not have to assume an effective size of the dot or field strength. When plotted as a function of this parameter, the magnetization has rapid beating oscillations in the weak-field (or strong-confinement) region, and the de Haas-van Alphen-type oscillations, with

the Aharonov-Bohm oscillations superimposed on them, in the strong-field (or weak-confinement) region. These features are common for both the harmonic and disc potentials. For harmonic confinement, there are no Landau levels in the strong-field limit and instead, the "Landau sheets" of continuous levels are formed, whereas the Landau levels emerge in disc confinement. This difference is reflected in the magnetization for the two cases as some quantitative difference in the shape of the dHvA oscillations.

In the case of harmonic confinement, the rapid beats or "supershells" in the weak-field region are understood as an interference effect between the two primitive periodic orbits. As the field becomes stronger, only one primitive, shorter orbit dominates, which approaches to the cyclotron orbit and gives rise to the dHvA-type oscillations. On the other hand, the other primitive, longer orbit that goes along the edge of the system results in the finer AB oscillations. Through the classical action of the edge orbit, we have found that each AB oscillation corresponds to two flux quanta added to the system. Also in disc confinement, the cyclotron and edge orbits explain the dHvA and AB structures, respectively. The supershells at weaker fields may be explained as an interference between shortest orbits in the disc, with curvature determined by the cyclotron radius which is shorter than the disc radius.

For the disc potential, we have also studied changes in the shell structure in the weak-field limit and their semiclassical interpretation through periodic orbits within first-order perturbation theory. We made comparison with the system in a spherical

cavity, the three-dimensional version of the disc potential, which may be regarded as modeling a large metal cluster. Both original systems have supershell structure, which is related semiclassically to shortest periodic orbits of high degeneracy. As in the spherical cavity, as $\kappa$ increases, the original supershells are gone and different beats emerge, with the repeated appearance and disappearance of different beating patterns. These phenomena up to $\kappa \simeq 5$ are understood both semiclassically and quantum mechanically in first-order perturbation theory, again as in the spherical cavity. The interesting difference between the two- and three-dimensional cases appears in the modulation factor of the perturbed trace formula, which modifies the contribution from each original orbit family – the cosine and spherical Bessel functions, respectively, of magnetic flux enclosed by the original orbit. Thus whereas the shell-oscillation amplitudes in the spherical cavity decay rapidly as $\kappa$ increases, there is no such decay in the disc system. The difference is whether the symmetry of the original system is broken or not by the perturbation [Creagh 96, Tomsovic 95, Ullmo 95]. The nondecay of amplitudes under a magnetic field in the disc confinement is also a difference from the harmonic case [Brack 96], which has originally a higher (U(2)) symmetry ; accordingly families of periodic orbits are destroyed by the field.

The fact that the bulk nature of electronic properties of quantum dots is well described by the effective single-particle picture is yet to be established further. For example, one might ask under what conditions, do exchange and other correlations among electrons become significant? As we saw in the magnetization in Sec.4.2, the

Zeeman effect of electron spins in GaAs is negligibly small for most field strengths. On the other hand, spin singlet-triplet oscillations due to the exchange effect have been predicted in the ground states of a quantum dot with two electrons [Wagner 92], and observed in a small dot in high magnetic fields [Ashoori 93]. Similar oscillations related not only to spins but also to total angular momentum in a quantum dot with a few electrons, have been predicted in the magnetization [Maksym 92]. The single-particle picture is yet powerful and may even be the only theoretical method to describe quantum dots with a large number of electrons. Measurements of the magnetization will open yet another window for understanding the single-particle nature and the shell structure of quantum dots.

# Chapter 5

# Conclusions

The objective of this thesis was to demonstrate that global shell structure of a finite many-fermion system can be understood semiclassically in terms of short periodic orbits. In this perspective, we have studied the effect of an external uniform magnetic field on the electronic shell structure of the mesoscopic systems of simple metal clusters and quantum dots.

In a leading semiclassical approximation, shell structure is governed by only closed periodic orbits. However, for a system in which the single-particle potential is a harmonic-oscillator well, the trace formula is exactly given, which links the quantum fluctuations, $\delta g$ of the density of states, with the classical periodic orbits. In Chapter 2, with a simple model of a two-dimensional cranked harmonic oscillator, we have illustrated a direct connection between the quantum shells and the periodic orbits. When cranked, an isotropic oscillator turns to be anisotropic with two different fre-

quencies, and the ratio of the two frequencies can be varied as the cranking rate is changed. A series of shell gaps appear in the quantum spectrum at rational frequency ratios, when classically families of periodic orbits are formed. We have also depicted the formation of the largest shell gaps with infinitely degenerate levels, when the cranking frequency equals the oscillator frequency : These levels are equivalent to the Landau levels of a charged particle in a uniform magnetic field.

In a finite system of electrons under a homogeneous magnetic field, the effect of the field on the electronic motion is determined by the ratio of the size of the system to the magnetic length. The latter corresponds classically to the cyclotron radius of an electron for a given energy. If the field is so weak that the magnetic length is larger than or barely comparable with the range of the orbital motion of electrons, perturbation by the field can be approximated by the linear Zeeman effect. In this approximation, the effect of the field is the same as that of cranking the system at the rate equal to the Larmor frequency. In Chapters 3 and 4, it has been seen in a metal cluster and a quantum dot that, similarly to the cranking, the electronic shell structure changes as the field strength is varied.

When a magnetic field is applied to a metal cluster, modelled by an electron gas confined in a spherical cavity, spherical symmetry is broken and the system turns to be nonintegrable. We thus anticipated drastic changes in the classical dynamics and hence in the electronic supershell structure. We have found, however, that there is little perceptible change in the supershells for realistic field strengths, for the cluster

sizes in which electronic shell effects are presently observable. It has also been found that if the field strength is increased yet further, the supershells are destroyed and different beating patterns emerge. These phenomena can be understood in first-order perturbation theory, which quantum mechanically leads to the Zeeman splittings of the energy levels and makes the problem identical to the "cranking" as described above. The changes in the shell structure or the formation of new shells as a function of the field can be understood semiclassically in connection with the original families of periodic orbits; rather than as due to the emergence of different periodic orbit families as is the case for the cranked oscillator.

For the semiclassical analysis in first-order perturbation, we have applied the "trace formula for broken symmetry" recently developed by Creagh [Creagh 96] to our problem. We have derived an explicit analytical formula for the cavity in a magnetic field, and have found that it reproduces the quantum results very well for the field strengths for which the first-order approximation works well also quantum mechanically. In the original system with spherical symmetry, there are many families of degenerate periodic orbits, and the shortest orbits of high degeneracy give rise to the pronounced supershells. Under perturbation by the field, most of the periodic orbit families are destroyed, yet it is these orbit families that have significant contribution to the trace when the perturbation is not too large. This explains the rather smooth and slight changes of the shell structure that appear when the field is switched on. Our model has thus proven to be another example verifying the usefulness of the new

trace formula, which yields smooth interpolation between trace formulae for different symmetries. In this first-order treatment, through Fourier transforms of $\delta g$, we have also elucidated the modifications of the shell structure in terms of rearrangements of the dominant contributions from the shortest orbits.

Unlike the case of the metal clusters, the electronic shell structure of a quantum dot can be drastically changed by a magnetic field of realistic strengths. We have studied the magnetization and the magnetic susceptibility of a quantum dot as a function of the field strength. Our aim was to compare the shell structure reflected in these magnetic properties in the two limits of the mean-field potential, an isotropic harmonic well and a circular disc. The main difference between the two cases is that in the strong-field limit, Landau levels emerge for disc confinement, whereas there are no Landau levels for harmonic confinement. In the strong-field limit, the Aharonov-Bohm oscillations appear, superimposed on the de Haas-van Alphen-type oscillations in the magnetization. In the spirit of periodic orbit theory, we have explained these Aharonov-Bohm oscillations in terms of the shortest orbits that go along the edge of the system.

A quantum dot is not a self-bound system, and a potential that confines electrons in a dot depends on the device. Not only the number of confined electrons, but also the size of a dot can be controlled externally. Thus, unlike the self-bound systems of nuclei and metal clusters, simply for a given number of electrons, one may not know the shape of the effective single-particle potential felt by the electrons in a dot.

The nature of the single-particle potential is reflected in the shell structure, which can be seen in the response functions of a quantum dot. This was our motivation to compare the magnetic properties for the mean-field potentials in the limit of a small and large number of confined electrons. On the other hand, the single-particle picture for the electronic properties of a quantum dot is yet to be experimentally established further. Measurements of the magnetization are awaited for further understanding of the single-particle nature and shell effects of quantum dots, along with their link to classical orbits.

# Appendix A

# Numerical Methods

## A.1 Diagonalization

### A.1.1 Spherical Cavity in a Uniform Magnetic Field

The Hamiltonian for an electron in a spherical cavity in a uniform magnetic field is given in Eq.(2) of the article included in Chapter 3. We evaluate the eigenvalues of this Hamiltonian by a numerical diagonalization. We first scale out the physical dimensions in the Hamiltonian, so that it can be written in terms of the dimensionless spherical coordinates $(r, \theta, \phi)$ as

$$\hat{H} = \hat{\mathbf{p}}^2 + \kappa m + \frac{1}{4}\kappa^2 r^2 \sin^2\theta + V(r) \,, \tag{A.1}$$

where lengths are measured in the cavity radius $R$ and energies in the natural energy unit for the cavity $E_0 = \hbar^2/2m_e R^2$. The dimensionless angular momentum, which we

have replaced with the azimuthal quantum number $m$, is preserved under the field. Apart from $m$, the Hamiltonian now depends on one dimensionless parameter, the ratio of the cavity radius and the magnetic length, $\kappa = (R/l_0)^2 = eBR^2/\hbar c$.

The Schrödinger equation $\hat{H}\Psi(\mathbf{r}) = E\Psi(\mathbf{r})$ reduces to

$$\left[\hat{\mathbf{p}}^2 + \frac{1}{4}\kappa^2 r^2 \sin^2\theta + V(r)\right] \Psi_m(\mathbf{r}) = E_m \Psi_m(\mathbf{r}) \,, \tag{A.2}$$

where $E_m = E - \kappa m$. The confining potential, $V(r) = 0$ $(r < 1)$ and $V(r) = \infty$ $(r \geq 1)$, sets the boundary condition, $\Psi_m = 0$ at $r = 1$. We choose to expand the wavefunction $\Psi_m$ in terms of the normalized, unperturbed ($\kappa = 0$) eigenfunctions $\{\psi_{nlm}\}$,

$$\begin{aligned} \Psi_m(\mathbf{r}) &= \sum_{n,l\geq|m|} C_{nl}\, \psi_{nlm}(\mathbf{r}) \\ &= \sum_{n} \sum_{l\geq|m|} C_{nl}\, A_{nl}\, j_l(k_{nl} r)\, Y_{lm}(\theta,\phi) \,, \end{aligned} \tag{A.3}$$

where $j_l$ is the spherical Bessel functions of order $l$ and $Y_{lm}$ the spherical harmonics. The $l$ $(= 0, 1, 2, ...)$ is the angular-momentum quantum number for the original system with no magnetic field, and for a given $m$, only values of $l \geq |m|$ are allowed. The $k_{nl}$ $(n = 1, 2, 3, ...)$ is the (dimensionless) wave-number eigenvalue, determined by the boundary condition $j_l(k_{nl}) = 0$ for the zero-field case, which also guarantees $\Psi_m$ to vanish at the boundary. The $A_{nl} \equiv \frac{\sqrt{2}}{|j_{l+1}(k_{nl})|}$ is a normalization factor so that the orthogonality relation can be written as

$$\int_0^1 dr\, r^2 \int d\Omega\, j_l(k_{nl} r)\, Y^*_{lm}(\theta,\phi)\, j_{l'}(k_{n'l'} r)\, Y_{l'm'}(\theta,\phi) = \frac{1}{2} j^2_{l+1}(k_{nl})\, \delta_{nn'}\, \delta_{ll'}\, \delta_{mm'} \,, \tag{A.4}$$

where $d\Omega$ is the solid-angle element. Equation (A.2) then becomes

$$\sum_{n,l\geq|m|} C_{nl}\,A_{nl}\left[k_{nl}^2+\frac{1}{4}\kappa^2 r^2\sin^2\theta\right] j_l(k_{nl}r)\,Y_{lm}(\theta,\phi)$$
$$= E_m \sum_{n,l\geq|m|} C_{nl}\,A_{nl}\,j_l(k_{nl}r)\,Y_{lm}(\theta,\phi)\,. \qquad \text{(A.5)}$$

Let us now multiply both sides of Eq.(A.5) with $A_{pq}\,j_q(k_{pq}r)\,Y^*_{qm}(\theta,\phi)$ and integrate over the space, $\int d\mathbf{r} = \int_0^1 dr\,r^2 \int d\Omega$. We thus obtain

$$\sum_{n,l\geq|m|} C_{nl}\left[k_{pq}^2\delta_{p,n}\delta_{q,l}+\frac{1}{4}\kappa^2 A_{pq}A_{nl}\int_0^1 dr\,r^2 j_q(k_{pq}r)r^2 j_l(k_{nl}r)\int d\Omega\,Y^*_{qm}\sin^2\theta\,Y_{lm}\right]$$
$$= E_m\,C_{pq}\,, \qquad \text{(A.6)}$$

where we have used the orthogonality relation A.4. The $\Omega$ integration of the second term of Eq.(A.6) can be done by using the recurrence relation for the spherical harmonics [Arfken 85]:

$$\cos\theta\,Y_{lm} = \sqrt{\frac{(l-m+1)(l+m+1)}{(2l+1)(2l+3)}}\,Y_{l+1,m} + \sqrt{\frac{(l-m)(l+m)}{(2l-1)(2l+1)}}\,Y_{l-1,m}. \qquad \text{(A.7)}$$

Using this relation twice, we obtain the $\Omega$ integration as

$$\int d\Omega\,Y^*_{qm}\sin^2\theta\,Y_{lm} = \delta_{ql}b_{lm} - \delta_{q,l+2}d_{lm} - \delta_{q,l-2}f_{lm}\,, \qquad \text{(A.8)}$$

where

$$\begin{aligned} b_{lm} &= 1-\frac{(l-m+1)(l+m+1)}{(2l+1)(2l+3)}-\frac{(l-m)(l+m)}{(2l-1)(2l+1)} \\ d_{lm} &= \sqrt{\frac{(l-m+1)(l+m+1)}{(2l+1)(2l+3)}}\sqrt{\frac{(l-m+2)(l+m+2)}{(2l+3)(2l+5)}} \\ f_{lm} &= \sqrt{\frac{(l-m)(l+m)}{(2l-1)(2l+1)}}\sqrt{\frac{(l-m-1)(l+m-1)}{(2l-1)(2l-3)}}. \end{aligned} \qquad \text{(A.9)}$$

Thus Eq.(A.6) can be reduced to

$$\sum_{n,l\geq|m|} C_{nl}\left[k_{pq}^2\delta_{p,n}\delta_{q,l}+\frac{1}{4}\kappa^2\left\{B_{p,n;qm}\delta_{q,l}-D_{p,n;qm}\delta_{q-2,l}-F_{p,n;qm}\delta_{q+2,l}\right\}\right]=E_m\,C_{pq}\,, \tag{A.10}$$

where we have defined

$$\begin{aligned} B_{p,n;qm} &= b_{qm}\,A_{pq}A_{nq}\int_0^1 dr\,r^4 j_q(k_{pq}r)\,j_q(k_{nq}r) \\ D_{p,n;qm} &= d_{q-2,m}\,A_{pq}A_{n,q-2}\int_0^1 dr\,r^4 j_q(k_{pq}r)\,j_{q-2}(k_{n,q-2}r) \\ F_{p,n;qm} &= f_{q+2,m}\,A_{pq}A_{n,q+2}\int_0^1 dr\,r^4 j_q(k_{pq}r)\,j_{q+2}(k_{n,q+2}r)\,. \end{aligned} \tag{A.11}$$

Equation (A.10) is nothing but the eigenvalue equation

$$\sum_{n,l\geq|m|} M_{pq,nl}\,C_{nl}=E_m\,C_{pq} \quad \text{or} \quad \mathbf{MC}=E_m\mathbf{C}\,, \tag{A.12}$$

where the matrix element $M_{pq,nl}$ is defined by the terms in the brackets in Eq.(A.10). The $\mathbf{M}$ is a real symmetric matrix, which can be diagonalized numerically. Note that the eigenvalue equation A.12 is invariant under the change $m \leftrightarrow -m$ and we solve it for each value of $|m|$. Thus for a given $|m|$, we obtain a set of eigenvalues $E_{|m|,i}$ with eigenvectors $\mathbf{C}_i$ ($i \equiv 1,2,3...$). Finally the total energy eigenvalues are given by

$$E_{m,i}=E_{|m|,i}+\kappa m \quad (m=0,\pm1,\pm2,\,...\,;\; i=1,2,3,...)\,, \tag{A.13}$$

and the wavefunction for each eigenenergy can be obtained from Eq.(A.3).

As discussed in Section 4.3.1, the eigenvalues for the two-dimensional version of this problem with a circular disc potential can be obtained similarly by diagonalizing

Hamiltonian (4.1). The formalism is basically the same as above. The unperturbed wavefunctions in this case are $\psi_{nm} = A_{nm}\, J_{|m|}(k_{n|m|}r)\, e^{im\phi}$, where $J_{|m|}$ is the (cylindrical) Bessel functions of order $|m|$, and $l_z = m\hbar$.

## A.2 The Shell-Correction Method

In this section, let us briefly describe the procedure for evaluating the shell correction, Eq.(1.5) of 1.1, which we have applied in Chapter 3 to the electron gas in a spherical cavity under a uniform magnetic field. This is the so-called shell-correction method that was introduced by Strutinsky [Strutinsky 67, Strutinsky 68, Brack 97] for calculating nuclear binding and deformation energies. It has been used extensively in nuclear physics and recently also for metal clusters. The method is based on a Hartree-Fock approximation, which yields single-particle energies $\{E_i\}$. The basic idea is to write the total energy for a given number of particles $N$ as

$$E_{tot} = \tilde{E}_{tot} + \delta E_{tot}\,, \tag{A.14}$$

where $E_{tot} = \sum_i E_i$. We have calculated the single-particle energies by assuming a spherical cavity as a mean-field potential confining electrons. Strutinsky developed a prescription for obtaining a smooth part of the density of states, $\tilde{g}(E)$ as in Eq.(1.3), from a given single-particle spectrum $\{E_i\}$. This has proven to be a useful tool for separating the density of states into smooth and oscillating parts. From $\tilde{g}(E)$ thus obtained, one can evaluate the smooth part of the total energy as

$$\tilde{E}_{tot} = \int_{-\infty}^{\tilde{E}_F} E\,\tilde{g}(E)\,dE\,, \qquad \text{where} \qquad N = \int_{-\infty}^{\tilde{E}_F} \tilde{g}(E)\,dE\,. \tag{A.15}$$

The shell-correction energy $\delta E_{tot}$ can then be calculated from Eq.(A.14). Note that, even if all the single-particle energies $\{E_i\}$ are positive as in our case, the lower bound

of the above integrals should extend to negative infinity. This is because of a spurious tail in the $\tilde{g}(E)$ coming from smoothing of the lowest few levels extended to lower energies.

In Chapters 3 and 4, in order to compare the quantum density of states with the semiclassical one in connection with short periodic orbits, we have smoothed the density of states $g(E) = \sum_i \delta(E - E_i)$ by convoluting it with a Gaussian :

$$g_\gamma(E) = \int_{-\infty}^{\infty} dE' \, g(E') \frac{1}{\gamma\sqrt{\pi}} e^{-(E-E')^2/\gamma^2} = \frac{1}{\gamma\sqrt{\pi}} \sum_i e^{-(E-E_i)^2/\gamma^2} . \qquad \text{(A.16)}$$

If we take the width $\gamma$ large enough ($\gtrsim$ the major shell spacing), all the shell oscillations reflected in $g_\gamma(E)$ can be damped out and $g_\gamma(E)$ becomes a smooth and monotonous function of $E$. If one takes this $g_\gamma(E)$ as the smooth part of the density of states, $\tilde{g}$ in Eq.(A.15), and evaluates $\tilde{E}_{tot}$, the shell correction $\delta E_{tot}$ thus obtained turns out to depend strongly on the value of $\gamma$. This is not satisfactory because $\gamma$ is an arbitrary parameter except that it should be of the order of the major shell spacing. Strutinsky argued that this is because the smooth function obtained from Eq.(A.16) does not have the curvature of the correct $\tilde{g}(E)$ at $E$, unless it is a constant or proportional to $E$ [Strutinsky 67, Ross 73]. To correct this deficiency, Strutinsky introduced the "curvature function" of order $2K$, $f_{2K}$ ($K = 0, 1, 2, ...$), and redefined $g_\gamma(E)$ as

$$g_\gamma(E) = \frac{1}{\gamma\sqrt{\pi}} \sum_i e^{-u_i^2} f_{2K}(u_i) , \qquad \text{(A.17)}$$

where $u_i = (E - E_i)/\gamma$. The $f_{2K}$ can be expressed in terms of Hermite polynomials

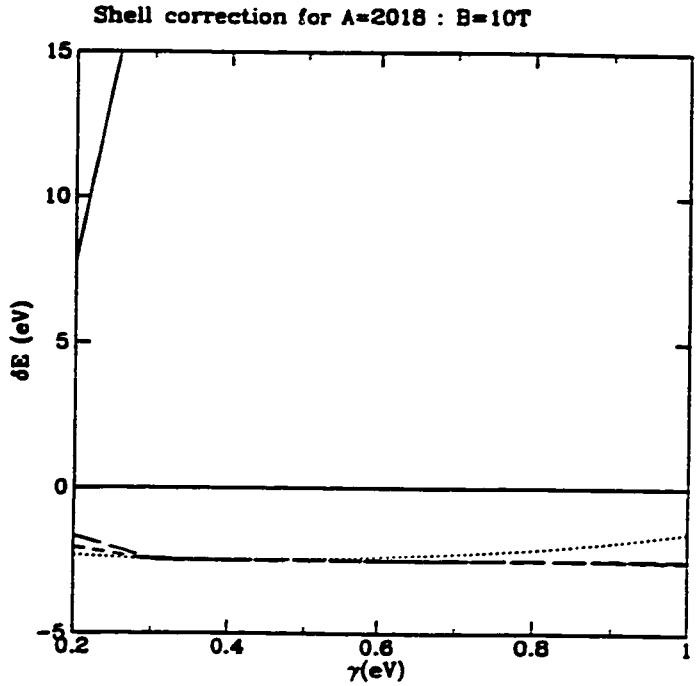


Figure A.1: Shell correction as a function of the smoothing width $\gamma$ for 2018 electrons in a metal cluster for the magnetic field strength $B = 10$ T. The solid line is for the curvature correction $2K = 0$, the dotted line is for $2K = 2$, the dashed line for $2K = 4$ and the long-dashed line $2K = 6$.

as

$$f_{2K}(u_i) = \sum_{l=0}^{2K} a_l H_l(u_i), \quad \text{with} \quad a_l = \frac{(-)^l/2}{2^l(l/2)!} \text{ (for even } l) \text{ or } 0 \text{ (for odd } l), \quad \text{(A.18)}$$

or equivalently $f_{2K}(u_i) = L_K^{1/2}(u_i^2)$, where $L_K^{1/2}$ is the associated Laguarre polynomial [Ross 72, Ross 73]. The $g_\gamma$ obtained from Eq.(A.17) contains the right curvature of the smooth density of states, provided that $K$ is taken large enough. The shell correction calculated using this $g_\gamma$ is found to be independent of $\gamma$ for a considerable range, and thus we can obtain an almost unique value of the shell correction. This is illustrated

in Fig.A.1 for the valence electrons in a metal cluster, modelled here by an electron gas in a cavity, under a magnetic field. In this figure, the shell correction $\delta E_{tot}$, for the number of particles $N = 2018$ and the field strength $B = 10$ T, is plotted as a function of $\gamma$ for several values of $K$. We have converted the dimensionless eigenvalues obtained as Eq.(A.13) by multiplying them with the energy scale for alkali metal clusters $E_0 = \hbar^2/2m_eR^2$, where $R = 2.25\,N^{1/3}\mathring{A}$. The Fermi energy for electrons in a metal cluster is about 3 eV. In Fig.A.1, the solid line is for $K = 0$, the dotted line is for $K = 1$, the dashed line $K = 2$ and the long-dashed $K = 3$. The $\gamma$ dependence is drastically reduced by the curvature correction of order $2K = 2$, and for $2K \geq 4$, the shell correction is virtually independent of $\gamma$ for $\gamma \gtrsim 0.3$ eV.

When there is no external field, the smooth part of the density of states for free particles in a spherical cavity is given analytically as [Balian 70]

$$\tilde{g}(E) = \frac{1}{E_0}\left(\frac{\sqrt{E}}{3\pi} - \frac{1}{4} + \frac{1}{3\pi\sqrt{E}}\right), \tag{A.19}$$

where $E$ is the dimensionless energy. We have compared this analytical $\tilde{g}(E)$ and $g_\gamma(E)$ numerically smoothed by means of Eq.(A.17), and have confirmed that the Strutinsky method yields the correct $\tilde{g}(E)$, except for a spurious tail described above. In the presense of a uniform magnetic field applied to the system, we did not know if this $\tilde{g}(E)$ would be affected by the magnetic field. Therefore, also for nonzero $B$, we have compared $g_\gamma(E)$, smoothed according to Eq.(A.17), with the analytical $\tilde{g}(E)$ for $B = 0$. We have found that the two are virtually identical as functions of $E$.

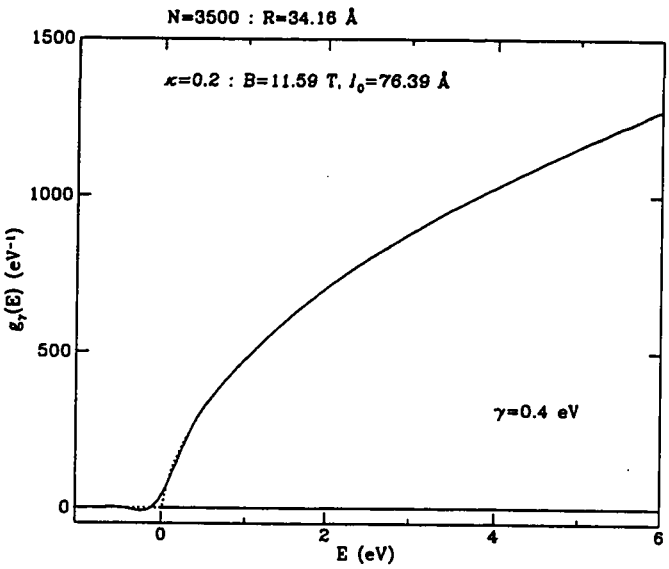


Figure A.2: Comparison of the numerically smoothed density of states for $\kappa = 0.2$, $g_\gamma(E)$ defined by Eq.(A.17) for $2K = 6$ and $\gamma = 0.4$ eV (solid line), and of the analytical $\tilde{g}(E)$ for $\kappa = 0$ given by Eq.(A.19) (dotted line).

In Fig.A.2, we compare $g_\gamma(E)$ for $\kappa = 0.2$ (solid line) with $\tilde{g}(E)$ given by Eq.(A.19) (dotted line). For $g_\gamma(E)$, we have taken $2K = 6$ and $\gamma = 0.4$ eV. In evaluating the energy scale $E_0$, the number of electrons is assumed to be $N = 3500$, which yields the semiempirical radius of $R \simeq 34\mathring{A}$. For this value of radius, $\kappa = 0.2$ corresponds to $B = 11.6$ T. In Fig.A.2 the two densities of states are indistinguishable except around $E = 0$, where a spurious tail of the $g_\gamma$ extends to the negative energy region. Thus we have concluded that the smooth density of states, analytically given by Eq.(A.19), is not affected by the field. We have also confirmed that the shell correction obtained by using the analytical $\tilde{g}(E)$ agrees with the one obtained by the Strutinsky procedure, for $B = 0$ as well as for $B \neq 0$. Thus this system has proven to be yet another example for which Strutinsky's method works very well.

# Bibliography


[Arfken 85] G. Arfken, *Mathematical Methods for Physicists*, 3rd edition (Academic Press, Orlando, 1985), p. 698.

[Ashoori 92] R. C. Ashoori et al., *Phys. Rev. Lett.* **68**, 3088 (1992).

[Ashoori 93] R. C. Ashoori et al., *Phys. Rev. Lett.* **71**, 613 (1993).

[Balian 70] R. Balian and C. Bloch, *Ann. Phys. (N.Y.)* **60**, 401 (1970).

[Balian 71] R. Balian and C. Bloch, *Ann. Phys. (N.Y.)* **63**, 592 (1971).

[Balian 72] R. Balian and C. Bloch, *Ann. Phys. (N.Y.)* **69**, 76 (1972).

[Berry 76] M. V. Berry and M. Tabor, *Proc. Lond.* **A 349**, 101 (1976).

[Berry 77] M. V. Berry and M. Tabor, *Proc. Lond.* **A 356**, 375 (1977).

[Beth 37] E. Beth and G. E. Uhlenbeck, *Physica* **4**, 915 (1937).

[Bhaduri 71] R. K. Bhaduri and C. K. Ross, *Phys. Rev. Lett.* **27**, 606 (1971).

[Bhaduri] R. K. Bhaduri and B. K. Jennings (unpublished).

[Bhaduri 94] R. K. Bhaduri, S. Li, K. Tanaka and J. C. Waddington, *J. Phys. A : Math. Gen.* **27**, L553 (1994).

[Bjørnholm 90] S. Bjørnholm et al., *Phys. Rev. Lett.* **65**, 162 (1990).

[Bogachek 72] E. N. Bogachek and G. A. Gogadze, *Zh. Eksp. Theor. Fiz.* **63**, 1839 (1972) ; *Sov. Phys. JETP* **36**, 973 (1973).

[Bohr 69] A. Bohr and B. R. Mottelson, *Nuclear Structure* (W. A. Benjamin, New York, 1969), Vol. I.

[Bohr 75] A. Bohr and B. R. Mottelson, *Nuclear Structure* (W. A. Benjamin, Reading, 1975), Vol. II, p. 598.

[Brack 93] M. Brack, *Rev. Mod. Phys.* **65**, 677 (1993).

[Brack 94] M. Brack, *Many-Body Physics*, edited by C. Fiolhais, M. Fiolhais, C. Sousa, and J. N. Urbano (World Scientific, Singapore, 1994), p. 233.

[Brack 95] M. Brack and S. R. Jain, *Phys. Rev. A* **51**, 3462 (1995).

[Brack 96] M. Brack et al., *Large Clusters of Atoms and Molecules*, edited by T. P. Martin (Kluwer Academic Publishers, Dordrecht, 1996), p. 1.

[Brack 97] M. Brack and R. K. Bhaduri, *Semiclassical Physics* (Addison-Wesley, Reading, 1997).

[Bréchignac 92] C. Bréchignac et al., *Physics and Chemistry of Finite Systems : From Clusters to Crystals*, edited by P. Jena et al. (Kluwer Academic Publishers, Dordrecht, 1992), Vol. I, p. 369.

[Chakraborty 92] T. Chakraborty, *Comments Cond. Matt. Phys.* **16**, 35 (1992).

[Creagh 96] S. C. Creagh, *Ann. Phys. (N.Y.)* **248**, 60 (1996).

[Darwin 30] C. G. Darwin, *Proc. Cambridge Phil. Soc.* **27**, 86 (1930).

[de Heer 93] W. A. de Heer, *Rev. Mod. Phys.* **65**, 611 (1993).

[Du 93] R. R. Du, H. L. Stormer, D. C. Tsui, L. N. Pfeiffer and K. W. West, Phys. Rev. Lett. **70** 2944 (1993).

[Feldman 70] A. Feldman and A. H. Kahn, *Phys. Rev. B* **1**, 4584 (1970).

[Feynman 64] R. P. Feynman and A. R. Hibbs, *Quantum Mechanics and Path Integrals* (McGraw-Hill, New York, 1964).

[Fock 28] V. Fock, *Z. Phys.* **47**, 446 (1928).

[French 78] A. P. French and E. F. Taylor, *An Introduction to Quantum Physics* (W. W. Norton & Company, New York, 1978), p. 456.

[Gasiorowicz 74] S. Gasiorowicz, *Quantum Physics* (John Wiley & Sons, New York, 1974), Ch. 19.

[Geerinckx 90] F. Geerinckx, F. M. Peeters, and J. T. Devreese, *J. Appl. Phys.* **68** 3435 (1990).

[Geilikman 69] B. T. Geilikman, *Yad. Fiz.* **9**, 894 (1969) ; *Sov. J. Nuc. Phys.* **9**, 521 (1969).

[Gutzwiller 67] M. C. Gutzwiller, *J. Math. Phys.* **8**, 1979 (1967).

[Gutzwiller 71] M. C. Gutzwiller, *J. Math. Phys.* **12**, 343 (1971).

[Gutzwiller 90] M. C. Gutzwiller, *Chaos in Classical and Quantum Mechanics* (Springer Verlag, New York, 1990), Chapter 17.

[Haldane 83] F. D. M. Haldane, *Phys. Rev. Lett.* **51**, 605 (1983).

[Hansen 89] W. Hansen et al., *Phys. Rev. Lett.* **62**, 2168 (1989).

[Haxel 49] O. Haxel, J. H. D. Jensen and H. E. Suess, *Phys. Rev.* **75**, 1766 (1949).

[Huang 65] K. Huang, *Statistical Mechanics* (John Wiley & Sons, New York, 1963).

[Jennings 76] B. K. Jennings and R. K. Bhaduri, *Phys. Rev. B* **14**, 1202 (1976).

[Kastner 92] M. A. Kastner, *Rev. Mod. Phys.* **64**, 849 (1992).

[Kastner 93] M. A. Kastner, *Phys. Today* **46**, 24 (1993).

[Kirkwood 33] J. G. Kirkwood, *Phys. Rev.* **44**, 31 (1933).

[Knight 84] W. D. Knight et al., *Phys. Rev. Lett.*, **52**, 2141 (1984).

[Knight 85] W. D. Knight, K. Clemenger, W. A. de Heer, and W. A. Saunders. *Phys. Rev. B*, **31**, 2539 (1985).

[Kumar 90] A. Kumar, S. E. Laux, and F. Stern, *Phys. Rev. B* **42**, 5166 (1990).

[Lagarias 92] J. C. Lagarias, *Proc. Symp. Appl. Math.* **46**, 35 (1992), edited by S. A. Burr.

[Landau 58] L. D. Landau and F. M. Lifshitz, *Quantum Mechanics* (Pergamon Press, London, 1958), p. 474.

[Laughlin 83] R. B. Laughlin, *Phys. Rev. Lett.* **50**, 1395 (1983).

[Lerme 96] J. Lerme et al., *Large Clusters of Atoms and Molecules*, edited by T. P. Martin (Kluwer Academic Publishers, Dordrecht, 1996), p. 71.

[Lindelof 96] P. E. Lindelof et al., *Large Clusters of Atoms and Molecules*, edited by T. P. Martin (Kluwer, Dordrecht, 1996), p. 89.

[Louck 73] J. D. Louck, M. Moshinsky and K. B. Wolf, *J. Math. Phys.*, **14**, 692 (1973).

[Maksym 90] P. A. Maksym and T. Chakraborty, *Phys. Rev. Lett.* **65**, 108 (1990).

[Maksym 92] P. A. Maksym and T. Chakraborty, *Phys. Rev. B* **45**, 1947 (1992).

[Malkin 69] I. A. Malkin and V. I. Man'ko, *Sov. Phys. - JETP*, **28**, 527 (1969).

[Martin 90a] T. P. Martin, T. Bergmann, H. Göhlich and T. Lange. *Chem. Phys. Lett.*, **172**, 209 (1990).

[Martin 90b] T. P. Martin, T. Bergmann, H. Göhlich and T. Lange. *Phys. Rev. Lett.*, **65**, 748 (1990).

[Mayer 48] M. G. Mayer, *Phys. Rev.* **74**, 235 (1948).

[Mayer 49] M. G. Mayer, *Phys. Rev.* **75**, 1969 (1949).

[McEuen 93] P. L. McEuen et al., *Physica B* **189**, 70 (1993).

[McIlroy 92] M. D. McIlroy, *Proc. Symp. Appl. Math.* **46**, 105 (1992), edited by S. A. Burr.

[Meir 90] Y. Meir, O. Entin-Wohlman, Y. Gefen, *Phys. Rev. B* **42**, 8351 (1990).

[Messiah 61] A. Messiah, *Quantum Mechanics* (North-Holland Publishing Company, Amsterdam, 1961), Vol. I, p. 454.

[Murthy] M. V. N. Murthy, Shankar, and S. Sinha (unpublished).

[Myers 66] W. D. Myers and W. J. Swiatecki, *Nucl. Phys.* **81**, p. 1 (1966).

[Nakamura 93] K. Nakamura, *Quantum Chaos* (Cambridge, 1993), Ch. 2.

[Niven 1991] I. Niven, H. S. Zuckerman and H. L. Montgomery, *The Theory of Numbers*, 5th edition (John Wiley & Sons, New York, 1991), p. 297.

[Pedersen 91] J. Pedersen et al. *Nature*, **353**, 733 (1991).

[Persson 95a] M. Persson et al., *Phys. Rev. B* **52**, 8921 (1995).

[Persson 95b] M. Persson et al., *J. Phys. : Cond. Matt.* **7**, 3733 (1995).

[Preston 75] M. A. Preston and R. K. Bhaduri, *Structure of the Nucleus* (Addison-Wesley, Reading, 1975).

[Reimann 96a] S. M. Reimann, M. Brack, A. G. Magner, J. Blaschke, and M. V. N. Murthy, *Phys. Rev. A* **53**, 39 (1996).

[Reimann 96b] S. M. Reimann, M. Persson, P. E. Lindelof and M. Brack, *Z. Phys. B* **101** 377 (1996).

[Richter 96] K. Richter, D. Ullmo, and R. A. Jalabert, *Phys. Rep.* **276**, 1 (1996).

[Rinaldi 96] R. Rinaldi et al., *Phys. Rev. Lett.* **77**, 342 (1996).

[Ross 72] C. K. Ross and R. K. Bhaduri, *Nucl. Phys.* **A 188**, 566 (1972).

[Ross 73] C. K. Ross, Ph. D. Thesis, McMaster University (1973).

[Shapiro 93] B. Shapiro, *Physica A* **200**, 498 (1993).

[Sheline 72] R. K. Sheline, I. Ragnarsson and S. G. Nilsson. *Phys. Lett.* **41B**, 115 (1972).

[Sivan 88] U. Sivan and Y. Imry, *Phys. Rev. Lett.* **61**, 1001 (1988).

[Strutinsky 67] V. M. Strutinsky, *Nucl. Phys.* **A 95**, 420 (1967).

[Strutinsky 68] V. M. Strutinsky, *Nucl. Phys.* **A 122**, 1 (1968).

[Tabor 89] M. Tabor, *Chaos and Integrability in Nonlinear Dynamics* (John Wiley & Sons, New York, 1989), p.70.

[Tomsovic 95] S. Tomsovic, M. Gringerg, and D. Ullmo, *Phys. Rev. Lett.* **75**, 4346 (1995).

[Tsui 82] D. C. Tsui, H. L. Stormer and A. C. Gossard, *Phys. Rev. Lett.* **48**, 1559 (1982).

[Ullmo 95] D. Ullmo, K. Richter, and R. A. Jalabert, *Phys. Rev. Lett.* **74**, 383 (1995).

[Van Vleck 28] J. H. Van Vleck, *Proc. Natl. Acad. Sci. USA* **14**, 178 (1928).

[Wagner 92] M. Wagner, U. Merkt and A. V. Chaplik, *Phys. Rev. B* **45**, 1951 (1992).

[Weis 93] J. Weis, R. J. Haug, K. von Klitzing and K. Ploog, *Physica B* **189**, 111 (1993).

[Wigner 32] E. Wigner, *Phys. Rev.* **40**, 749 (1932).

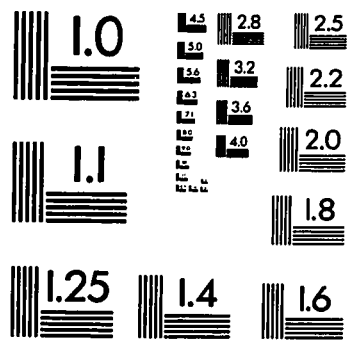


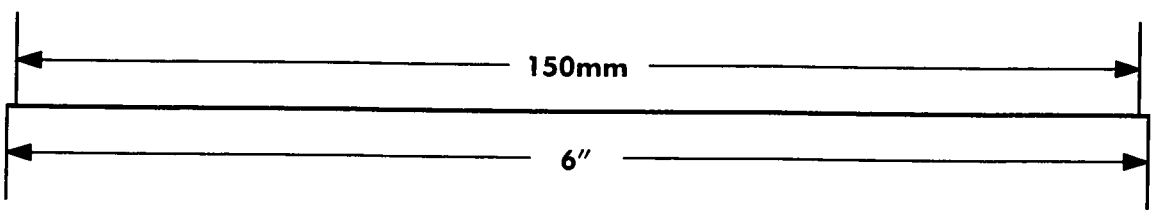


APPLIED IMAGE, Inc
1653 East Main Street
Rochester, NY 14609 USA
Phone: 716/482-0300
Fax: 716/288-5989